Quantum Jumps Between Fock States of an Ultracold Electron Cyclotron Oscillator

A thesis presented

by

Steven Eric Peil

to
The Department of Physics
in partial fulfillment of the requirements
for the degree of
Doctor of Philosophy
in the subject of
Physics

Harvard University
Cambridge, Massachusetts

May 1999

Abstract

Fock states of a one-electron cyclotron oscillator have been produced and observed nondestructively. The states are long-lived because spontaneous emission is inhibited by a factor of 140 using the modified radiation field of a cylindrical Penning trap. Direct, nondestructive observation is achieved with a magnetic gradient that is ten times larger than previously possible, allowing the states to be resolved with high signal-to-noise ratio. Quantum jumps up to the $n = 4$ cyclotron level have been observed. The potential line broadening from the increased magnetic coupling is avoided because we have lowered the temperature to which electrons can be cooled by nearly two orders of magnitude, to as low as 50 mK. This is the first time a trapped elementary particle has been cooled below 4.2 K. At these low temperatures, the cyclotron oscillator is completely cooled to its ground state. Detection of the electron signal is made possible by a low-power transistor that was developed in collaboration with condensed-matter colleagues. Applications include new single-electron spectroscopy techniques for an improved measurement of the electron g factor.

To my parents, Norman and Elda Peil.
Thanks for your steadfast support.

Contents

Table of Contents ii

Acknowledgments vi

List of Tables vii

List of Figures viii

1 Introduction 1

1.1 Fock States 2

1.2 Ultralow Temperatures 3

1.3 QED and the Fine Structure Constant 5

1.4 Other Motivations 8

1.4.1 Antihydrogen Production 8

1.4.2 Phase Transitions in a Cold Electron Plasma 8

2 Cooling Electrons Below 4 Kelvin 9

2.1 Closed-Endcap Cylindrical Trap 11

2.2 Radio-Frequency and Microwave Systems 15

2.2.1 Axial Detection and Excitation 15

2.2.2 Cyclotron Detection and Excitation 20

2.3 Trapping Potential 23

2.4 Millikelvin Temperature Production 26

2.4.1 General Description 26

2.4.2 Apparatus Details 28

2.5 Particle Confinement and Trap Vacuum 31

2.5.1 4 Kelvin 31

2.5.2 Below 4 Kelvin (No Trap Can) 31
2.5.3 Trap Can Design 35
2.6 Thermal Equilibrium 38

3 Low-Power Detection 41
3.1 Overview of RF Detection 42
3.2 Inductive Coupling 46
3.2.1 Reduced Trap Temperature 47
3.2.2 Instabilities 49
3.3 Commercial GaAs MESFET 51
3.3.1 Characterization and Applications 51
3.3.2 Optimization Procedure 54
3.4 Cryogenic HFET 57
3.4.1 HFET Design 57
3.4.2 Characterization 60
3.4.3 Additional Considerations 64
3.5 FET Comparison 64
3.5.1 DC Properties 65
3.5.2 AC Properties 66
3.6 Conclusions and Future Improvements 69

4 Quantum Jumps Between Fock States 70
4.1 Magnetic-Bottle Coupling 74
4.1.1 Bottle Field 76
4.1.2 Axial-Frequency Shift — Theory 78
4.1.3 Axial-Frequency Shift — Experiment 80
4.1.4 Thermal Issues 81
4.1.5 Counting Electrons 83
4.1.6 Future Considerations 83
4.2 Inhibited Spontaneous Emission 84
4.2.1 History 84
4.2.2 Cavity Modes of a Cylindrical Penning Trap 85
4.3 Quantum-Jump Thermometer 88
4.3.1 Interaction with Thermal Radiation 88
4.3.2 Temperature Measurement 91

4.3.3 Analysis . . . 94
4.4 Photon Antibunching . . . 96
4.5 Topics in Quantum Measurement . . . 98
4.5.1 QND Measurement . . . 98
4.5.2 Measurement Time . . . 98
4.5.3 Quantum Zeno Effect . . . 100
4.5.4 Zeno Time . . . 100
4.6 Future Experiments . . . 104

5 Toward $g-2$ 106
5.1 Reduced Axial Temperature . . . 108
5.1.1 General Magnetic Lineshape . . . 109
5.1.2 Cyclotron Resonance . . . 112
5.1.3 Anomaly Resonance . . . 117
5.2 Reduced Cyclotron Temperature . . . 121
5.3 Eliminating Cavity Shifts . . . 122
5.4 Future . . . 124

6 Conclusions 126

A Electrostatics 128
A.1 Definitions and Conversions . . . 128
A.2 Symmetric Potentials . . . 129
A.3 Antisymmetric Potentials . . . 130
A.4 Calculated Coefficients . . . 132

B Parametric Response with Weak Radiative Damping 133

C Dilution-Refrigerator Details 139
C.1 Performance Issues . . . 139
C.1.1 Vacuum Leaks . . . 139
C.1.2 Touch . . . 142
C.1.3 Plug . . . 144
C.2 Comparison to 4 Kelvin Systems . . . 145
C.3 Operating Procedure . . . 145
C.3.1 Cooling to 4 Kelvin . . . 145

C.3.2 Cooling Below 4 Kelvin 148
C.3.3 Removal of Refrigerator from Dewar 149

D Magnetic-Bottle Measurement in a Cylindrical Trap 152
D.1 Axial Displacement of Particles 152
D.2 Cyclotron Excitations 155

Bibliography 156

Acknowledgments

I am grateful to my advisor, Gerald Gabrielse, for his continual support throughout a rewarding graduate school experience. I appreciate his urging me to make it to Hemenway each week for the important meetings held there.

K. Abdullah and D. Enzer helped to get this project started, and B. Odom was invaluable during the final stages. I enjoyed working with both B. Odom and B. D'Urso over the past year. W. Itano provided insight into the Zeno effect, and B. D'Urso helped with aspects of the Zeno-time calculation. C. H. Tseng was a valuable resource, especially with the microwave system. This work would not have been possible without R. Beck and those in the group of R. Westervelt who made the low-power FETs possible. I found this collaboration to be very rewarding, and I am indebted to Rex for his efforts. S. Shepard was helpful with wirebonding and kind to allow me cleanroom privileges.

S. Cotreau, P. Crevoiserat, and L. Defeo and his group provided their talent and knowledge of machining. D. Moura and S. McNeil made the move of our 500-pound dewar from one corner of the lab to the other a reality. J. Ragusa was instrumental in the generation of the written thesis under stressful time constraints. I have always enjoyed hearing from A. Davis, and am grateful for the flowers with which she brightens our lab. Basketball added some recreation to my graduate school experience; thanks to all who showed up to play each week for the past seven years.

I have profited greatly from working with L. Haarsma, P. Janzen, D. Phillips, D. Enzer, D. Hall, L. Lapidus, A. Khabbaz, C. Levy, P. Yesley, J. Estrada, P. Oxley, T. Roach, J. Tan and M. Schneider. It has been a pleasure to work with these colleagues. I had the opportunity to supervise many undergraduates, including T. Fairfield, M. Drndic, J. Chen, A. Ross, D. Abrams and S. Laufer. Many others in the Harvard physics department provided help and support, including the Doyle, Westervelt, Tinkham and Silvera groups with dilution refrigerator issues, and my committee members, J. Doyle and M. Tinkham, who offered sound advice and were always accessible. The NSF provided financial support for this work.

I would like to express my deep gratitude to my parents and family, who have always been incredibly supportive. Most of all, I would like to thank Jill Center, who has been my greatest inspiration. She has been with me through it all, and helped make it an enjoyable experience.

List of Tables

2.1 Trap parameters and electron frequencies for our system. 13

3.1 Equilibrium temperatures with each amplifier design. 50
3.2 Optimization of low-power transconductance of MGF-1100. 56
3.3 HFET operating parameters at different temperatures. 63

4.1 Calculated and measured values of the leading expansion coefficients for the magnetic-field perturbation. 78
4.2 Center frequencies and Q values of the TM_{135} and TE_{127} modes. . . . 87

5.1 Experimental parameters relevant to magnetic-lineshape calculations. 110

A.1 Electrostatic expansion coefficients. 132

C.1 IVC leak rates. 140

List of Figures

1.1 Various determinations of the fine structure constant. 7

2.1 Dilution-refrigerator cooled Penning trap system. 10
2.2 Three fundamental particle motions in a Penning trap and the corresponding resonances observed at $T_{trap} \sim 100$ mK. 12
2.3 Cross-sectional view of a closed-endcap cylindrical Penning trap. . . . 13
2.4 Base-temperature wiring diagram. 14
2.5 Axial detection circuit. 16
2.6 In-phase and quadrature response of a 200 Hz electron cloud to an axial drive. 17
2.7 Diagram of RF electronics. 18
2.8 Cancellation of drive feedthrough. 20
2.9 Schematic of microwave system. 22
2.10 Absorption coefficient of teflon versus frequency. 24
2.11 Model of a dilution refrigerator. 27
2.12 1 K attenuator. 29
2.13 Liquid-helium dewar. 32
2.14 Drawing of the trap vacuum spaces. 33
2.15 ^{4}He vapor pressure versus temperature. 35
2.16 Temperature curves for the first demonstration of cooling electrons below 4.2 K. 36
2.17 Conical grease seal diagram. 37

3.1 Overview of RF detection. 43
3.2 Schematic of FET bias circuit. 44
3.3 Undriven and driven response of trapped electrons. 45
3.4 Drawing of inductive amplifier. 48

3.5 Temperature of amplifier can when the FET is dissipating 3 mW. . . . 49
3.6 Drain characteristics for the Mitsubishi MGF-1100 MESFET at 4.2 K. 52
3.7 Driven resonances of a 30-electron cloud, taken with the MESFET throttled to three different powers. 53
3.8 Optimization procedure for an "ideal" FET. 55
3.9 Optimization of MGF-1100 transconductance at low powers. 56
3.10 Representation of HFET, displaying fabricated design and heterostructure properties. 58
3.11 Optical micrograph of HFET. 59
3.12 HFET drain characteristics at 4.2 K. 61
3.13 Transfer characteristic of HFET at 4.2 K. 61
3.14 HFET DC properties at room temperature. 62
3.15 Driven single-electron resonances observed with 4.5 μW power dissipation. 63
3.16 Drain characteristics at 4.2 K for the HFET and the MESFET. . . . 65
3.17 Comparison of the transconductances of the two FETs. 66
3.18 Comparison of a tuned-circuit noise resonance obtained with each transistor. 67
3.19 Comparison of signal-to-noise of driven resonance amplitude obtained with each FET. 68

4.1 Illustration and observation of quantum jumps between Fock states of a single electron. 71
4.2 Observation of quantum jumps to low-n Fock states due to absorption of thermal photons and photons from an external drive. 73
4.3 Signal observed when the cyclotron oscillator makes transitions from $|0\rangle \rightarrow |1\rangle \rightarrow |2\rangle \rightarrow |1\rangle \rightarrow |0\rangle$. 73
4.4 Illustration of quantum jumps of a single ion. 74
4.5 Mechanical drawing for one of the nickel electrodes used to produce the bottle field. 75
4.6 Trap-assembly drawing showing placement of nickel rings. 75
4.7 Map of magnetic "bottle" field. 77
4.8 Quantum-jump signal observed at 80 mK when the electron's quadrature response is locked to a frequency reference. 81

4.9 Quadrature response of electron and error signal for a single quantum-level transition. 82
4.10 Quantum-jump signal obtained from clouds of 2 and 3 electrons. . . . 83
4.11 10 GHz portion of cavity-mode spectrum of cylindrical Penning trap. 86
4.12 Calculated lifetime when the cyclotron oscillator is tuned between the TM_{135} and TE_{127} modes. 88
4.13 Observation of quantum jumps with in-phase electron response. . . . 89
4.14 A sample of thermal-photon induced transitions at five different trap temperatures. 91
4.15 Measured distribution of energy levels at 4.2 K, 3.2 K, 2.0 K and 1.6 K. 93
4.16 Measurement of temperature and average occupation/photon number for the electron cyclotron oscillator and radiation field. 93
4.17 Measured stimulated absorption and stimulated emission rates. 95
4.18 Correlation function exhibiting photon antibunching. 97
4.19 Relativistic anharmonicity in the cyclotron oscillator. 105

5.1 Energy levels for an electron in a magnetic field. 108
5.2 Ratio of linewidth parameter to axial damping width as a function of T_z for the cyclotron and anomaly resonances. 113
5.3 Calculated cyclotron line profile $\chi_c(\nu)$ for axial temperatures of 4.2 K and 50 mK. 114
5.4 Single-electron cyclotron resonance. 116
5.5 Calculated anomaly line profiles. 118
5.6 Calculated anomaly resonances. 119
5.7 Calculations of the modified damping rate and frequency shift experienced by an electron coupled to the TM_{123} and TE_{115} cavity modes. 123

A.1 Convention for voltages applied to Penning trap electrodes. 128
A.2 Potential antisymmetric in z applied to the endcap electrodes. 131
A.3 Potential antisymmetric in z applied to the compensation electrodes. 132

B.1 Standard driven axial response and parametric response for a cloud of more than 1,000 electrons. 134
B.2 Example of the parametric response of a 15-electron cloud with weak radiative damping. 135

B.3 Successive traces of the 15-electron cloud's response to a resonant parametric drive. 136
B.4 Coulomb coupling constant Γ versus temperature for $V_0 = 10$ V and $V_0 = 100$ V. 138

C.1 ^{4}He level in the IVC as the system saturates after running for four days with a leak to the liquid-helium reservoir. 141
C.2 Cooling of the amplifier can and heating of the trap (ring electrode) due to a leak in the IVC. 141
C.3 Refrigerator behavior in the presence of a leak in the dilution unit. . . 143
C.4 The effect of a touch between amplifier coils on refrigerator behavior. 144
C.5 Evolution of Penning-trap apparatus. 146
C.6 Typical cooling curve for experiment when refrigerator resides in empty dewar near 77 K. 147
C.7 Cooling of dilution refrigerator to base temperature. 150

D.1 Axial frequency shift versus voltage applied between endcaps to shift center of oscillation. 154

Chapter 1

Introduction

The field of quantum optics [1] explores the quantum mechanical nature of a single mode of the radiation field in part through the generation of Fock states, the nonclassical energy eigenstates of the cavity oscillator. Recently, the techniques developed in this and related fields proved vital to the growing effort to use fundamental aspects of quantum mechanics for novel methods of computing and communication [2, 3]. We have realized a system for production and nondestructive observation of Fock states of a harmonic oscillator using an extremely cold electron cyclotron oscillator in a microwave Penning-trap cavity rather than a photon oscillator [4]. In addition to the inherent interest of this system, it makes available new techniques for a precision measurement of the magnetic moment of a single electron or positron. The oscillator is prepared in its ground state by cooling it to temperatures as low as 70 mK, and quantum jumps to higher Fock states are observed.

1.1 Fock States

The quantum-mechanical nature of light was first revealed through statistical effects such as photon antibunching (the anticorrelation of photons at short time intervals) [5, 6, 7, 8, 9], and sub-Poissonian amplitude fluctuations [9]. Now, non-classical harmonic-oscillator states are being generated for emerging fields such as quantum measurement and quantum communication [2] which require engineering the quantum state of a system. Squeezed states of an oscillator have been produced in several experiments [10, 11, 12], and there is much interest in generating arbitrary harmonic oscillator number states or Fock states. Cooling a quantum oscillator to its ground state puts it in the $n = 0$ Fock state, but exciting a particular number of energy quanta to make a state of $n > 0$ has proved challenging.

The $n = 0$ and $n = 1$ Fock states of a mode of the radiation field in a high finesse microwave cavity have been generated [13, 14], and efforts are underway to create states of the mode with arbitrary photon number n [15]. A different system, the RF motion of a single ion in a Paul trap, has recently been used in generating higher-n Fock states [12]. Detection, however, relied on a procedure which destroyed the prepared state. Both of these systems rely on low temperatures to suppress thermal excitations of the oscillator. The trapped ion is laser cooled to 0.2 mK, corresponding to 95% of the population in the ground state. The high-Q cavity in reference [13] is cooled to 0.8 K, giving the same fractional ground-state occupation.

In this work, the oscillator under study is the one-electron cyclotron oscillator cooled to temperatures as low as 70 mK, in which case it is in its ground state more than 99.99% of the time. This is the first time an isolated elementary particle has been cooled below 4 K. The system of a single electron confined in a microwave Penning-trap cavity is unique in that it incorporates elements of both the cavity-

QED and Paul-trap experiments. With this oscillator, Fock states up to the $n = 4$ level have been observed. These states are long-lived — on average 13 sec for $n = 1$ — because we use a surrounding microwave cavity to inhibit spontaneous emission. Unlike the earlier work discussed, the observation of these non-classical states does not rely on population transfer to a two-state system via a Jaynes-Cummings interaction, but rather results from a direct quantum non-demolition measurement [16] of the oscillator's energy. This QND detection leaves the Fock state intact.

1.2 Ultralow Temperatures

During the second half of this century, physicists strove to produce ever higher energies in their quest to reveal the most fundamental building blocks of matter. Accelerators were used to discover new elementary particles and an assortment of composite hadrons, leading to the development of the Standard Model of particles and forces [17]. The push toward progressively higher energies ultimately broke the TeV barrier at the Fermilab Tevatron.

In the meantime, physicists in other fields ventured to the opposite extreme of the energy scale, creating environments with temperatures close to absolute zero [18]. Among the fruits of their labors have been the revelation of quantum-statistical phase transitions and high-precision measurements for tests of fundamental physics.

Ultralow temperatures[1] have been produced using a variety of methods. The dilution refrigerator [20, 21], which can generate temperatures near 2 mK using a mixture of ^{3}He and ^{4}He, allows cooling of macroscopic samples via direct thermal contact. Incorporating adiabatic nuclear demagnetization techniques enables the

[1]We will use "ultralow" temperatures to mean those below 300 mK [18, 19].

production of temperatures as low as 2 μK [18].

Driven primarily by condensed-matter physics, these low-temperature technologies provide refrigerated environments in which experiments can be performed. Atomic physicists took a different approach to low-temperature production. They developed "traps" to confine particles for extended interaction and devised methods of cooling just the confined sample rather than the entire environment. The combination of laser and evaporative cooling has produced atoms with temperatures below 1 nK [22, 23]. While very effective, optical-cooling techniques are only applicable to atoms with transitions accessible to available lasers. More general methods for cooling additional types of atoms and other particles require resorting to dilution refrigeration as part of the cooling process. Using thermalization with a cold buffer gas [24], scientists have cooled a variety of atomic species [25, 26] and even molecules [27] to ultralow temperatures. The superthermal scattering process in liquid helium is used to create ultracold neutrons at a temperature of several millikelvin [28].

With charged particles, only ions with transitions appropriate for laser cooling had reached ultralow temperatures prior to this work. While evaporative cooling can be used in charged-particle experiments, its applicability is limited since most measurements are done with a single particle which is strongly coupled to a thermal reservoir (a damping circuit).

This thesis describes the first experiment in which electrons have been cooled to 50 mK, almost two orders of magnitude lower than previous electron experiments at 4.2 K [29]. The trap electrodes and RF detection circuit are cooled with a dilution refrigerator, providing radiative and resistive reservoirs of general applicability. Some of the techniques developed for this low-temperature Penning trap, including a novel transistor [30], may be useful in future efforts to confine other charged subatomic particles (protons, positrons and antiprotons) and a broad range of ions at these temperatures.

1.3 QED and the Fine Structure Constant

One of the most precise tests of quantum electrodynamics (QED) as well as the most precise CPT test with a lepton system [31] have been carried out with an isolated electron in a Penning trap at 4 K. Single-electron experiments are subject to thermal systematics that are dramatically reduced in our low-temperature apparatus.

The techniques demonstrated in this work should make possible an improved measurement of the electron's g factor, or *gyromagnetic ratio.* This dimensionless fundamental constant relates the particle's magnetic moment $\boldsymbol{\mu}$ to its spin $\boldsymbol{S}$,

$$\boldsymbol{\mu} = \frac{g}{2}\left(\frac{e}{m}\right)\boldsymbol{S}. \tag{1.1}$$

The magnitude of $\boldsymbol{\mu}$ can be written in units of the Bohr magneton μ_B, the natural unit for atomic magnetic-dipole moments, as

$$\mu = \frac{g}{2}\left(\frac{e\hbar}{2m}\right) = \frac{g}{2}\mu_B. \tag{1.2}$$

An improved measurement of g is important as a test of quantum electrodynamics and for a better determination of the fine structure constant.

The simplest solution of the Dirac equation yields an electron g factor of 2, while quantum electrodynamics predicts a deviation from 2. QED theory expresses g as an expansion in the fine structure constant α,

$$a \equiv \frac{g-2}{2} = C_1\left(\frac{\alpha}{\pi}\right) + C_2\left(\frac{\alpha}{\pi}\right)^2 + C_3\left(\frac{\alpha}{\pi}\right)^3 + C_4\left(\frac{\alpha}{\pi}\right)^4 + \ldots, \tag{1.3}$$

where we have introduced the electron *anomaly*,[2] a, which is about 10^{-3}. The original $g-2$ measurements were intended to test the validity of Eq. (1.3) by supplying the left-hand side of this expression, while measurements of α from other physical systems (see Fig. 1.1) and calculations of the expansion coefficients C_i were needed to evaluate the right-hand side of the expression. The most recent measurement of g gives [31]

$$a_e^{meas} = 1\ 159\ 652\ 188.4(4.3) \times 10^{-12}. \tag{1.4}$$

If we use the value of α obtained from the quantum Hall effect, the right-hand side of the expression becomes

$$a_e^{calc,\ qHe} = 1\ 159\ 652\ 156.4(1.2)(22.9) \times 10^{-12}, \tag{1.5}$$

where the first uncertainty is from the evaluation of the expansion coefficients C_i and the second is due to the measurement of the fine structure constant [32], which limits the precision of this QED test. New methods of determining α, including spectroscopy of helium fine structure [33] and atom recoil experiments [34], are in progress and may soon provide more precise values than the quantum Hall effect.

When Eq. (1.3) is used with the QED calculations and the measured g factor to determine the fine structure constant, the value obtained is the most precise of any method, with an uncertainty of 3.8 ppb. This uncertainty on α can presently be decreased by a factor of four with an improved g-factor measurement; theoretical progress expected in the next year will push this potential gain in precision to a factor of twelve [35, 36].

We have made several significant steps in this work toward a better g-factor

[2]Experiments that measure the electron g factor are interchangeably referred to as g-factor, $g-2$ or anomaly measurements.

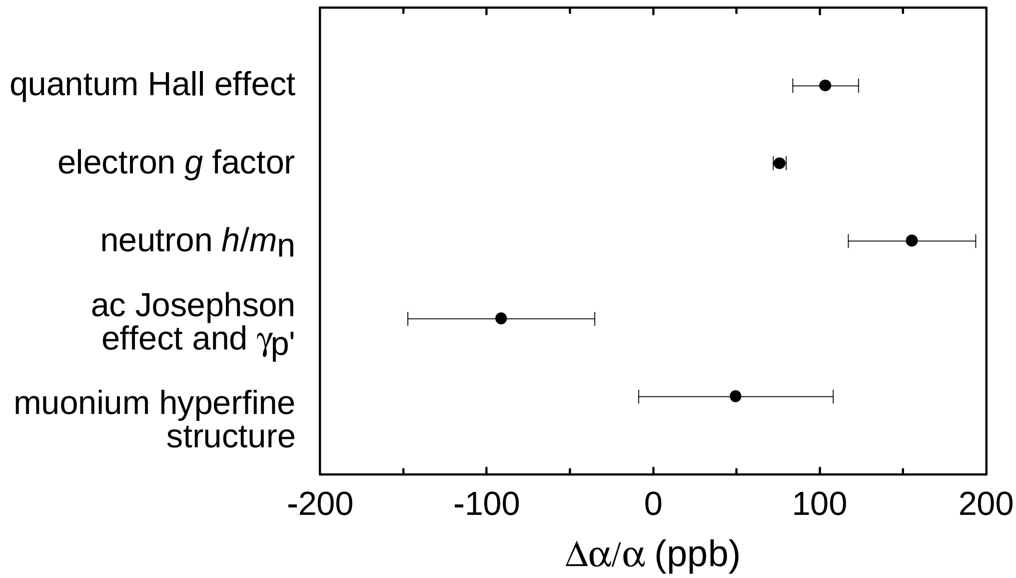

Figure 1.1: Various determinations of the fine structure constant, from references [32, 37]. The $x-$axis origin corresponds to the value of α from the 1986 adjustment of the physical constants [38].

measurement. Our reduced temperature enables us to use a larger magnetic-field gradient to achieve exceptional detection sensitivity of transitions in the magnetic systems, even while reducing the thermal systematics introduced by the magnetic "bottle". Our cylindrical trap geometry will allow us to reduce the uncertainty on the cavity shift in the cyclotron frequency, which was the leading uncertainty of the previous measurement done in a hyperbolic trap. Quantum-jump spectroscopy offers a new method of measuring the cyclotron frequency, using only the $n = 0$ to $n = 1$ transition and thus eliminating relativistic shifts that arise for $n > 1$.

1.4 Other Motivations

1.4.1 Antihydrogen Production

Efforts to produce cold antihydrogen in a nested Penning trap [39] will benefit from ultralow temperatures due to the temperature dependence of the formation rates. For collisional recombination, the process that dominates at high densities, the formation rate is expected to depend on temperature as [39]

$$R \propto T^{-9/2}. \tag{1.6}$$

The temperature dependence is less sensitive for radiative recombination [39],

$$R \propto T^{-0.63}, \tag{1.7}$$

which could become the dominant process if laser stimulation is incorporated. A dilution refrigerator-cooled antihydrogen apparatus is presently being designed.

1.4.2 Phase Transitions in a Cold Electron Plasma

An electron plasma subject to a parametric drive exhibits self-organized, collective phenomena that are sensitive to the energy in the internal motions of the plasma. The radiative cooling that results when coupled to the resonant electromagnetic modes of a Penning trap makes a parametrically pumped electron plasma an excellent probe of these cavity modes [40]. Plasma experiments at temperatures between 4 K and tens of mK should enrich these studies and additionally lead to phase transitions marked by the onset of short-range order in the plasma and possibly crystallization [41, 42, 43, 44]. Some additional thoughts are in Appendix B.

Chapter 2

Cooling Electrons Below 4 Kelvin

Electrons were first confined in a modern-day Penning trap using a room-temperature apparatus [45]. The necessity for a better vacuum and reduced noise lead to experiments at 77 K and subsequently 4.2 K. Electron experiments in a liquid-helium environment have produced remarkably precise measurements of the proton-electron mass ratio [46] and the electron g factor (and in turn the fine structure constant) [31], as well as one of the first demonstrations of inhibited spontaneous emission [47].

We have cooled isolated electrons below 4 K for the first time, demonstrating temperatures as low as 50 mK. This is almost 100 times lower than previous electron experiments. Our millikelvin ion-trap work requires new apparatus and techniques compared to liquid-helium systems. Figure 2.1 shows an overview of the cryogenic components of the experiment. The trap electrodes, vacuum can, and detection electronics are mounted to the mixing chamber of a dilution refrigerator which creates the low-temperature environment.

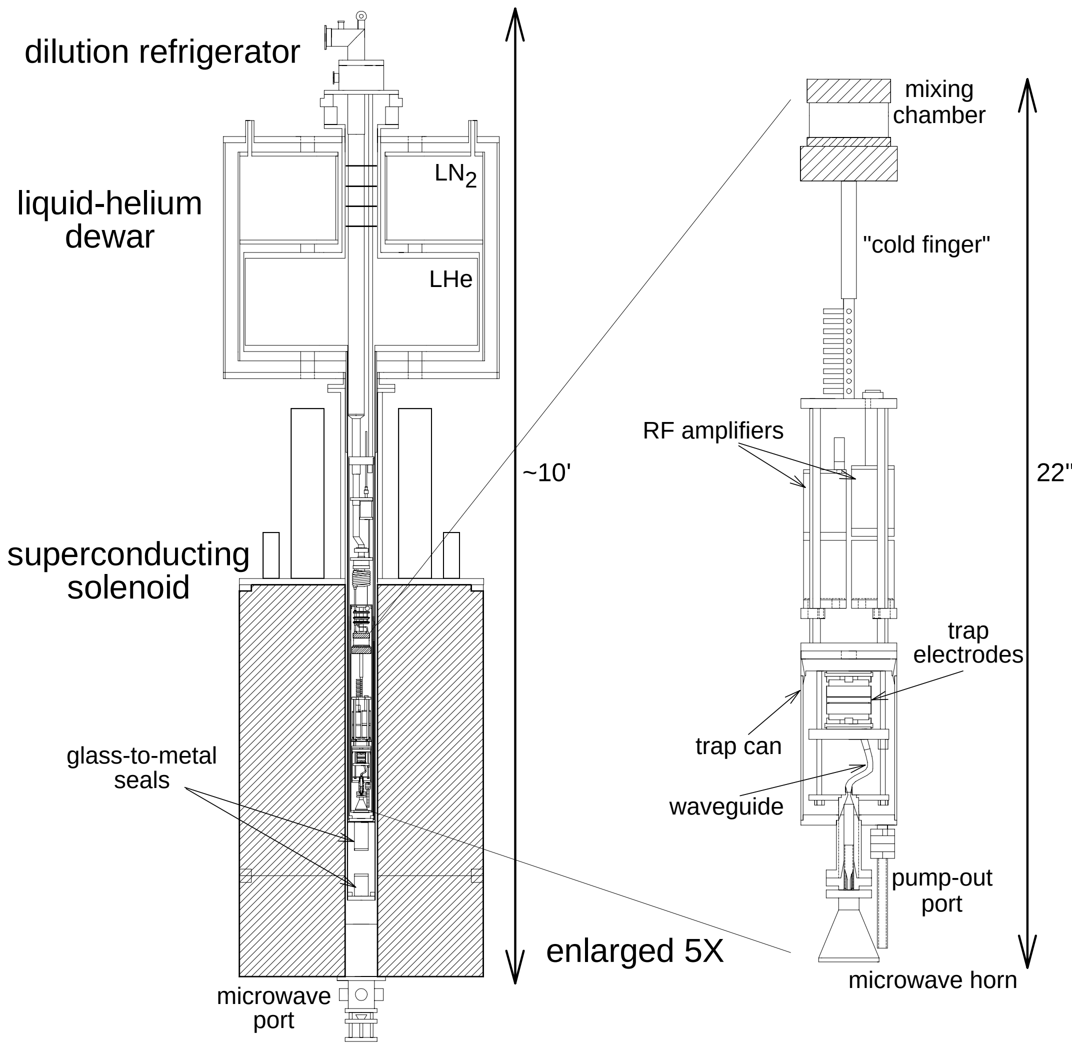

Figure 2.1: The cryogenic system consists of three major components. A dilution refrigerator resides in the tail of a liquid-helium dewar which extends into the bore of a superconducting solenoid. The enlargement shows the Penning trap and associated electronics anchored to the mixing chamber of the dilution refrigerator.

2.1 Closed-Endcap Cylindrical Trap

A Penning trap confines a charged particle radially with a strong, 5.2 T magnetic field and axially (in the direction of the magnetic field) with an electrostatic quadrupole potential. The particle oscillates in the axial potential well with frequency[1]

$$\nu_z = \frac{1}{2\pi}\sqrt{\frac{eV_0}{md^2}\left(1 + C_2\right)} \approx 64 \text{ MHz} \tag{2.1}$$

for an electron in our trap. The coefficient C_2 is discussed in Appendix A and d specifies the size of the trap cavity. The cyclotron motion is at

$$\nu_c = \frac{1}{2\pi}\left(\frac{eB}{m}\right) = 147 \text{ GHz} \tag{2.2}$$

for $B = 5.2$ T. A third oscillation, the magnetron motion, is a slow orbit about the trap center due to the combination of electric and magnetic fields, typically exhibiting a frequency near 14 kHz for an electron. Figure 2.2 illustrates these three motions and shows some of the first resonances observed at low temperatures. Trap parameters for our experiment are listed in Table 2.1.

The magnetic field introduces a Zeeman splitting to the energy levels of a spin-1/2 particle. The two spin eigenstates are separated in energy by $h\nu_s$, where

$$\nu_s = (g/2)\nu_c. \tag{2.3}$$

A g-factor measurement requires determining ν_s and ν_c, as discussed in Chapter 5.

A trapped particle is confined in a cavity formed by a series of OFHC copper electrodes, isolated from each other by MACOR ceramic spacers. Figure 2.3 shows

[1] We will use frequency ν or angular frequency $\omega = 2\pi\nu$, depending on which is more convenient.

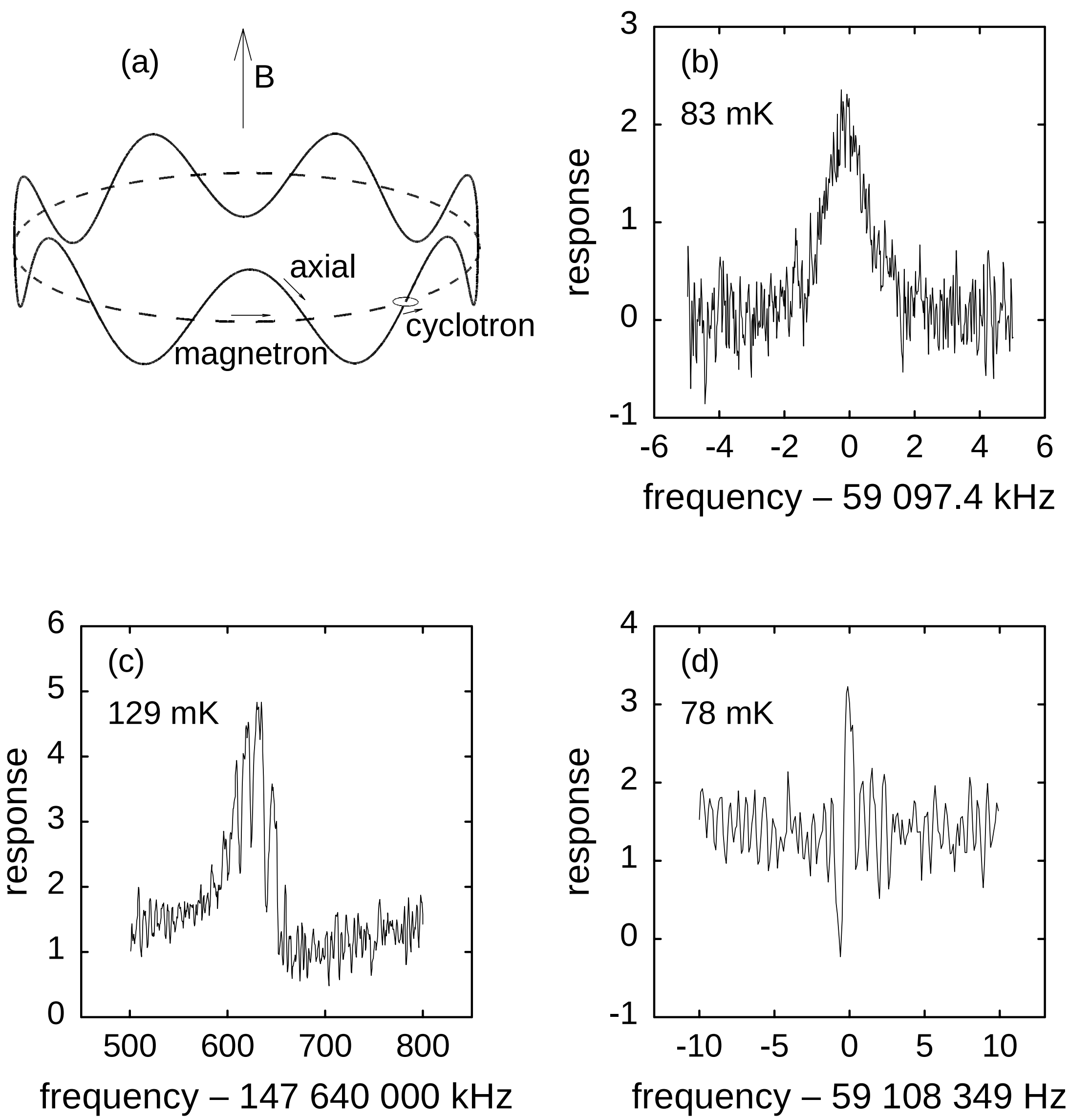

Figure 2.2: (a) The three fundamental particle motions in a Penning trap and the (b) axial, (c) cyclotron and (d) magnetron resonances for a cloud of several hundred electrons. These were the first observations of the three motions while keeping $T_{trap} \sim 100$ mK (the trap temperature is shown). (The distinct peaks in (c) are magnetron sidebands.)

parameter	value
V_0	10.18 V
ν_z	63.95 MHz
B	5.24 T
ν_c	146.664 2 GHz
ν_m	13 950 Hz
ρ_0	.1797 in (.4564 cm)
z_0	.1513 in (.3842 cm)
Δz	.0274 in (.0696 cm)
d	.35 cm
C_2	0.125 (calc)

Table 2.1: Some useful trap parameters and electron frequencies for our system. (These frequencies correspond to the single-electron work discussed in the following chapters, and are not the same as those in Fig. 2.2, which were from an initial demonstration.)

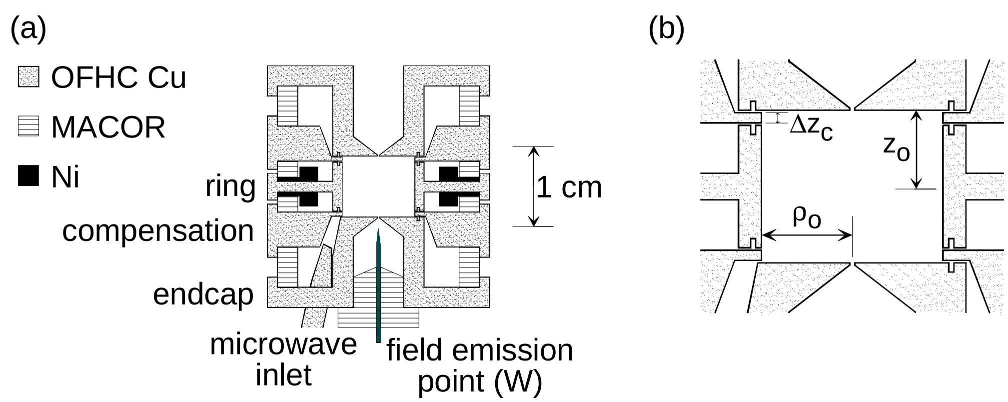

Figure 2.3: (a) Cross-sectional view of our closed-endcap cylindrical Penning trap. (b) Enlargement of the cavity ($\times 2.5$) for definition of constants z_0 and ρ_0. The dimension Δz_c, the height of the compensation electrode surface exposed to the cavity, is used in computing electrostatic expansion coefficients as discussed in Appendix A.

the trap assembly drawing. The top and bottom endcap electrodes are referenced to ground through 1 MΩ resistors, as illustrated in the wiring diagram in Fig. 2.4. Voltages applied to the ring and compensation electrodes produce a harmonic potential at the center of the trap. See Appendix A for a complete treatment of the electrostatics of this trap in terms of experimental variables and variables used in the literature [48, 49].

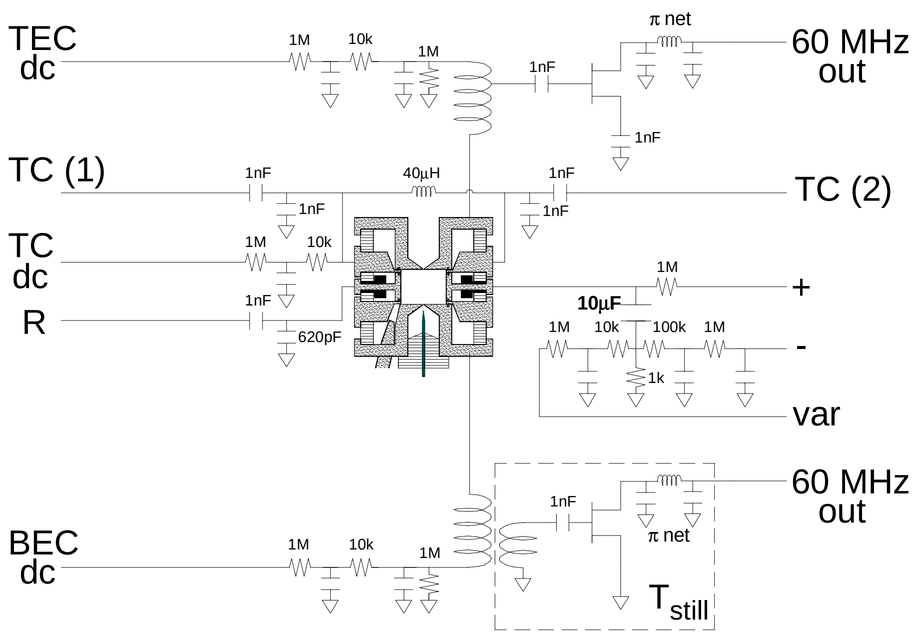

Figure 2.4: Base-temperature wiring diagram. The two RF amplifier designs are shown. Each compensation electrode is split into two halves — a separate drive line runs to each half and an inductor connects the two for low frequencies. (Only the wiring for the top compensation electrode is shown here; the bottom is wired separately but identically.) The "var" line is used to apply adjustments to the trapping potential in order to lock the axial frequency or account for a decaying ring voltage.

Electrons are loaded into the trap by applying a high voltage to a sharp tungsten needle dubbed the "field emission point", or FEP. The applied voltage can be between 200 and 2000 V, depending upon the sharpness of the point and the current desired. The high electric field created at the tip is strong enough to allow electrons to tunnel from the tungsten. This energetic beam of electrons dislodges and ionizes atoms condensed on the walls of the experiment near the trapping region. Secondary electrons produced in this process become trapped.

2.2 Radio-Frequency and Microwave Systems

2.2.1 Axial Detection and Excitation

The 60 MHz axial oscillation of a confined electron induces an RF current in the trap electrodes. The endcap and adjacent compensation electrode are incorporated into a detection circuit with the coil of a tuned amplifier. The coil inductance, trap capacitance and RF resistance form an LCR circuit, designed to resonate at $\nu_{LC} = \nu_z$ (Fig. 2.5). An electron sees a real impedance R with a value proportional to the Q of the tuned circuit [48],

$$R = Q\omega_z L. \tag{2.4}$$

The oscillating voltage across this resistance due to the current induced by the electron's motion is applied to the gate of a cryogenic FET, which provides the necessary power gain to drive the 50 Ω room-temperature amplifiers that follow. (The entire RF detection chain is shown in Fig. 2.7.) Thermal Johnson noise drives the tuned circuit, generating a "noise resonance" from which the values of the resistance R and its effective temperature can be obtained. Additional details of this RF detection are presented in Chapter 3.

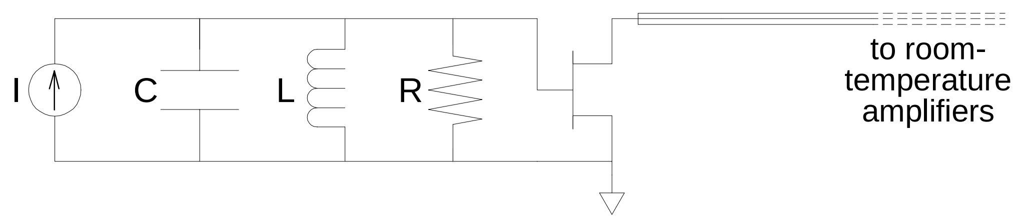

Figure 2.5: Detection circuit. C is the capacitance of the trap electrodes, L is the inductance of the amplifier coil, and R is the effective resistance seen by the electron (and the input impedance at ν_z).

We use a cryogenic amplifier on each endcap,[2] tuned to different frequencies. The coupling of the electron signal to the FET is different for the two detectors. One uses the conventional method of a direct tap to the inductor, creating an auto-transformer, while the other employs inductive coupling that provides a physical, thermal break (see Fig. 2.4). This break allows the transistor's heat to be directed away from the trap to the still, which requires several milliwatts for optimal refrigerator performance.

The amplifier's noise resonance can be used to obtain an "undriven" particle signal as discussed in Chapter 3. For cyclotron- and spin-frequency measurements, the axial motion is typically driven. An FM excitation scheme is used in order to minimize direct feedthrough to the tuned amplifier [48]. A 5 MHz drive applied to the ring electrode modulates the trap depth, creating sidebands on the particle's axial motion. The lower sideband is driven with a $\nu_z - 5$ MHz signal on the compensation[3] electrode and the particle's response at ν_z is detected. After pre-amplification

[2]Our use of two amplifiers is a practical way of developing some new techniques, including the inductive coupling and the cryogenic FET discussed in Chapter 3, while always having a traditional amplifier as a back-up and for comparison. A proposed detection scheme may make use of both amplifiers in the future.

[3]Typically this drive is applied to the "free" endcap when only one amplifier is used.

in the cryogenic environment and $\sim$ 70 dB of gain at room temperature, the signal is mixed to 5 MHz. Processing of this IF is facilitated by readily available commercial devices (filters, amplifiers, etc.) for this frequency. The "mixed-down" electron signal is measured using an EG&G 5202 lock-in amplifier, with the ring drive as the reference. The lock-in can be adjusted to output either the component of the particle's signal that is in phase with or in quadrature to the drive; both are shown in Fig. 2.6. Figure 2.7 illustrates the electronics involved in RF excitation and detection.

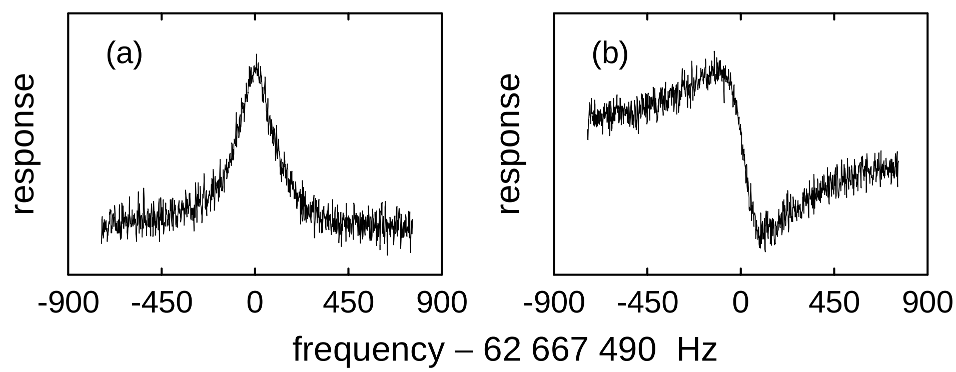

Figure 2.6: Response of a 200 Hz cloud (about 40 electrons) to an axial drive — (a) the in-phase component and (b) the quadrature component. These signals were obtained at 4.2 K.

The electron's quadrature response has a dispersive shape, with the linear region centered on ν_z. This linear portion of the resonance is used to lock the electron's axial frequency to an oscillator by serving as the error signal for a lock-loop; if ν_z changes, the resonance shifts and the error voltage measured is proportional to $\Delta\nu_z$. The correction voltage generated is applied to the "variable voltage" line ("var" in Figs. 2.4 and 2.7) which allows current to be sent through a resistor between the 'lo' of the ring's DC line and ground, slightly modifying the trapping potential. This

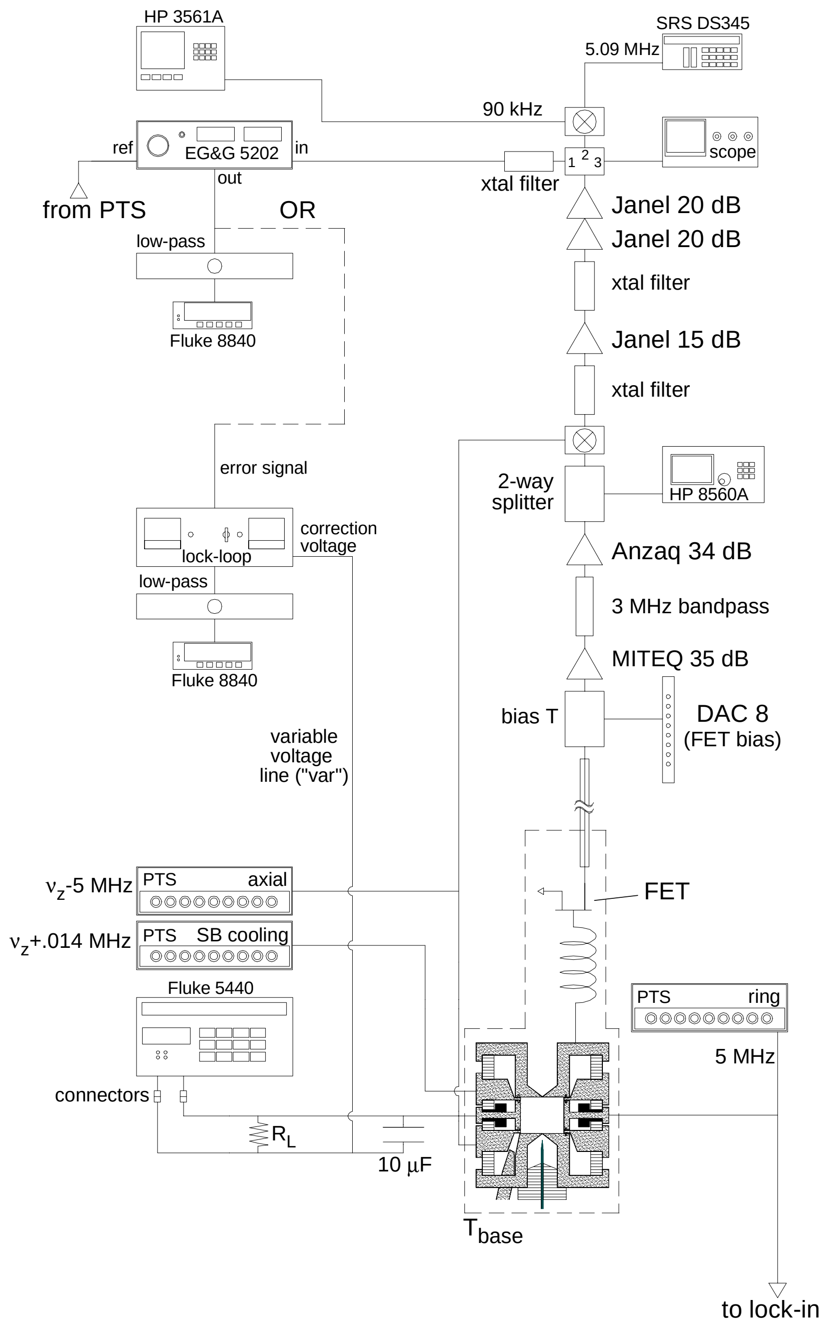

Figure 2.7: Electronics involved in RF excitation and detection. For "frequency-shift detection", the lock-in's $\phi = \pi/2$ output is used to lock the electron's axial frequency to the crystal oscillator in a PTS synthesizer. A correction voltage can be applied to the trap using the variable voltage line ("var"). The Fluke 5440 is used to charge the 10 μF capacitor to the desired trapping voltage, and is then disconnected.

voltage is also proportional to the change in energy of the cyclotron oscillator or spin system when they are coupled to the axial frequency via a magnetic bottle (see Chapter 4), and thus serves as the excitation amplitude. Detailed descriptions of these techniques can be found elsewhere; for example, see references [48, 50] for more on coherent detection, and refer to [51] for "frequency-shift detection".

Even with the FM excitation scheme, there can be a high background added to the electron signal from drive feedthrough. Both drives, at 5 MHz and at $\nu_z - 5$ MHz, can capacitively couple to the gate of the FET. The transistor acts as a mixer, generating a signal at the sum frequency, ν_z. This is a more substantial problem with our directly coupled amplifier than with the inductively coupled amp, presumably because the transformer attenuates the 5 MHz drive significantly before it reaches the FET. A simple way of eliminating this feedthrough is to couple an additional 5 MHz signal to the transistor (using a spare drive line). With proper adjustment of the amplitude and phase[4] of the drive, the total 5 MHz at the FET can be cancelled without affecting significantly the 5 MHz being applied to the trap. Figure 2.8 shows the feedthrough spike we see on our signal analyzer, mixed from ν_z down to 90 kHz, before (a) and after (b) we apply the cancellation drive.

Another axial-excitation technique, parametric excitation, is useful for probing the trap's cavity-mode structure [40] and for realizing a one-bit memory with a single electron as a tool for "dark detection" and precision measurements [52]. This excitation results from driving the ring electrode at $2\nu_z$, thus modulating the axial spring constant at this frequency. Interesting behavior in the response of an electron cloud to a parametric drive when the cyclotron motion is decoupled from the trap's cavity modes is presented in Appendix B.

[4]We use an SRS DS345 frequency synthesizer with manual phase adjustment.

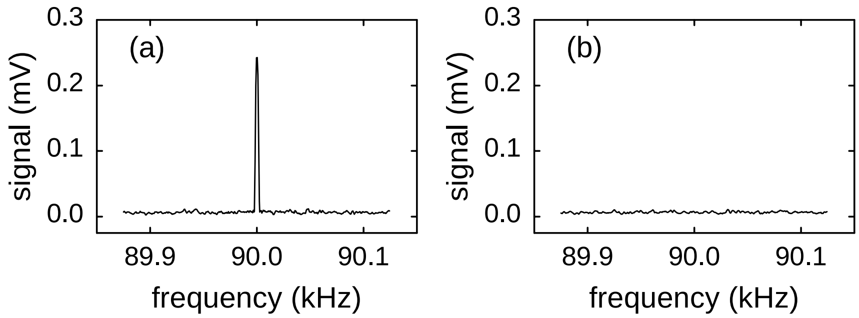

Figure 2.8: (a) Feedthrough spike, observed as 240 μV on a signal analyzer at the end of our RF detection chain. (b) Applying a 5 MHz drive to a resistor near the FET with the appropriate phase and amplitude can be used to kill the total 5 MHz level at the gate of the transistor. These pictures demonstrate a reduction of 30 dB.

2.2.2 Cyclotron Detection and Excitation

An electron's cyclotron frequency is high enough that the current induced in the trap electrodes by this motion is difficult to directly detect. Instead, a coupling is introduced to make the axial oscillation frequency dependent on the energy of the cyclotron motion. This "magnetic bottle" coupling is the subject of Section 4.1.

The cyclotron oscillator is driven with 147 GHz ($\lambda = 2$ mm) radiation. The microwave drive is generated with a system developed by C. H. Tseng, D. Enzer and F. Walls (summarized in Fig. 2.9 and described in detail in reference [53]). This system produces a 10.6 GHz signal which is frequency multiplied to generate D-band microwaves. Stabilization of the X-band drive is the heart of the microwave apparatus.

A 10.6 GHz oscillator drives a lead-coated iridium cavity with $Q \approx 20,000$. The output of the cavity is locked to the input using a fast phase-locked loop, stabilizing the microwaves for short times. For long-term stability, the cavity output is locked to a reference based on a 10 MHz crystal oscillator inside an HP8662A synthesizer.

From this oscillator, the frequency synthesizer generates a 640 MHz (rear) output that drives a step recovery diode (HP33004), producing a comb of harmonics. The 16th harmonic at 10.24 GHz is harnessed and mixed with the output of the 10.6 GHz source. The resultant 360 MHz is mixed with a 360 MHz signal from the adjustable (front) output of the same HP8662A. This DC voltage serves as the error signal for a slow lock-loop that provides long-term stability.

The stabilized 10.6 GHz drive is mixed with an IF signal, from a second HP synthesizer (8663A), at 680 MHz to produce 11.28 GHz microwaves. An X-band waveguide and microwave cable transmit this signal to the bottom port of the magnet where the D-band radiation is generated. The 11.28 GHz drives a harmonic mixer (Alpha 922FXOHN) containing a GaAs Schottky-barrier diode. The 13th harmonic is resonant with our 147 GHz cyclotron oscillator. The diode must be driven with a power between 15 and 18 dBm, a range which is above its saturation point but below its damage threshold. The D-band power level is controlled with a micrometer-driven mica-vane attenuator (Alpha TRG 523/716).

By adjusting the HP8663A IF or choosing a different harmonic of the 11 GHz signal, this system can be used to generate microwaves at all cyclotron frequencies relevant to our experiment, from the fundamental of the trap ($\approx$ 25 GHz) to the frequency at the highest solenoid field (165 GHz). (The only narrow-band component in the system is a filter in the 11 GHz section which has a bandwidth of several percent.) There are many amplifiers, filters, circulators, and isolators used in the microwave system that have not been mentioned here.

The microwaves are transmitted through the bottom port of the magnet, through the liquid helium in the dewar, into the IVC of the refrigerator and into the trap can, coarsely guided by teflon lenses. Access to the different cryogenic vacuum regions is achieved with glass-to-metal seals from Larson Electronic Glass [54]. These

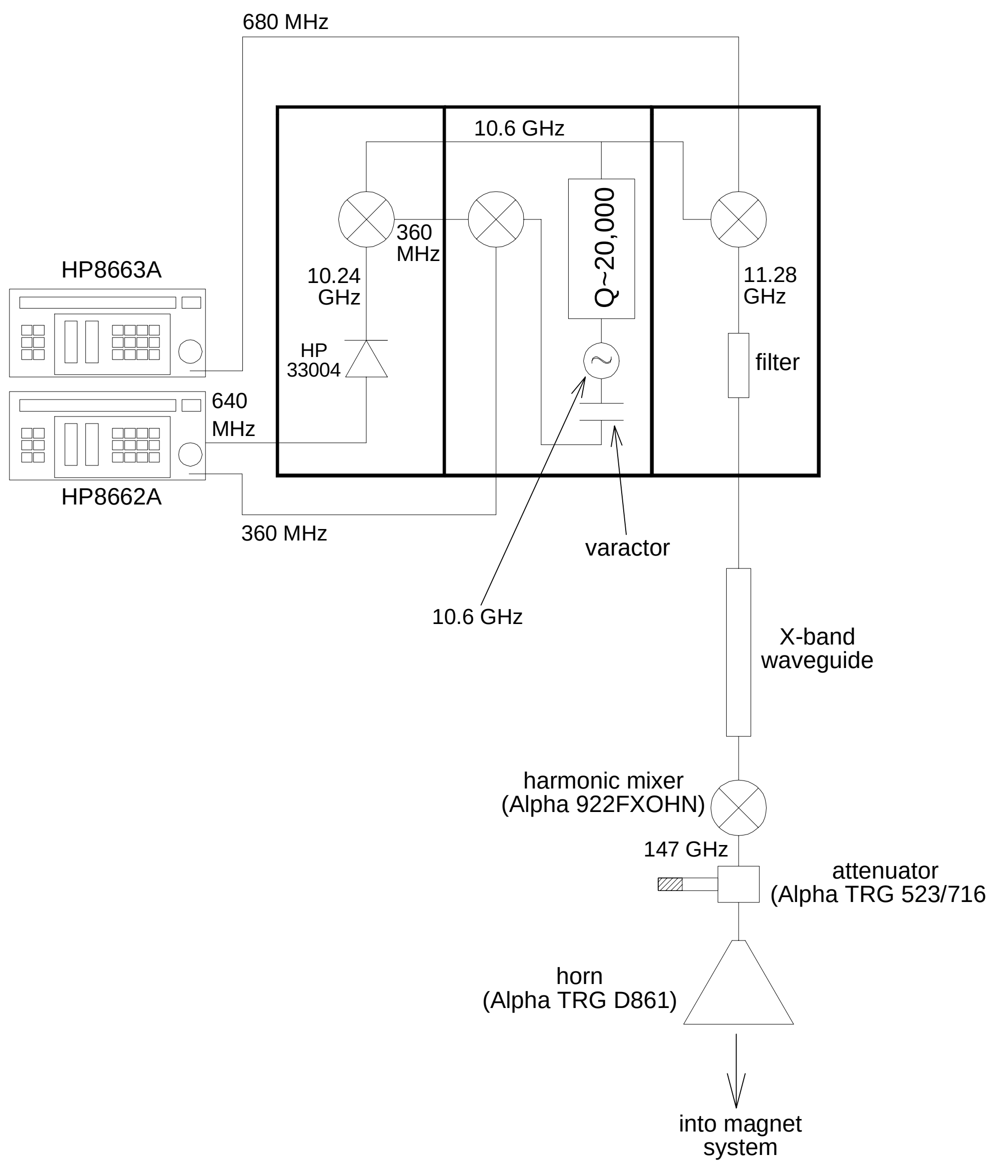

Figure 2.9: Schematic of microwave system.

implement a "housekeeper" seal between the OFHC copper and the pyrex which is designed for thermal cycling to elevated temperatures rather than cryogenic temperatures. Yet, when cooled slowly these seals endure low temperatures. The glass-to-metal assemblies are soldered[5] to flanges which mate to the rest of the vacuum container with an indium seal. After the radiation passes into the trap can, a microwave horn funnels it into an oversized circular waveguide, $\lambda_{cutoff} \approx 5$ mm, which leads to the microwave inlet at the trap. The microwave horn and waveguide can be seen in the enlargement of the base-temperature apparatus shown in Fig. 2.1.

The lens and window system providing direct access to the trap for our 2 mm drive also allows thermal radiation to reach the experiment. The teflon we use for lenses is fairly transparent at 147 GHz yet fairly absorptive at $\approx 10^{13}$ Hz, the frequency at which a 300 K body's thermal-radiation spectrum peaks. Figure 2.10 shows teflon's absorption coefficient versus frequency, with which we estimate a negligible heatload on the trap due to blackbody radiation. In addition to the integrated heat load, a narrow band of this thermal radiation acts as a continual weak resonant drive. Monitoring the cyclotron motion for many hours at 80 mK (where the electrodes radiate no blackbody photons) puts an upper limit of roughly 1 excitation in 4 hours due to this weak drive.

2.3 Trapping Potential

Single-electron experiments require a very stable voltage supply to produce the axial harmonic well. From Eq. (2.1) we can see that jitter in the trapping voltage results

[5] Hard soldering is most reliable for a cryogenic vacuum, but because these seals need to be kept below 400 degrees C, soft soldering is easier. Each method has worked well for us.

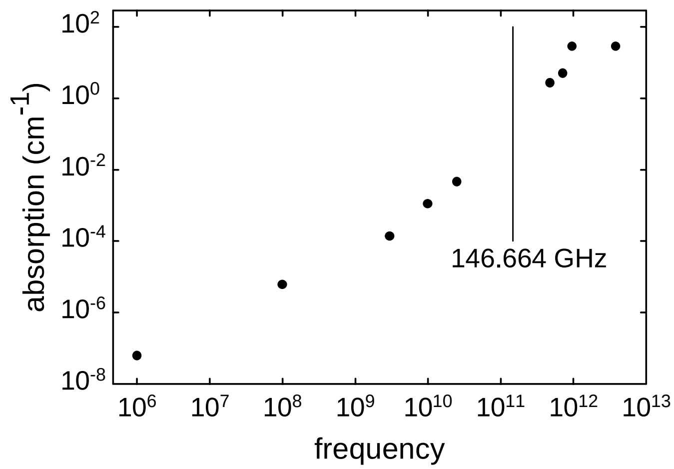

Figure 2.10: Log-log plot of absorption coefficient α versus frequency for teflon. Power transmitted a distance x is given by $P = P_0 e^{-\alpha x}$. Data is from reference [55].

in fluctuations in ν_z,

$$\frac{\partial \nu_z}{\partial V_0} = \frac{1}{4\pi}\sqrt{\frac{e}{V_0 m d^2}(1 + C_2)} \approx 3 \text{ Hz}/\mu\text{V}. \tag{2.5}$$

In the past, mercury/cadmium amalgam unsaturated standard cells were chosen over solid-state supplies to achieve good short-term stability. Typically, 10 Eppley A-2 PYR cells were used in series to generate $V = 10.193$ V [56]. However, standard cells are inconvenient for our application. They need to be temperature regulated at 32 degrees C to 10 mK, and they have a useful lifetime of only about five years. While saturated cells live longer, they have a ten times larger temperature coefficient. The greatest difficulty is that the cells provide only a fixed voltage and cannot be used with a resistive divider because they are unable to continually source the necessary current. This means that the frequency of our cryogenic amplifier must be aligned with ν_z by tugging the inductor.[6] If it is discovered at 4 K that the particle oscillation and circuit resonance are not close enough in frequency, the system needs to be thermally cycled and the procedure iterated.

It is far easier to use a solid-state supply for the trapping potential, either with adjustable output (*e.g.* the Fluke 5440 series) or in conjunction with a high-precision resistive divider (we are fond of the Fluke 732A 10 V reference standard driving a 10 kΩ Kelvin-Varley resistive divider). The particle's axial frequency can then simply be adjusted to match the circuit frequency.

The trap voltage is applied through a cold 10 sec filter, 1 MΩ with 10 pF, to minimize the noise reaching the ring electrode. A polypropylene capacitor [58] is used in order to achieve a high leakage resistance, $R_L \geq 10^{13}\ \Omega$. We have discovered that it is possible for these capacitors to demonstrate $R_L \geq 10^{15}\ \Omega$ at 4 K when handled carefully.[7] This is high enough that a noisy, unstable solid-state supply can be used to charge the capacitor to a particular voltage and then disconnected. The result is a trap voltage that decays slowly with a time constant of $\tau = R_L C \sim 10^4$ sec.

This discharging capacitor will result in a drift in the axial frequency of about 3 Hz/hr $\approx$ 50 ppb/hr. If ν_z is locked to a frequency reference, then the discharging capacitor causes the lock-loop to ramp the correction voltage to keep ν_z fixed, producing a drifting baseline on the data. The voltage decay can even be offset by continually modifying the trap potential using an external integrator. The integrated voltage can be combined with the correction voltage from the lock circuit (or used by itself) and applied to the variable voltage ("var") line. This can be

[6] Varactors, voltage-controlled capacitors that can allow the tuned-circuit frequency to be adjusted *in situ*, may be an alternative solution, though they typically hurt the Q of the resonant circuit. Reference [57] discusses the use of varactors for this purpose.

[7] The leakage resistance can have contributions not only from the capacitor but also from the wires running the length of the cryostat, the room-temperature feedthrough, etc., all of which need to be handled carefully.

done without adding much noise because the "var" line contains a 1:1000 divider, reducing noise and jitter by that much.

2.4 Millikelvin Temperature Production

2.4.1 General Description

A dilution refrigerator uses a mixture of ^{3}He and ^{4}He to achieve low temperatures. Sufficiently below 0.87 K,[8] this isotopic solution separates into two phases, one that is primarily ^{3}He (the "concentrated phase") and one that is primarily ^{4}He (the "dilute phase"). If ^{3}He is removed from the dilute phase, some atoms will diffuse from the concentrated phase in order to maintain equilibrium concentrations. Cooling results from this process because there is an enthalpy difference for a ^{3}He atom in the two phases. The finite fraction of ^{3}He in the dilute component at 0 K, 6.5%, signifies that in principle this provides cooling all the way to absolute zero.

Figure 2.11 shows a model of a dilution refrigerator. The dilute/concentrated phase boundary resides in the coldest part, the *mixing chamber*. The experiment is heat-sunk to this stage through a $\frac{3}{8}$" OFHC copper rod fastened to the refrigerator with an M-6 thread as well as through many experimental leads. Running the refrigerator in "single-shot" mode (during which the ^{3}He removed from the system is *not* re-condensed) and monitoring if and when a lower base temperature is reached provides a check of the location of the phase boundary and thus of the amount and fraction of ^{4}He and ^{3}He. In our case, the "mash" consists of 71 liters of ^{4}He and 16 liters of ^{3}He at STP.

The dilute phase in the mixing chamber is coupled to a reservoir called the *still*.

[8]The temperature varies with ^{3}He concentration.

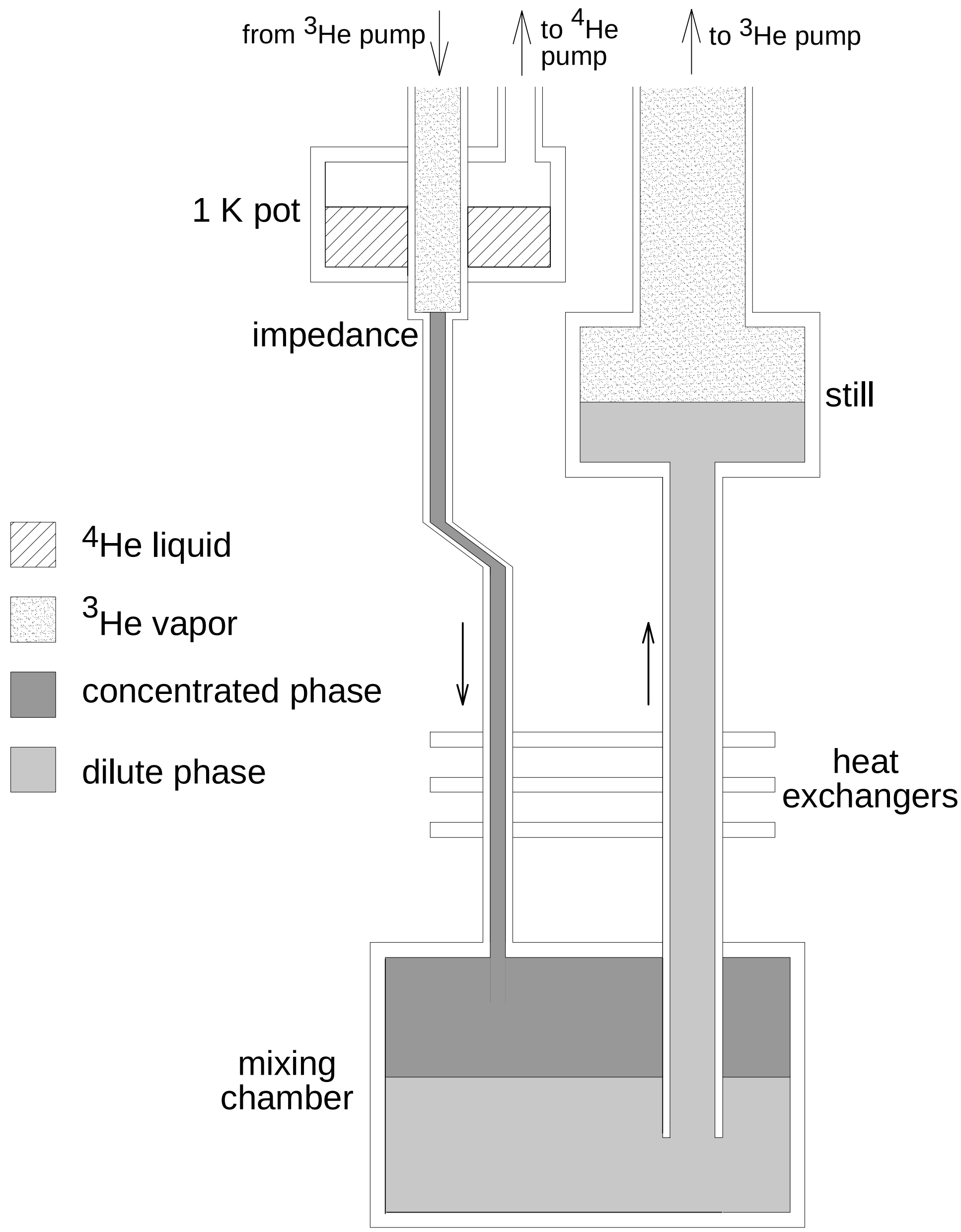

Figure 2.11: Model of a dilution refrigerator.

It is here, with the liquid at its saturated vapor pressure at 600–700 mK, that ^{3}He is removed from the system. Typically several milliwatts of heat are applied to the still in order to reach the optimal circulation rate.

The flow of ^{3}He liquid from the mixing chamber to the still opposes ^{3}He returning to the mixing chamber after being re-condensed into the system. These counter-flowing currents pass each other through two *heat exchangers*, which are designed to provide thermal contact between the two liquids. In this way, some heat flows from the returning helium to the exiting helium, cooling the incoming liquid.

After it is pumped from the system, the ^{3}He passes through cold traps in order to remove any impurities introduced through a small leak or by outgassing in the pump, and is then sent to the condenser of the refrigerator. Here, a separate pumped ^{4}He reservoir, the *1 K pot*, cools the return line to 1.2 K. An impedance in the condenser causes the pressure of the ^{3}He to build so that it can condense at this temperature. The 1 K pot and the dilution unit are maintained in a vacuum region known as the IVC or *inner vacuum chamber*.

2.4.2 Apparatus Details

Our experiment uses an Oxford Kelvinox 300 dilution refrigerator. The compact design (the outer diameter of the IVC is only $3\frac{1}{8}$") provides a nominal cooling power at the mixing chamber of 50 μW at 100 mK when used with a 65 m^3/hr (= 18 l/sec) rotary-vane pump. The cooling power at the trap is considerably lower because electrical-isolation requirements prevent solid metal-to-metal junctions for heatsinking, introducing thermal resistance between the trap and the mixing chamber. When heat $\dot{Q}$ flows from the trap to the mixing chamber, a temperature gradient arises,

$$T_{trap} - T_{MC} = R_{therm}\dot{Q}. \tag{2.6}$$

Formvar-coated constantan wires, 0.003 inches in diameter, run from room-temperature feedthroughs to various stages of the refrigerator for application of DC voltages and RF drives and for temperature measurement. The wire bundles are heatsunk to a post at each stage using GE 7031 varnish [59]. Microcoax lines for the electron signal and anomaly drive are heatsunk to another set of bobbins with Stycast 2850 FT epoxy [60]. These wires and cables contribute a substantial portion of the constant heatload reaching the experiment. We incorporate cold attenuators mounted to the 1 K pot for all of the twisted-pair drive lines to reduce 300 K thermal noise from the 50 Ω source impedance of the RF synthesizers. Standard "T network" values for 20 dB attenuation on 50 Ω lines are used (Fig. 2.12) — the attenuation realized on our lossy transmission line will be different [61].

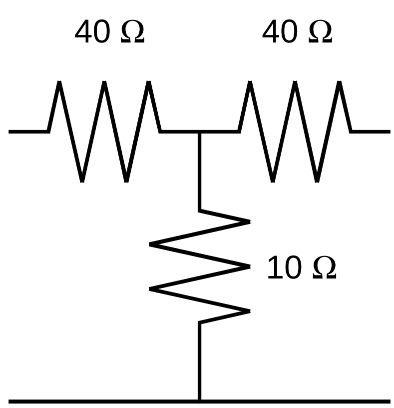

Figure 2.12: Attenuator mounted to 1 K pot.

During dilution refrigerator operation, roughly 30 auxiliary channels are monitored, including temperatures, pressures, and cryogen levels. Labview-based software orchestrates data acquisition through GPIB communication. Temperatures of different stages of the dilution refrigerator and of experimental components are specified by the resistance of RuO_2 chip resistors [62]. These secondary thermometers feature low magnetoresistance, high reproducibility, small size and low cost. Several of our sensors were calibrated versus the nuclear-orientation primary thermometry method using a ^{60}Co<u>Co</u> radioactive source. Additional RuO_2 sensors were calibrated versus these. A low-power resistance bridge, the AVS 46 [63], uses phase-sensitive detection to measure resistances with ample signal-to-noise while generating only several pW of power. Specifically, the power dissipated in a temperature sensor is $P = I^2R$, where the current delivered by the AVS is $I = 2V_{exc}/\Delta R$. V_{exc} is the excitation range and ΔR the resistance range used for the measurement. Four-wire measurements, which factor out the resistance of the sensor's constantan leads, are used for five vital places on the experiment, while we settle for two-wire measurements for the temperatures of various stages of the dilution unit. An SRS 200 amu residual gas analyzer on the IVC pumping port detects the partial pressures of nitrogen and hydrogen as diagnostic levels and of ^{3}He and ^{4}He to monitor the integrity of the vacuum space. The pressures of the condenser line, 1 K pot and still and the ^{3}He flow are all logged electronically during a "run". Appendix C discusses operation of the dilution refrigerator and a history of problems encountered.

The refrigerator is cooled to 4.2 K by a liquid-helium reservoir. We use a 110-liter, 500-pound custom dewar from Nalorac Cryogenics Corporation [64], shown in Fig. 2.13. A boil-off rate of about 6 l/day when the refrigerator is out of the dewar rises to 13 l/day when the refrigerator is in and running. A glue seal in the neck of the dewar has a "permanent" leak between the liquid-helium and vacuum spaces. A 360 degree band of Stycast 2850FT epoxy [60] bonding to both the aluminum plate and G-10 cylinder has been used successfully and repeatedly to achieve a leak-tight patch.

2.5 Particle Confinement and Trap Vacuum

2.5.1 4 Kelvin

The background pressure in a liquid-helium cooled environment can be exceptionally low, on the order of 5×10^{-17} Torr [65]. Penning-trap experiments have achieved this ultrahigh vacuum by enclosing the electrodes in a "trap can" which is evacuated at room temperature, hermetically sealed, and cooled by a liquid-helium reservoir.

We have implemented two different apparatus for our low-temperature trap, shown in Fig. 2.14. The trap in our original setup (2.14(a)–(b)) relied on the vacuum achieved by the cold surfaces of the dilution refrigerator. This design was subsequently improved (2.14(c)) to incorporate a separate vacuum space for the trap. The trap-can system was used to carry out the single-electron work discussed in following chapters which was performed at temperatures between 4.2 K and 70 mK. The separate trap vacuum is needed for our system to confine particles at 4 K because the helium exchange gas used to cool the experiment and dilution unit can never be sufficiently removed.[9] The new techniques involved in preparing our system for 4 K operation are discussed in Section C.3.

2.5.2 Below 4 Kelvin (No Trap Can)

The apparatus shown in Fig. 2.14(a)–(b) has been used routinely to confine electrons when the refrigerator is cooled below 4 K. Cooling just the 1 K pot does not create a high enough vacuum in the trap region to enable particle confinement. If we also

[9]Even if no exchange gas were used, the helium that can diffuse through the room-temperature feedthroughs would in time be detrimental.

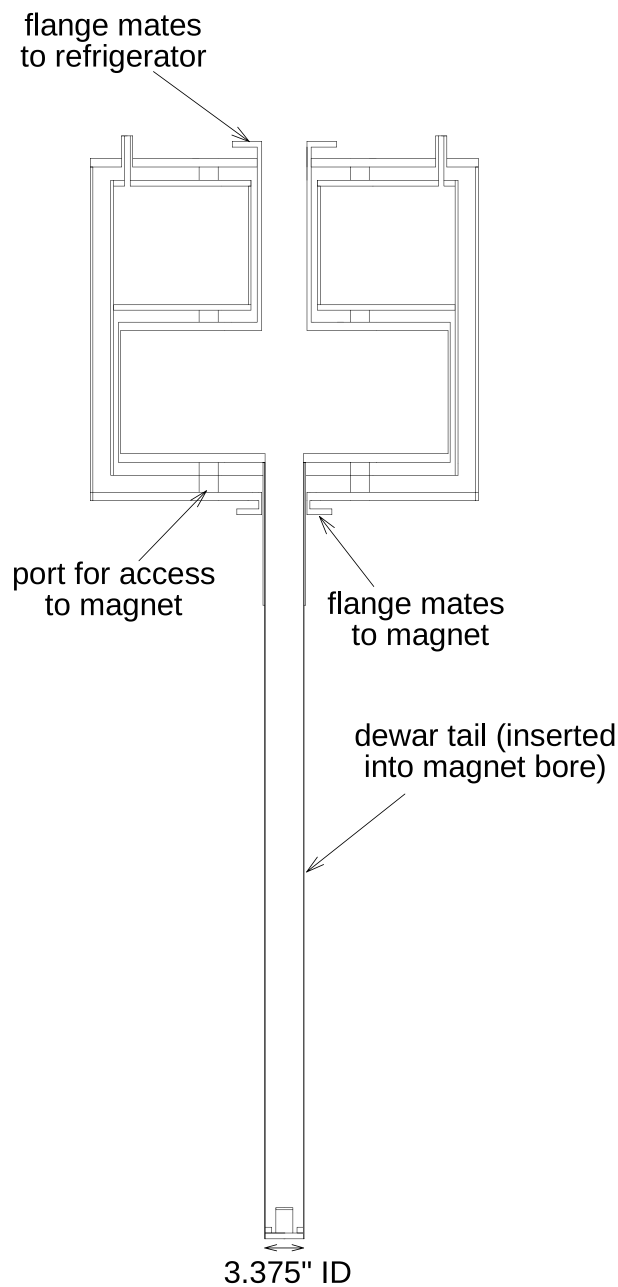

Figure 2.13: Liquid-helium dewar.

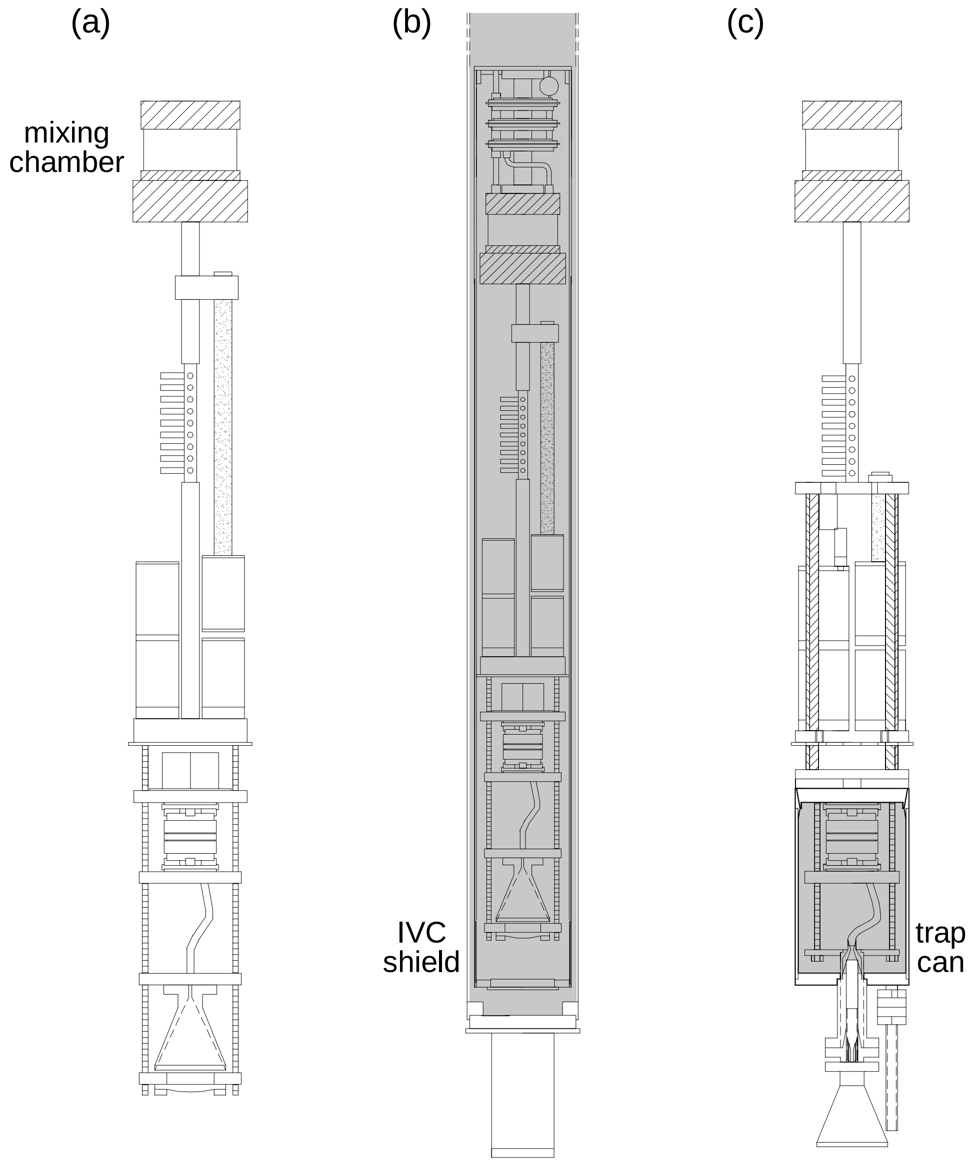

Figure 2.14: (a)–(b) Apparatus that was originally used for confinement below 4 K. (c) Adding a trap can allows confinement at 4 K and alleviates concerns about the trap vacuum in the old design. The vacuum space that determines the pressure within the trap is shaded in (b) and (c). (The drawing in (b) is scaled down by 33% compared to (a) and (c).)

add mash to the dilution unit, it can couple the mixing chamber to the 1 K pot, improving the trap vacuum and enabling particles to be trapped. We observed a lower limit of several hours for the hold time for a cloud of about 5,000 electrons under these conditions, but not much effort went into operating at 1 K since the vacuum is likely not very good.[10]

When the system is cooled to a base temperature of 50–100 mK, the pressure in the vicinity of the trap is expected to be quite low. Figure 2.15 shows the ^{4}He vapor pressure curve derived from data taken at higher temperatures. This is for helium in equilibrium with bulk liquid; in our experiment, the helium is bound to the walls of the system. We routinely trapped electrons at trap temperatures ≤ 100 mK and held the clouds for the duration of the refrigerator runs (only 3–4 days for these runs, which took place before a leak in the IVC was fixed). Our first demonstration of cooling electrons to 50 mK is shown in Fig. 2.16 (the resonances shown in Fig. 2.2 were also obtained with this apparatus).

However, some of the behavior we observed led us to believe that the vacuum in the trap was not as good as the (extrapolated) ^{4}He vapor pressure indicates. For instance, we never succeeded in loading clouds with fewer than several hundred particles — gently throttling the FEP would cause loading to cease completely. Furthermore, we have seen that there can be helium gas in the IVC while the refrigerator surfaces are cold (< 100 mK), which is discussed in Section C.1.1. (The fact that there is ^{4}He gas present in the base-temperature environment while temperatures are ≤ 100 mK is suggestive that simply assigning the ^{4}He vapor pressure to the actual pressure in the system is suspect.)

[10]The 1 K environment *with* a trap can is useful for eliminating thermal excitations of the cyclotron oscillator without running the refrigerator continuously.

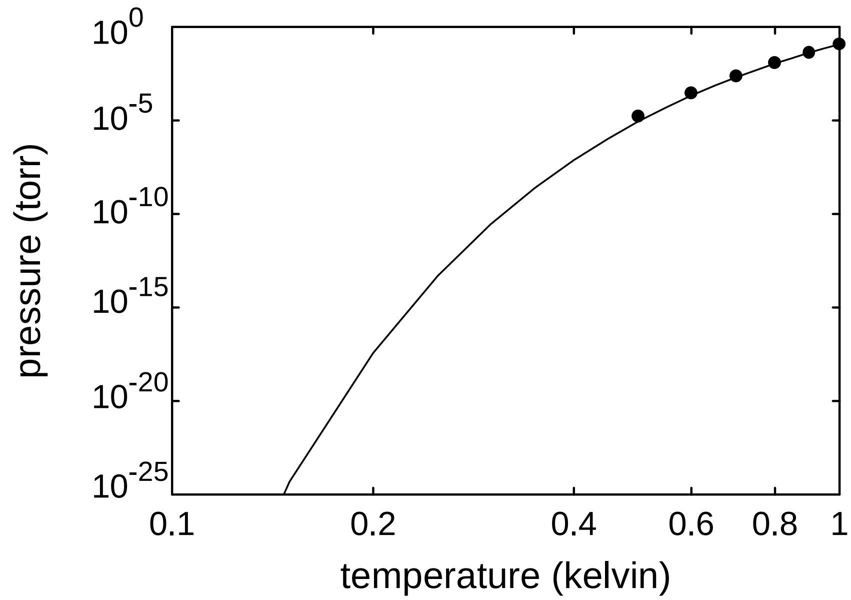

Figure 2.15: ^{4}He vapor pressure versus temperature. Points are data from reference [66]; the curve is a fit to an exponential [67].

2.5.3 Trap Can Design

Compared to brass and stainless steel, OFHC copper has few magnetic impurities, making it the natural choice for construction of the vacuum can enclosing a set of trap electrodes. The space constraints within the dilution refrigerator prevented us from using an indium seal for the trap can because of the room required for flanges and a bolt pattern to compress the indium. Instead, we have implemented a "conical grease seal" which requires very little extra space on the trap-can diameter. This seal is created by forcing a metal plug into a matched metal cone with vacuum grease between the surfaces, as illustrated in Fig. 2.17. Pumping on the volume inside forces the pieces together, and typically the pressure difference maintains force on the two parts of the seal. In our system, however, the trap can is in the

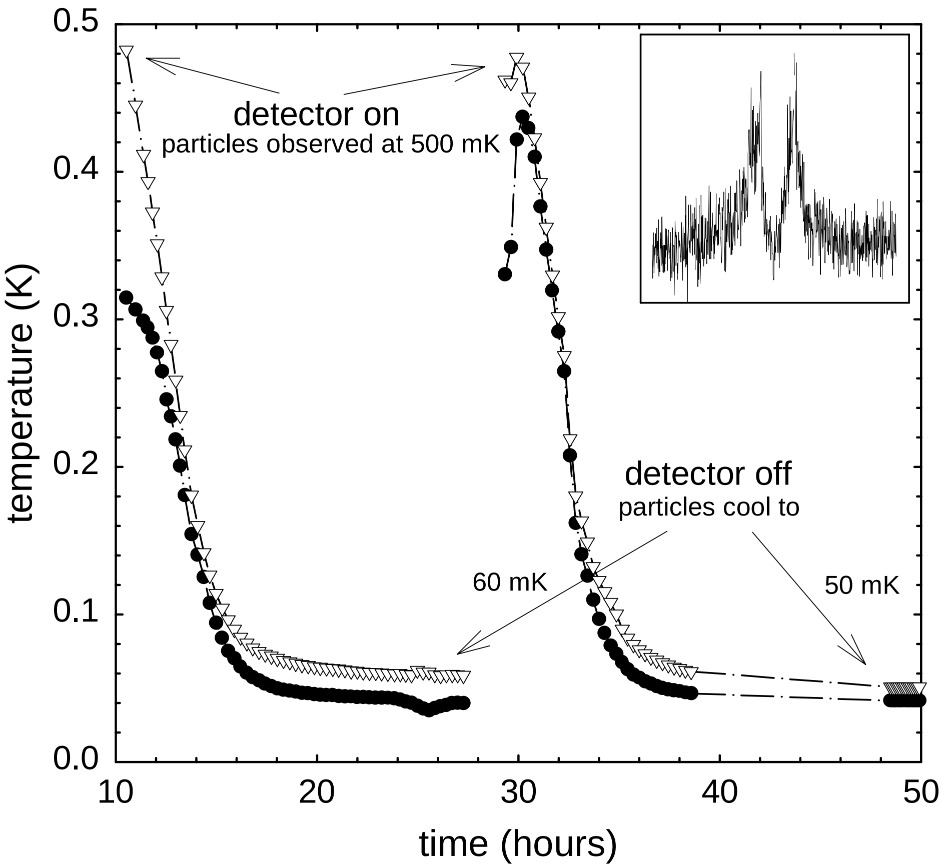

Figure 2.16: Temperature curves for the first demonstration of cooling electrons below 4.2 K. Open triangles indicate the trap temperature and filled circles the mixing chamber temperature as measured with RuO_2 sensors. The inset shows the RF signature of the trapped particles. Solutions to the detector-heating problems that are evident are discussed in the next chapter.

IVC, itself under vacuum, and thus we rely just on the force stored in the metal pieces to preserve the seal. Upon venting, the components can barely be separated by over-pressuring with 12 psi on the inside, indicating that most of the initial force is stored in the metal. We have demonstrated that the vacuum achieved is good enough for experiments with a single electron.

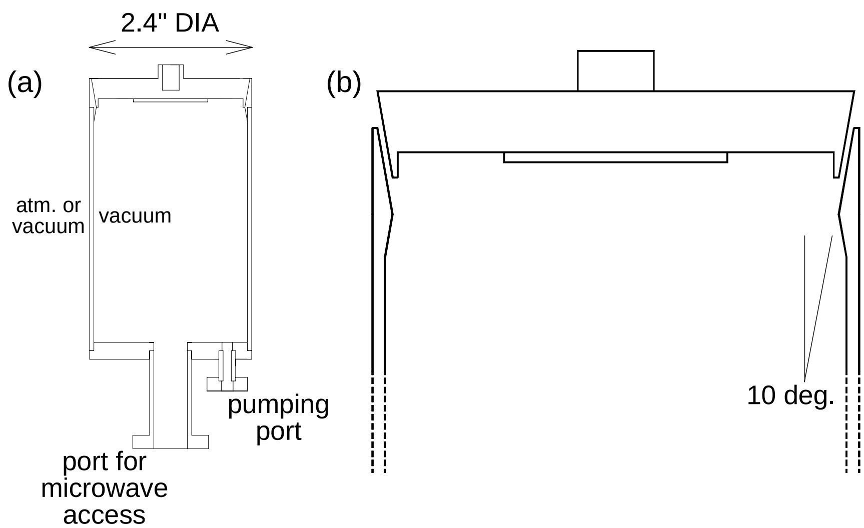

Figure 2.17: (a) Cross section of trap-can assembly. (b) Outline of pieces involved in the conical grease seal.

The surfaces of our cone seal are angled at 10 degrees, the midpoint of the recommended range of 5–15 degrees [59]. The mating pieces need to be lapped [68] in order to achieve the necessary contact between the surfaces. We use Dow-Corning silicone vacuum grease for the seal because non-silicone products such as Apiezon greases are reported to fragment at low temperatures [59].

Our dilution refrigerator is one of the Oxford models that incorporates a grease seal for the IVC. The design has now been discontinued due to unreliable performance. The reliability of our refrigerator's grease seal is discussed in Appendix C.

2.6 Thermal Equilibrium

The electron cyclotron oscillator comes into thermal equilibrium with blackbody radiation in the trap cavity. The temperature of the electrodes determines the number of thermal photons in the cavity which in turn determines the average excitation level of the cyclotron oscillator,

$$T_{trap} \Rightarrow T_{\gamma} \Rightarrow T_{e^-}. \tag{2.7}$$

The rate for the ground-state oscillator to absorb a blackbody photon is given by $\Gamma_{abs} = \gamma_c \langle l \rangle$, where $\langle l \rangle$ is the average number of photons in the cavity,

$$\langle l \rangle = \frac{1}{e^{\hbar\omega/kT} - 1}, \tag{2.8}$$

and γ_c is the damping rate due to synchrotron radiation,

$$\gamma_c = \frac{1}{4\pi\epsilon_0} \left(\frac{4e^2\omega_c^2}{3mc^3} \right). \tag{2.9}$$

In free space, $\gamma_c = (94 \text{ msec})^{-1}$ for our 5.2 T field. (This rate can be modified by the trap cavity and in our case is decreased to $< (10 \text{ sec})^{-1}$.) The cyclotron motion is in thermal equilibrium on the timescale of many absorptions and emissions. Below 1 K, the oscillator is essentially free of thermal excitations; for instance, at 80 mK, $\langle l \rangle = 6 \times 10^{-39}$ and $\Gamma_{abs} = (10^{32} \text{ yrs})^{-1}$. Thus, at the lowest temperatures we reach, the cyclotron motion of the electron is isolated from its environment.

The radiative lifetime of the axial motion of the electron is very long; energy is radiated at a rate of $\gamma_{z,rad} = (10^6 \text{ sec})^{-1}$ [48]. We damp the electron's axial motion by coupling it to an RF tuned circuit. The losses in this circuit act as a reservoir at temperature T_R with Johnson noise stochastically driving the electron and I^2R losses damping its motion. (R is the detector resistance of Section 2.2.1 (recall Fig. 2.5).) The resistive damping rate is [48]

$$\gamma_z = \left(\frac{e\kappa}{2z_0}\right)^2 \frac{R}{m}, \tag{2.10}$$

where $\kappa = 0.79$. We measure $\gamma_z \approx 2\pi(5\ \mathrm{Hz})$ for our system.

Changing the temperature of the axial oscillator requires changing the temperature of R, which depends not only on the temperature of the RF losses in the tank circuit but also on noise sources within the FET. When the transistor is active, these noise sources are at an effective temperature that is above 4 K even when the trap temperature is 80 mK, as we have determined by measuring $T_z \sim 15$ K (see Section 5.1.2). This elevated temperature has been seen in past liquid-helium experiments as well [69, 70]. In some cases, when the FET is cooled by submersion in liquid helium, $T_z \sim 4.2$ K has been measured [51, 71].

Further evidence that the transistor keeps T_z elevated comes from the noise resonance. The temperature of the axial reservoir is proportional to the noise power generated by the resistance R, $V_R^2 = 4k_BT_RR\Delta\nu$. The width of the noise resonance of our RF amplifier reveals R, which can then be used along with the height of the resonance to determine T_R. Extracting an absolute temperature is actually a bit difficult because of unknowns in the RF detection chain, but determining temperature changes is straightforward. We have observed no change in the height of our noise resonance — *i.e.* no change in T_R and thus T_z — as our system cools from 4.2 K to 80 mK.

Thus, realizing a low axial temperature requires turning the FET off and allowing all of the noise sources to cool. The cyclotron and spin systems therefore need to be driven with the FET off; the transistor will be turned on to read out the result of an excitation attempt (Section 5.1.2).

The low-frequency magnetron motion is decoupled from its environment — the radiation rate is $\gamma_{mag,rad} = (10^{14}\ \text{sec})^{-1}$ [48]. This motion is sideband cooled by applying a drive to couple it to the axial oscillator. The limit of the effective temperature achievable by this technique is

$$T_{mag} \approx \frac{\nu_m}{\nu_z} T_z. \tag{2.11}$$

Inserting values for our system at $T_z = 70$ mK gives $T_{mag} \approx 15\ \mu$K.

The spin system is also decoupled from the environment because transitions between the two levels are weak magnetic dipole transitions. The higher energy spin eigenstate is stable against decay for $\sim 10^{11}$ sec [48].

Chapter 3

Low-Power Detection

An electron confined in our Penning trap oscillates in the electrostatic well at 64 MHz for a trap voltage of 10.2 V. The image current induced in the trap electrodes by the oscillating charge is detected and processed. This RF signal provides information not only about the electron's axial motion, but also about its cyclotron and spin states. At frequencies near 150 GHz, the motions of these magnetic states are difficult to monitor directly. Instead, they are intentionally coupled to the axial oscillation (Section 4.1), which is used to extract all pertinent information about the electron.

The amplifier used to monitor the RF motion typically employs a transistor that generates more heat than is tolerable for the mixing chamber of a dilution refrigerator. This required us to develop low-power detection techniques. In particular, we have collaborated with condensed-matter colleagues to develop a cryogenic, RF field-effect transistor (FET) fabricated from a specially grown GaAs/AlGaAs heterostructure [30]. This FET has been used for experiments with a single electron in a Penning trap cooled to an unprecedented 80 mK.

Techniques for detection of this induced RF current are of general use to the ion-trapping community, and thus the improvements presented in this chapter in terms of detection of the axial motion of an electron have a broad applicability. While some trapped ions are probed optically, subatomic particles reveal themselves only through the current they induce in the trap electrodes. Even ion mass-spectrometry experiments [72] measure the current induced by the ion's oscillations to determine mass ratios. Furthermore, particles other than electrons and positrons have a cyclotron frequency that is in the RF range or lower, making this motion directly detectable using the same techniques as for an electron's axial motion [73].

3.1 Overview of RF Detection

An oscillating electron induces in the trap electrodes a current given by [48],

$$i = \left(\frac{e\kappa}{2z_0}\right)\dot{z}, \tag{3.1}$$

where the geometrical factor κ is 0.79 for our trap. We detect this electron current with a tuned amplifier connected to the trap electrodes. The amplifier consists of a high-frequency transistor and a coil which forms a tank circuit with the capacitance of the electrodes, as shown in Fig. 3.1(a). The coil inductance, trap capacitance, and RF resistance form an LCr detection circuit designed to resonate at $\nu_{LC} = \nu_z$. Near resonance, the RF resistance r in the tank circuit can be treated as an effective resistance, $R = L/rC$, in parallel with L and C (recall Section 2.2.1). At ν_z, the reactances of L and C cancel and the trapped particle sees just the resistive load, which in terms of the quality factor Q of the circuit is [48]

$$R = Q\omega_z L. \tag{3.2}$$

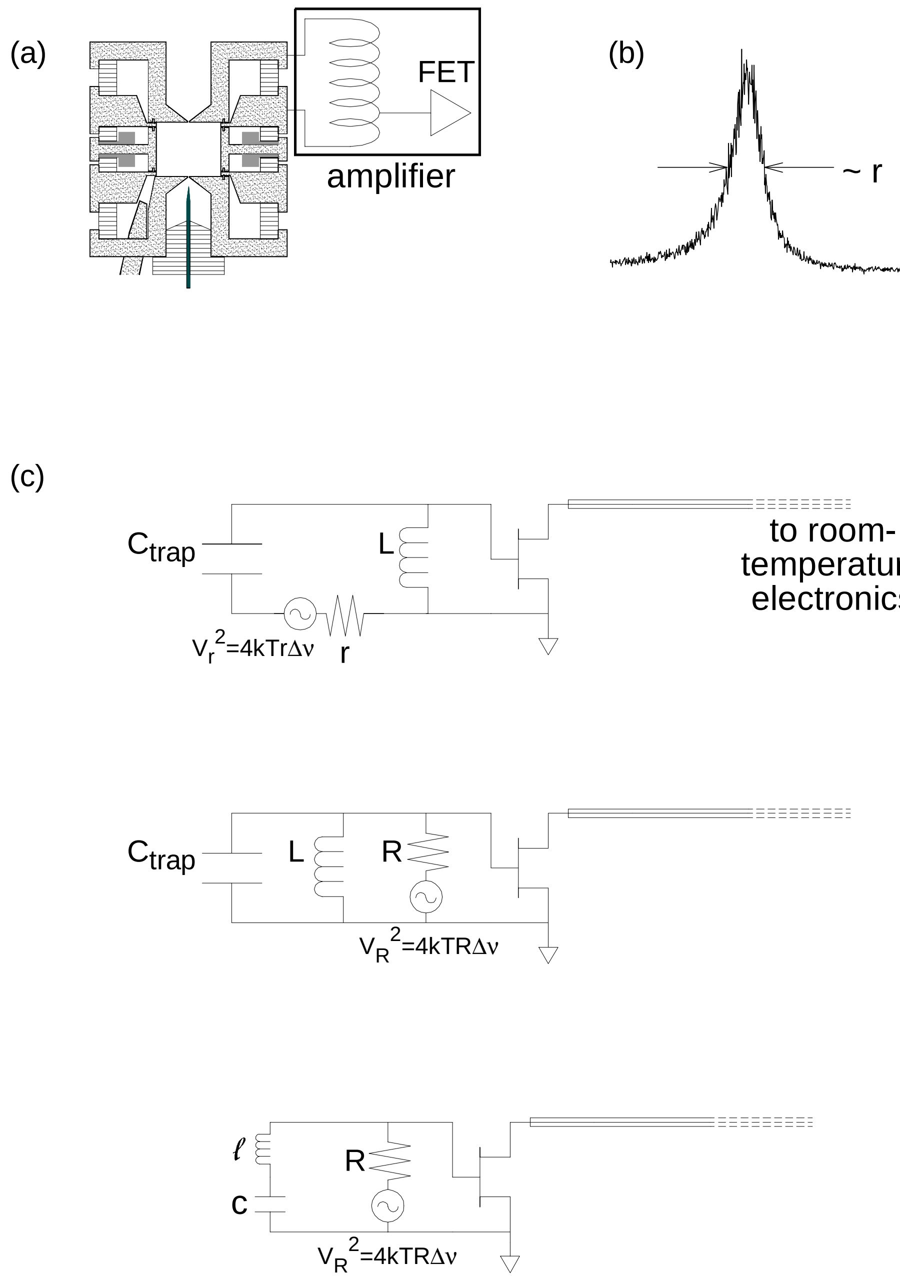

Figure 3.1: (a) Trap and amplifier. (b) Noise power spectrum characterizing tuned circuit. (c) Three schematics of detection circuit. The RF resistance, r, of the tank circuit can be written in parallel with L and C as $R = L/(rC)$ near resonance. The reactances of L and C cancel at $\nu_{LC} = \nu_z$; a trapped particle, modeled as a series lc circuit [74], sees just the effective resistance of the circuit.

Maximizing this resistance (minimizing the RF losses in the detection circuit) optimizes the signal-to-noise of the amplified electron signal.[1] The voltage drop across this resistor is capacitively coupled to the gate of the FET which is matched to a microcoax for transmitting the signal to room-temperature amplifiers. Figure 3.1 outlines the RF detection; the FET bias circuit and matching network are shown in Fig. 3.2.

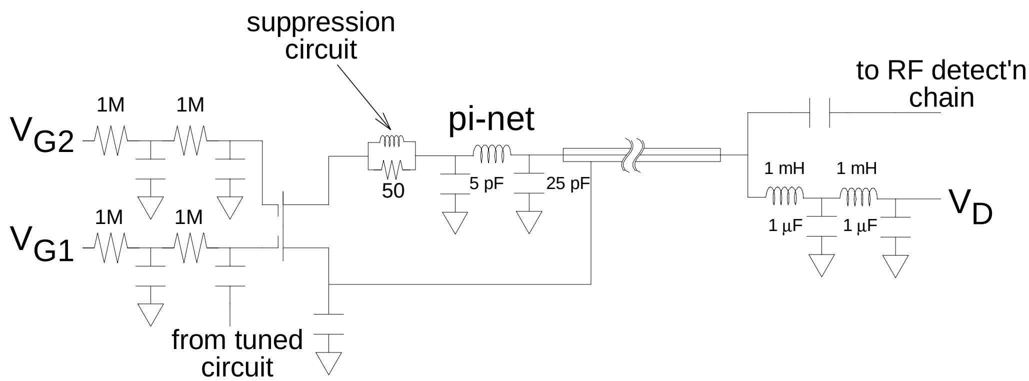

Figure 3.2: Schematic of FET bias circuit. All capacitors are 1000 pF except for those labeled. A complete representation of the detection chain is shown in Fig. 2.7.

The transistor and the RF losses in the detection circuit generate Johnson noise which drives the LC circuit, producing a noise resonance (Fig. 3.1(b)) with a center frequency of $\nu_{LC} = 1/(2\pi\sqrt{LC})$ and a power spectrum with a full-width at half-maximum of $\Delta\nu = \nu_{LC}/Q$. An electron's axial frequency,

$$\nu_z = \frac{1}{2\pi}\sqrt{\frac{eV_0}{md^2}\,(1 + C_2)}, \tag{3.3}$$

and the tuned circuit frequency are made resonant by either tuning L or adjusting

[1] This resistor has an associated thermal noise source which degrades the final signal. Since $V_{signal} \propto R$ and $V_{noise} \propto \sqrt{R}$, the amplitude signal-to-noise achieved depends on this resistance as $\sqrt{R}$ [48].

V_0, depending on the particular experiment.[2] The oscillating electron, in a fashion reminiscent of a series lc circuit [74], shorts out the Johnson noise at ν_z, creating a "dip" in the tuned-circuit resonance (Fig. 3.3(a)–(b)). This dip is the most pristine particle signature because it does not require application of any excitation drives. However, for a single electron it is often desirable to improve the achieved signal-to-

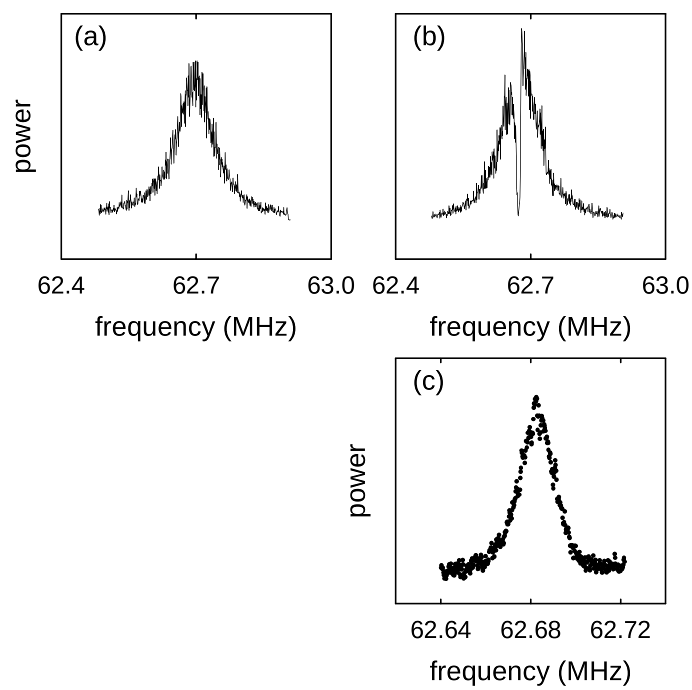

Figure 3.3: (a) Driven tuned-circuit resonance with no electrons in the trap. (b) "Dip" in resonance due to about 500 electrons, which short out the signal driving the circuit. (c) Driven response of the 500-electron cloud.

noise ratio and to measure shifts in the axial frequency (Section 2.2.1) by driving the axial motion and synchronously detecting the particle's response (Fig. 3.3(c) and Section 2.2.1).

[2]Variable voltage supplies make tuning ν_z trivial, but typically single-electron experiments require stable, low-noise standard cells for application of V_0. This demands manually adjusting L by compressing or stretching the coil. Section 2.3 discusses a welcome alternative.

The amplifier is constructed with a silver-coated copper coil housed in a cylindrical can for shielding. Cooling the entire amplifier to low temperatures reduces both the RF losses and the thermal noise generated. A "suppression circuit", a 50 Ω resistor wrapped with five turns of wire, dissipates high-frequency signals which could otherwise couple to the input and cause regeneration (Fig. 3.2). Additionally, isolating the gate and drain leads from the circuit board in the amplifier is typically required for the most stable operation.

3.2 Inductive Coupling

The MESFET typically used in 4 K systems generates several milliwatts of heat. The coupling of the electron signal to the transistor's gate is achieved with a copper strap soldered to the inductor at a certain point along the coil, providing a direct path for conduction of heat from the FET to the trap electrodes. In an attempt to continue using transistors at this power dissipation, we designed a transformer-coupled amplifier. A pick-up coil, physically separated from the inductor of the tuned circuit, couples the RF signal to the FET while eliminating the heat conduction path between the transistor and the trap electrodes. The two amplifier designs are illustrated in Fig. 3.4(a) and Fig. 2.4.

In addition to the thermal isolation provided by this new amplifier, the less-than-unity coefficient of coupling of the transformer may be able to provide more stringent electrical isolation between the FET and the trap than the auto-transformer of the 4 K design. This would be helpful for minimizing the loading of the tuned circuit by the real part of the FET's input impedance at 60 MHz and for reducing the amount of noise from the FET that reaches the endcap and can stochastically drive the electron.

3.2.1 Reduced Trap Temperature

With the inductive amplifier, the only physical contact between the FET and the base-temperature region is through a hollow (.035 inch wall) G−10 support rod, several inches long,[3] connecting the copper shield around the FET circuit to the mixing chamber. The amplifier uses two coaxial coils, the secondary hanging inside the primary. A copper microcoax, whose shield is soldered to the FET's source, runs unanchored from the preamp region, along a machined groove in the cold shield, to the still (Fig. 3.4(b)).

We intended for this heatsinking scheme to direct all of the heat generated by the FET to the still to optimize the ^{3}He circulation rate and avoid increasing the base temperature. This goal went unrealized due to unexpected heat transfer to the mixing chamber and experiment. When the detector dissipates 3 mW, all of the temperatures in the base-temperature region rise dramatically (recall Fig. 2.16), with the copper shield around the FET circuit reaching an alarming 22–23 K (Fig. 3.5). The elevated base temperature may be due to heat conduction through the G-10 support rod, which is much greater than anticipated as a result of the high temperature of the amplifier shield. This could be responsible for close to 1 mW of heat transfer. Furthermore, with surfaces as warm as 20 K, it is possible that a locally bad vacuum is partially to blame. For instance, helium atoms acting as an exchange gas might contribute to the elevated temperature.

Some of the heat from the FET *is* successfully diverted away from the trap. We have seen that when we operate the transistor at 15 μW (see Section 3.3.1), our method of heatsinking allows a lower trap temperature, by about 40% at 100 mK. The two amplifier designs were tested during the same refrigerator run, giving the

[3]Two versions of this support stalk were used, one two inches and the other six inches in length.

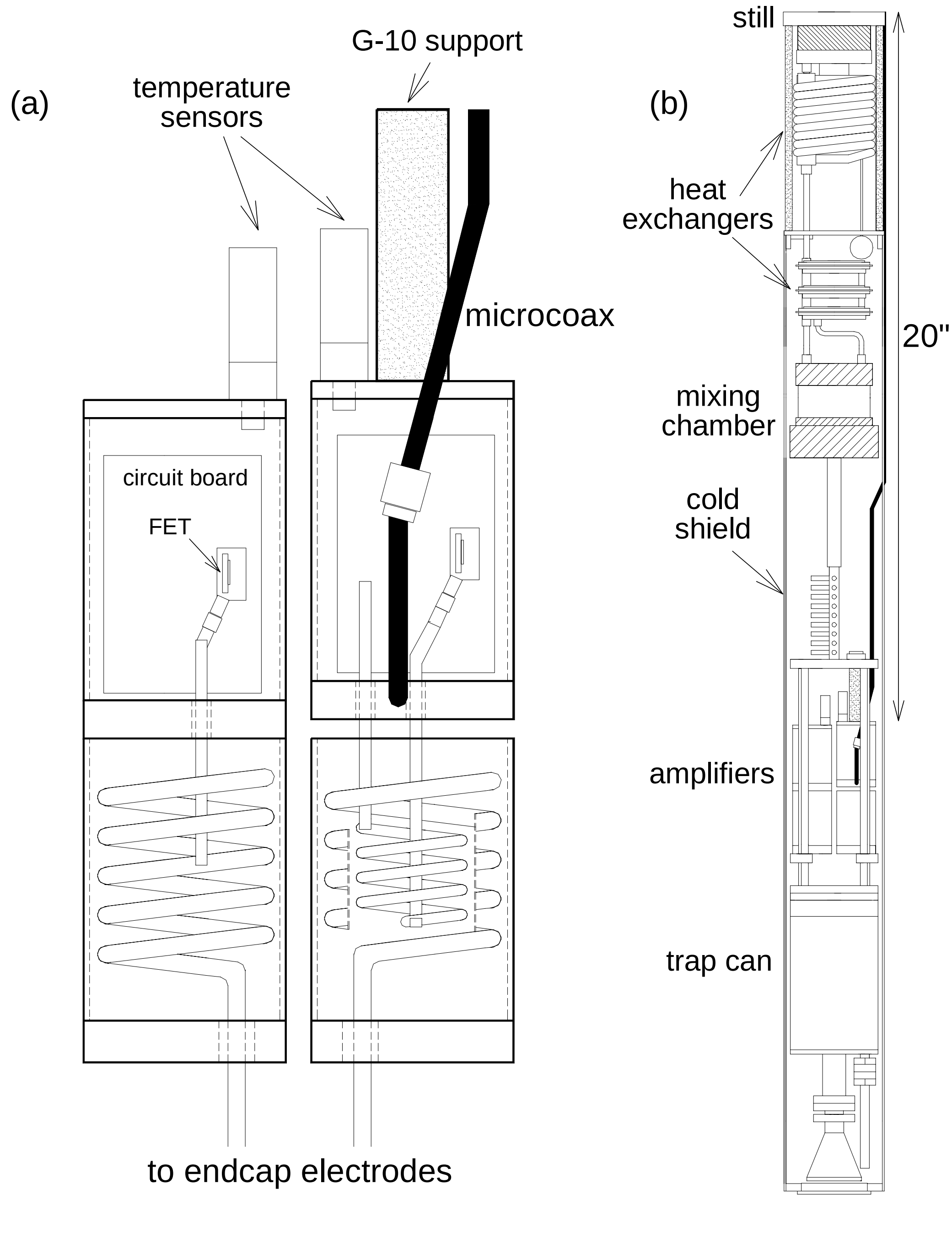

Figure 3.4: (a) Detailed view of amplifiers, with "directly coupled" amplifier on the left, "inductively coupled" amplifier on the right. The primary coil in the inductive amp is "cut away" to expose the pick-up coil. (b) The microcoax heatsink extends about 20 inches from the amplifier in the base-temperature region to the still.

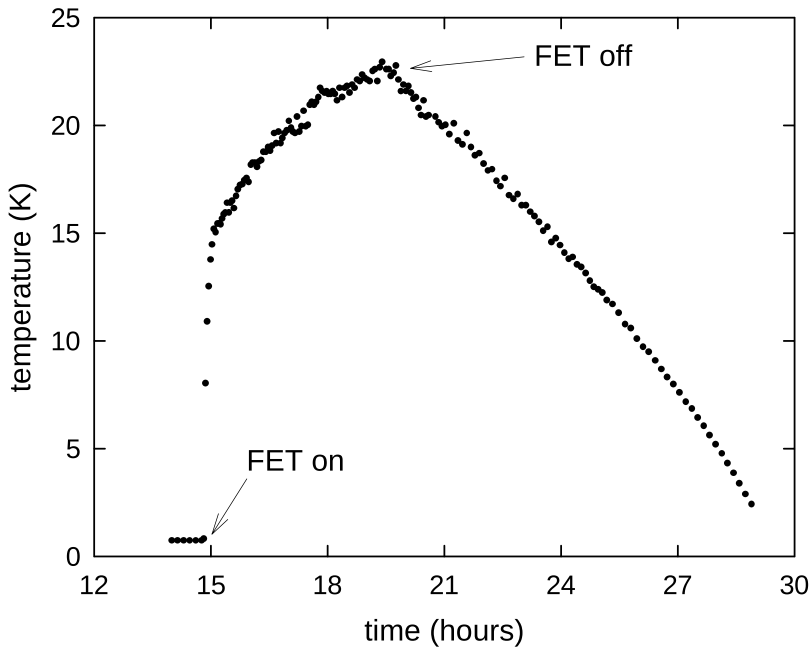

Figure 3.5: Temperature of amplifier can when the FET is dissipating 3 mW.

results shown in Table 3.1. Even at this low power, the copper amplifier shield is heated above 1 K.

3.2.2 Instabilities

Any circuit which provides gain and in which there is coupling between the output and the input is potentially unstable. For an RF amplifier, capacitive pickup (which can be aided by unintended resonances) is an unavoidable source of coupling. The design of our tuned amplifiers needs to account for potential instabilities.

We have observed a greater tendency for unstable operation with our inductively coupled amplifier than with our directly coupled design. The leakage inductance due to the imperfect coupling between the transformer coils can resonate with, for

Coupling	Power	Trap Temp.	MC Temp.	Amp. Temp.
inductive	3 mW	> 500 mK	> 320 mK	> 22 K
inductive	15 μW	77 mK	49 mK	1.2 K
direct	15 μW	118 mK	79 mK	

Table 3.1: The inductively coupled amplifier directs some heat away from the trap. The "greater-than" signs indicate that the system never quite reached equilibrium subjected to a 3 mW heatload. (The directly coupled amplifier enclosure lacked a RuO_2 temperature sensor during this run.)

example, the FET capacitance and lead to oscillations [75]. For a 0.83 inch long primary coil with eight turns and a diameter of 0.55 inches, a secondary coil with a length of 0.8 inches, four turns and a diameter of 0.375 inches seems to provide ample coupling and stable operation down to 4.2 K. Smaller-diameter coils, which are less likely to make contact with the primary coil, create a transformer with too much leakage inductance. Larger coils tend to load the primary tuned circuit and are difficult to keep physically isolated.

Occasionally we have noticed that a low-Q (< 100) resonance appears at 70–90 MHz, tens of megahertz above the primary resonance, during stable room-temperature operation of an amplifier that regenerates at low temperatures. This resonance may correspond to the frequency which causes the instability, which would make it useful as a diagnostic at room temperature. Simulations of the behavior of a transformer-coupled amplifier show a secondary resonance that moves higher in frequency as the coefficient of coupling is increased, further suggesting that the low-Q resonance observed is correlated with instability.

3.3 Commercial GaAs MESFET

An FET that has been used to a great extent in 4 K Penning-trap experiments is a commercial GaAs MESFET, Mitsubishi model MGF-1100. The MGF-1100 is a depletion-mode, n-channel FET with 1 μm-long by 200 μm-wide Schottky metal electrodes in a dual-gate configuration. Optimal performance requires a 3 V drain-source bias and the gates biased to give a drain current of > 10 mA. In order to reduce liquid helium boil-off, the FETs are typically used at $I_D \approx 1$ mA, reducing the transconductance from 15 mS to around 10 mS. This 3 mW is still too much heat to dissipate in the base-temperature region of a dilution refrigerator; further "starving down" is required. Although the performance is degraded, these FETs can be used at powers down to tens of microwatts for some low-temperature applications.

3.3.1 Characterization and Applications

Drain characteristics for the MGF-1100 at liquid-helium temperatures are shown in Fig. 3.6(a). At powers that are compatible with our system, the device operates in the "linear" region (Fig. 3.6(b)), diminishing the transconductance.

"Starving-down" this commercial FET to tens of microwatts degrades its performance so much that a different solution is needed for our single-electron experiments, which is the subject of the next section. There are, however, at least three situations in which the throttled MESFET might suffice. If the experiment being performed involves clouds of "many" particles, can operate at several hundred millikelvin, or uses a refrigerator system with higher cooling power than ours, then the commercial device may be adequate.

It is easier to detect the signal from a cloud of electrons than from one. Anharmonicity in the electrostatic potential limits the amplitude to which a cloud can

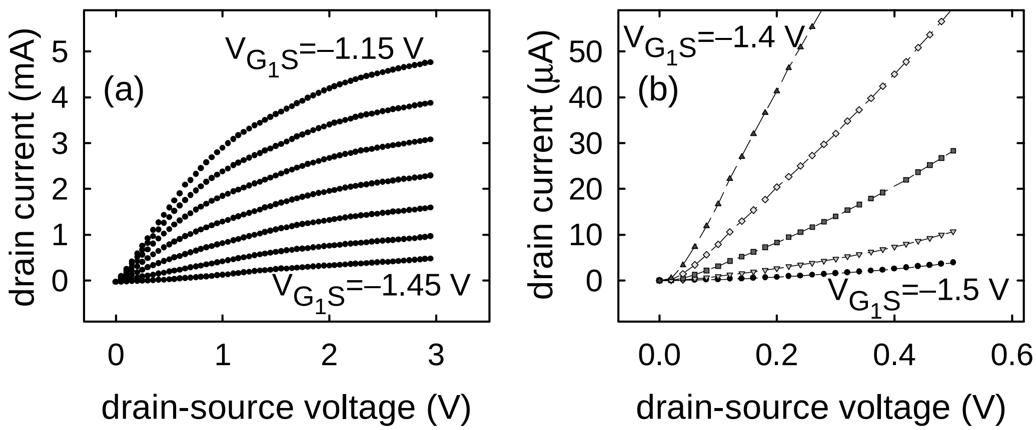

Figure 3.6: Drain characteristics for the Mitsubishi MGF-1100 MESFET at 4 K. (a) $I_D - V_{DS}$ curves for typical operating parameters, with gate 2 grounded and V_{G_1S} stepped in 50 mV increments. (These curves are for currents lower than specs, but typical for operation in 4 K experiments.) (b) Low-power region of drain characteristics with gate 2 grounded and V_{G_1S} increased in 25 mV increments.

be excited, *i.e.*, one cannot drive the particles arbitrarily close to the electrodes in order to increase the induced current. For a given oscillation amplitude, the image current is proportional to particle number, and therefore the sensitivity of the FET is less crucial for larger clouds. Figure 3.7 shows several driven resonances from a cloud of about 30 electrons using the MESFET starved to three different powers. From this figure, it is reasonable to believe that this FET at 70 μW could suffice for detection of a cloud of 30 electrons (which is a relatively small cloud). Examples of experiments involving clouds rather than a single particle are cold-electron plasma studies (see Appendix B) and hydrogen and antihydrogen [39, 76] production.

The production of hydrogen or antihydrogen in a nested Penning trap [39, 76] may not require the lowest temperatures achievable with a dilution refrigerator. The expected production rate for collisional recombination exhibits a $T^{-9/2}$ temperature dependence [39]. With this sensitivity, an equilibrium temperature of several

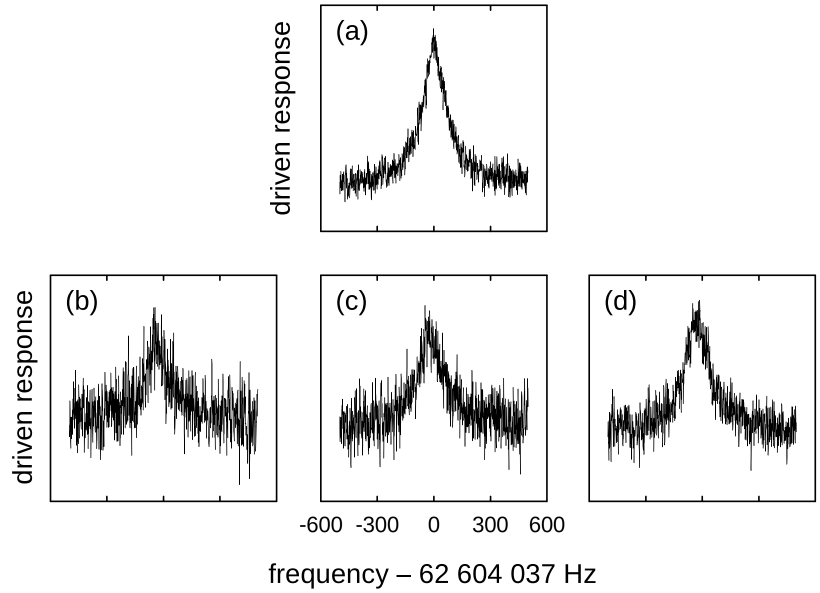

Figure 3.7: Driven resonances of a 30-electron cloud, taken with the MESFET throttled to three different powers. The powers and full vertical scales are (b) 10 μW and 1 V, (c) 25 μW and 1.1 V, and (d) 67 μW and 1.5 V. The response obtained using the conventional $I_D = 1$ mA (1 μW dissipation) is shown in (a) as a reference, with a full vertical scale of 3.1 V. (These are traces used in the comparison shown in Fig. 3.19.)

hundred millikelvin may suffice to achieve the desired formation rates.

Designed for precision measurements, our refrigerator system was constructed to fit into the 10 cm bore of a highly uniform superconducting solenoid. This necessitated a compact refrigerator with a very slim pumping line. In addition, we circulate ^{3}He with a rotary-vane pump to avoid the vibrations that a roots blower might introduce. The result is that our system achieves modest cooling power, about 50 μW at 100 mK at the mixing chamber. Since heatsinking of the trap cannot be done without introducing some thermal resistance between the trap and the mixing chamber to maintain electrical isolation, the cooling power at the trap is even lower. If the system is upgraded (*e.g.* the addition of a roots blower) or if future dilution refrigerator-cooled Penning-trap systems achieve higher cooling power, the MGF-1100 may be able to be used at high enough power dissipation to be effective.

3.3.2 Optimization Procedure

To maximize the utility of these commercial devices, we developed a procedure to optimize the DC transconductance g_m for a given power dissipation.[4] For an ideal FET, power minimization dictates biasing the drain close to its saturation value; the optimal paramaterization is given by $(V_{DS,sat}, I_D)$ which satisfy

$$I_D = kV_{DS,sat}^2 = k(V_{GS} - V_P)^2, \tag{3.4}$$

where k is an FET-specific parameter and V_P is the pinch-off voltage. This is just the curve that serves as the boundary between the "linear" and saturation regions of the FET's $I_D - V_{DS}$ curves (see Fig. 3.8(a)). In practice, this boundary is not well-defined for these MESFETs at the powers of interest (Fig. 3.6), and thus the choice of parameters that optimize the low-power performance is a more subtle one. We used the following procedure.

1. For a given V_{DS}, g_m is mapped out versus I_D. This curve exhibits a maximum at some current. (For an ideal FET, g_m versus I_D should become constant when the current becomes high enough that the device is no longer in the saturation region; in this case [77],

$$g_m = \frac{\partial I_D}{\partial V_{GS}} = \frac{\partial}{\partial V_{GS}} \left(2k\left[\left(V_{GS} - V_P\right)V_{DS} - V_{DS}^2/2\right]\right) = 2kV_{DS}. \tag{3.5}$$

— see Fig. 3.8(b).)

[4]This can be extrapolated to 60 MHz since we have verified $g_m(DC) = g_m(60\text{ MHz})$.

2. This plot is converted to a transconductance versus power map by scaling the x-axis by V_{DS}.

3. Putting all V_{DS} curves on the same plot allows the optimal V_{DS} for a particular power dissipation to be determined.

This is represented graphically in Fig. 3.9 for the MGF-1100; the results are listed in Table 3.2.

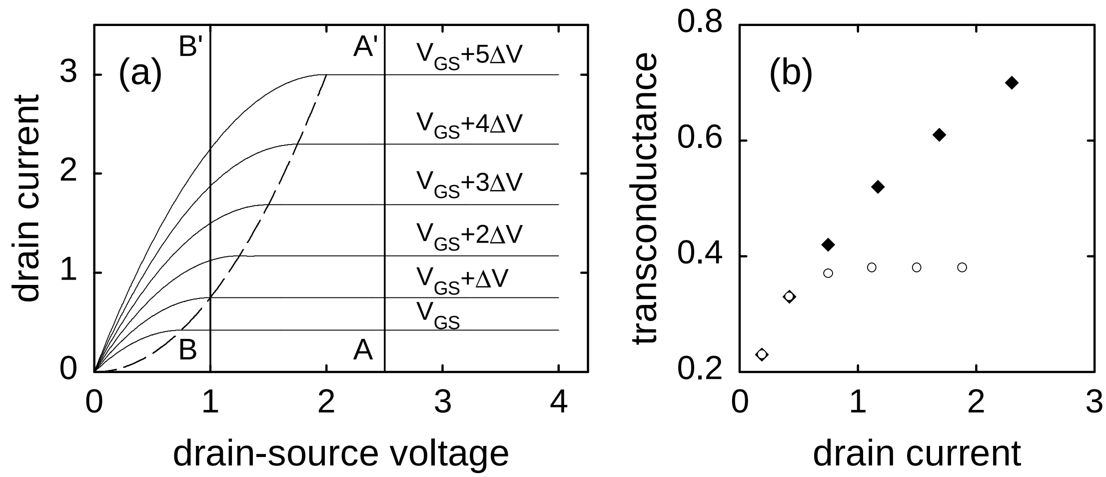

Figure 3.8: (a) Drain characteristics for an "ideal" FET. The dashed line (Eq. (3.4)) displays the boundary between the linear and the saturation regions. Increasing I_D along A–A' increases the transconductance as $\sqrt{I_D}$, shown in (b) with the solid diamonds. Along B–B', the transconductance becomes constant as the dashed line is crossed, signifying the device is no longer in the saturation region (open circles in(b)). For physical FETs, the transconductance will begin to decrease after reaching its maximum value.

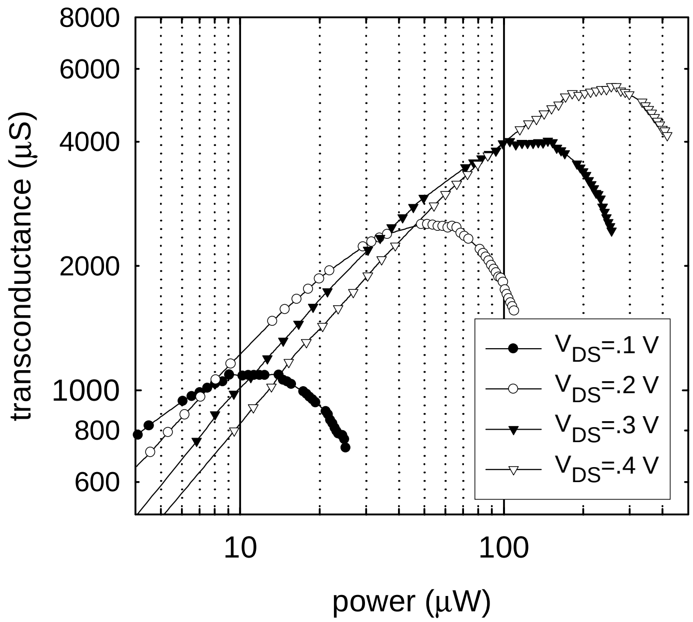

Figure 3.9: Transconductance-versus-power curves for different drain-source voltages. There is a power interval in which each V_{DS} shown is the optimal value. Just a portion of the optimization data set is shown; all of the results are compiled in Table 3.2.

Power (μW)	**Optimal V_{DS}**
2–8	0.1
8–30	0.2
30–80	0.3
80–200	0.4
200–400	0.5
400–800	0.75
800–2000	1.0
2000–3000	1.5

Table 3.2: Results of optimization of low-power transconductance of MGF-1100.

3.4 Cryogenic HFET

FETs specifically designed to operate at low powers and cryogenic temperatures have been fabricated and studied by the research group of R. M. Westervelt at Harvard's Gordon McKay Laboratories. A device designed in 1994 by D. J. Mar *et al.* [78] exhibited low-noise, high-sensitivity operation at ≈ 1 μW power dissipation using a heterostructure with an accumulation layer. That FET operated in the unsaturated regime and exhibited a bandwidth of about 2 MHz. R. G. Beck has fabricated a high-frequency cryogenic FET with a quantum well which provides more confinement for hot electrons than the single hetero-interface, allowing this transistor to operate in the velocity-saturation regime. This device was used for the data in this thesis and is still in use in our apparatus.

3.4.1 HFET Design

The FET is constructed from a wafer grown by A. C. Gossard and K. Maronowski at U. C. Santa Barbara using molecular beam epitaxy [79]. The semiconductor consists of a bulk $Al_{0.3}Ga_{0.7}As$ substrate upon which is grown a sequence of GaAs and $Al_{0.3}Ga_{0.7}As$ layers. These layers create a heterostructure[5] featuring a potential landscape with a quantum well in the z-direction (the growth direction — see Fig. 3.10). Electrons from silicon donors reside in this well, with their motion constrained in the z-direction but unimpeded in the x- and y-directions. This charge configuration is known as a two-dimensional electron gas (2DEG), and has been a tool for several historical experiments [81, 82]. The 2DEG in our FET has a sheet density of 2×10^{11} cm^{-2} and an electron mobility of 1.5×10^5 cm^2/(V $\cdot$ sec) at 4.2 K,

[5]Hence the name HFET, for "heterostructure FET", in reference to its semiconductor composition [80]. Other acronyms can be found in the literature, *e.g.* HEMT, which stands for "high electron-mobility transistor". The former label has been chosen because it is less general than HEMT, which can refer to devices of various compositions.

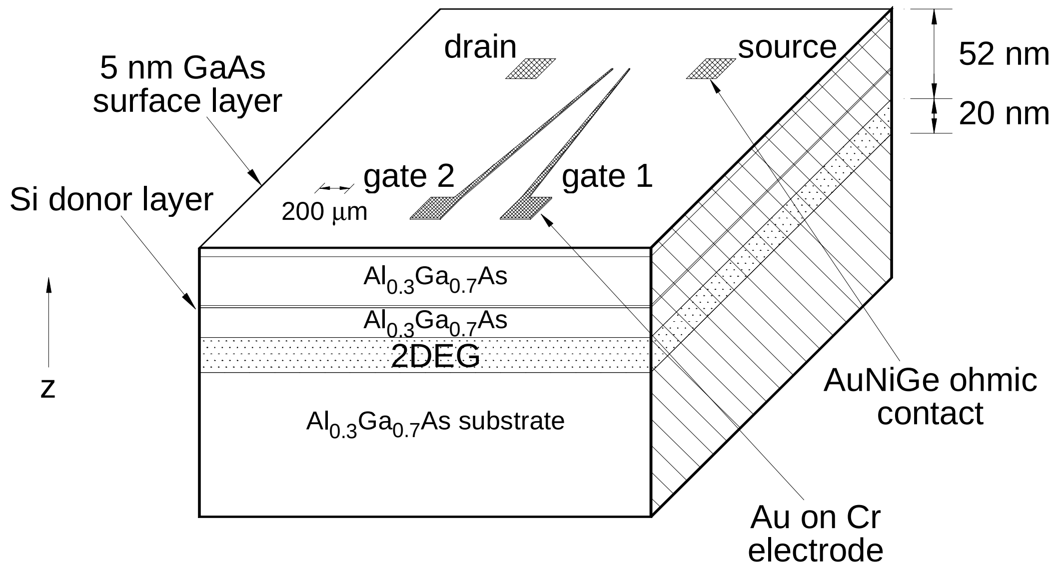

Figure 3.10: Representation of HFET, displaying fabricated design and heterostructure properties. Note that the planar and vertical scales are different.

and resides in a 200 Å square well beginning 520 Å below the surface. (Reference [80] includes a thorough treatment of semiconductor heterostructures.)

The FET is patterned using electron-beam lithography [83]. The channel is defined with a mesa etch which physically removes wafer material, taking the 2DEG with it. Electrical contact to the electron gas results from annealing AuNiGe pads that are deposited on the wafer for the source and drain terminals. The amount of current flowing through the channel is controlled by voltages applied to the gate electrodes, which are deposited on the surface by evaporating 200 Å of chromium followed by 1500 Å of gold. The FET features a dual-gate configuration, with each gate 2 μm long by 100 μm wide. Figure 3.11 shows a micrograph of the device. Theses of students from the Westervelt group contain clear accounts of the fabrication process used for their semiconductor devices (for example, see reference [84]).

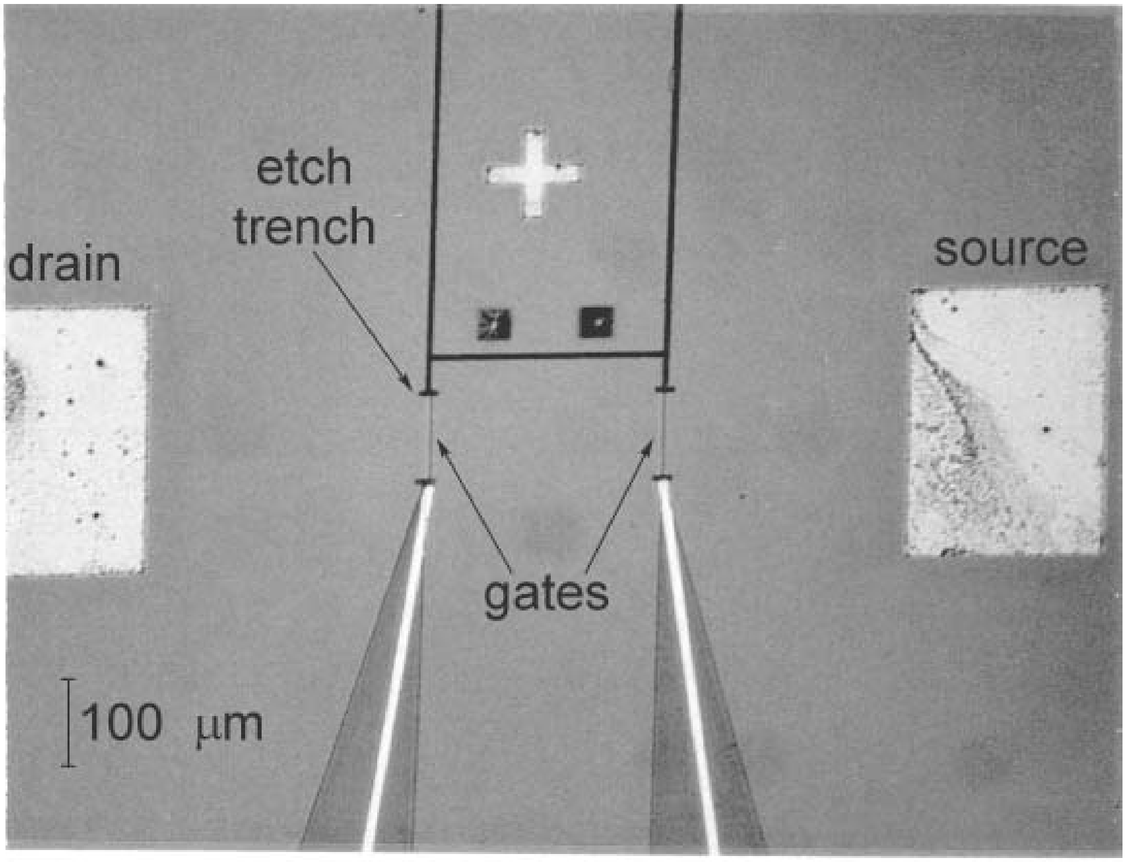

Figure 3.11: Optical micrograph of HFET. Courtesy of R. G. Beck.

The electrostatically sensitive and physically delicate wafer needs to be integrated into the standard design of our tuned amplifiers. The contacts on the wafer are wirebonded [85] with 0.001 inch gold wire to copper leads etched onto a 0.5 inch by 0.5 inch circuit board to which the wafer is cemented [86].[6] A bare 28 AWG wire is "twist tied" after going through a small hole in one of the copper leads, with the "twist" then soldered to the copper pad and acting as a leg for the FET. This

[6]If the contacts on the semiconductor become difficult to wirebond, the wafer can be dipped into a solution of 1 part ammonium hydroxide to 5 parts distilled water for 30–60 secs. The wafer should then be dried with nitrogen gas without rinsing in water.

design provides mechanical stability for the wire legs when soldering the transistor into the tuned amplifier which is quasi-permanently mounted to the cryostat. The FET is oriented so that the 2DEG is parallel to the magnetic field. A grounding or "make-before-break" switch permanently wired at the room temperature electrical feedthroughs for the FET bias leads allows cables to be connected and removed without the hazards of small sparks that can be so generated. Despite the proximity of the 2DEG to the surface, which makes the device particularly vulnerable to electrostatic discharge, the transistor is quite robust; the same FET has been in use for almost 3 years.

3.4.2 Characterization

Because of the low sheet density and high electron mobility of the 2DEG, the FET operates in the saturation region at low drain current and drain-source voltage. The drain characteristics in Fig. 3.12 show that a drain-source bias of 0.2 volts is enough to produce saturation. At 20 μA, the small-signal drain-source resistance is 450 kΩ. The transfer characteristic is shown in Fig. 3.13, along with its derivative which gives the transconductance. The transconductance is seen to plateau at 3 mS; for the data in this thesis, we typically used $V_{DS} = 0.2$ V and $I_D = 20 - 25$ μA, giving $g_m = 2 - 2.5$ mS. The respectable transconductance is primarily due to the proximity of the 2DEG to the surface.

In addition to the properties mentioned above, the light doping of the device is also responsible for the fact that this FET is not suitable for room-temperature operation. At 300 K, thermally liberated carriers leave ions[7] which scatter the electrons from the donors, seriously degrading the FET's performance. A transconductance

[7]Unlike the donor ions, which are physically isolated from the channel, these ions can be within the semiconductor that contains the 2DEG and thus increase scattering.

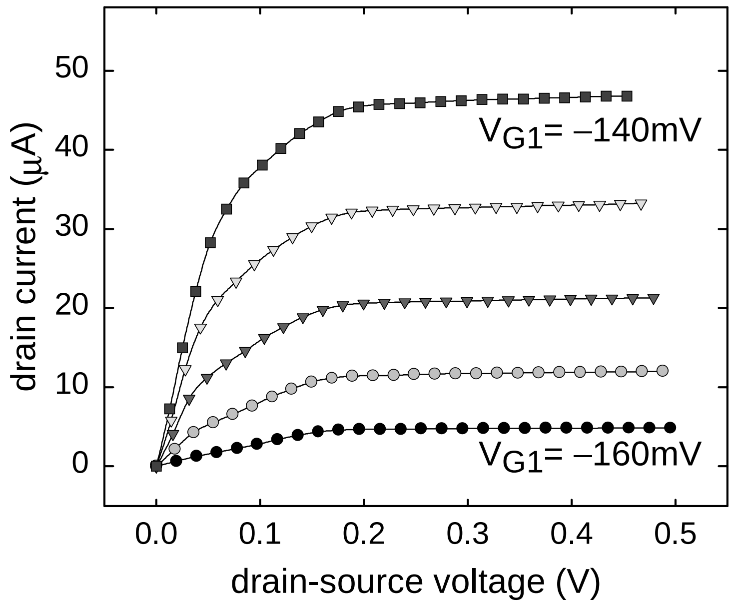

Figure 3.12: $I_D - V_{DS}$ curves at 4.2 K, showing low $V_{DS,sat}$. Gate 2 is grounded and gate 1 ranges from -160 mV to -140 mV in 5 mV increments.

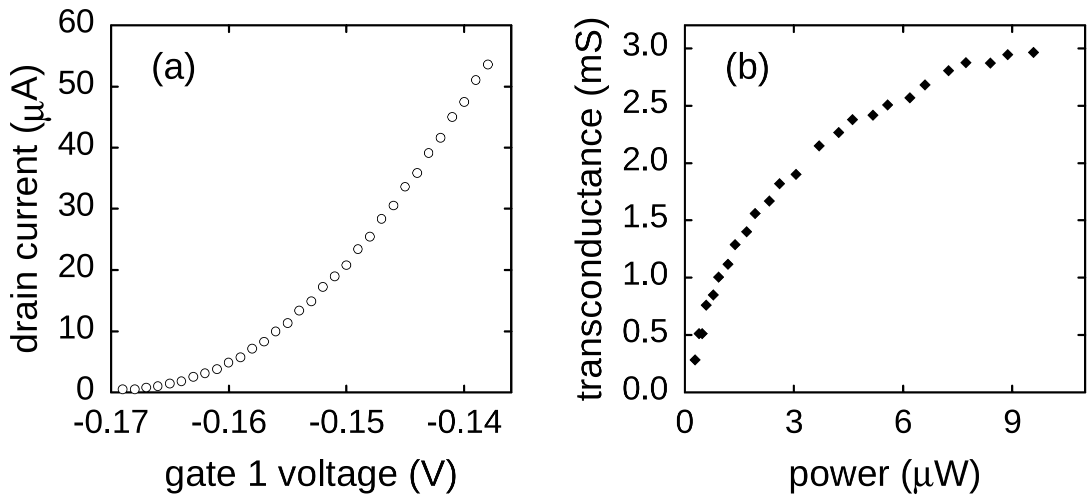

Figure 3.13: (a) $I_D - V_{G_1S}$ curve and (b) transconductance curve at 4.2 K. Gate 2 is grounded and $V_{DS} = 0.2$ V.

of only 0.1–0.5 mS is achieved, and the bias parameters are very different from those for 4.2 K (see Fig. 3.14 and Table 3.3). At 77 K, the transconductance improves

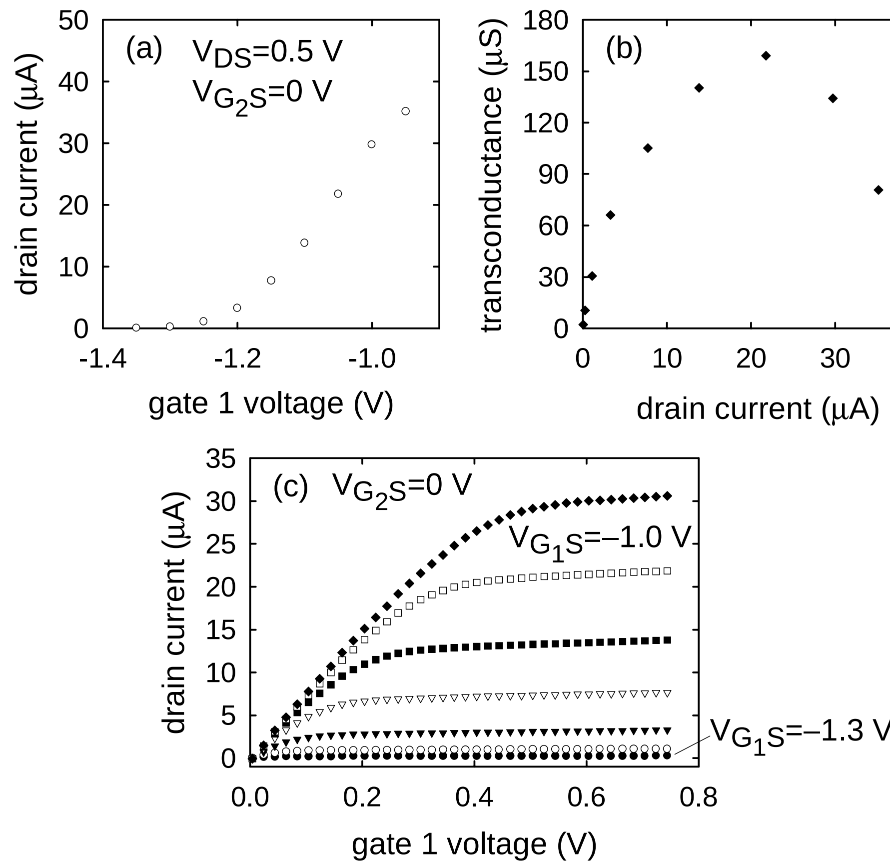

Figure 3.14: Characterization of HFET at room temperature. (a) Transfer characteristic at $V_{DS} = 0.5$ V and $V_{G_2S} = 0$ V. (b) Corresponding transconductance. (c) Family of $I_D - V_{DS}$ curves, with V_{G_1S} stepped in 50 mV increments.

to about 2 mS, and at 4.2 K the device performs optimally. Table 3.3 lists the approximate operating parameters of the FET at these different temperatures.

After cooling to 4 K, the channel typically needs to be filled with charge carriers by optically exciting electrons from the donors. This can be done with diffuse light from a cryogenic LED powered with several milliwatts. (This depletion of charge carriers by "electrostatic shock" is observed by us on every cool down, but is seen less frequently in other systems.) If extra carriers are liberated, several minutes may be required for equilibrium to be established. Afterward, however, the device is very stable — we witnessed no need for further optical activation for more than $5\frac{1}{2}$ months (at which time the particular experimental run ended).

temp. (K)	$\boldsymbol{V_{DS,sat}}$ **(V) for 20 μA**	$\boldsymbol{V_P}$ **(V)**
300	> 0.3	-1.3
77	~ 0.2	-0.170
4.2	≤ 0.2	-0.165

Table 3.3: HFET operating parameters at different temperatures.

The gain provided by the FET coupled with the low-noise properties enables a single-electron resonance to be resolved at 80 mK with signal-to-noise comparable to previous 4 K experiments. Figure 3.15 shows the in-phase and quadrature response of a single electron to an axial drive with the HFET dissipating 4.5 μW.

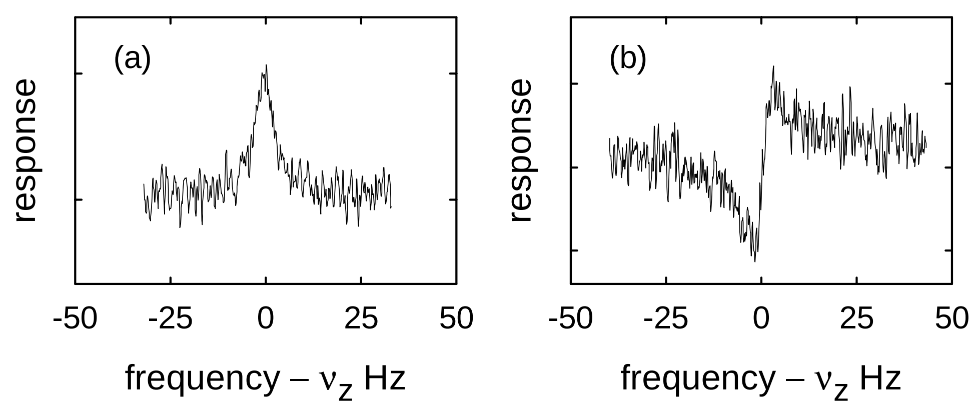

Figure 3.15: Driven single-electron resonances observed with the HFET dissipating 4.5 μW. (a) Electron's response in-phase with the drive. (b) Quadrature response.

3.4.3 Additional Considerations

This HFET is a device with very high charge sensitivity — an "ultrasensitive electrometer". The low-frequency transistor of D. J. Mar *et al.* demonstrated a charge sensitivity of 10^{-2} e/$\sqrt{\text{Hz}}$ and a charge resolution of 0.4 e [78]. A SQUID (superconducting quantum interference device) is a low-temperature detection device with very high sensitivity to magnetic fields — an "ultrasensitive magnetometer". Radio-frequency SQUIDs are currently used in one 4 K ion mass-spectrometry experiment to detect the ion's induced current at 160 kHz [87]. While a SQUID dissipates very little power, it is generally difficult to use, requiring somewhat complicated external electronics to operate, and the complete system is expensive. On the other hand, our cryogenic FET requires only a conventional power supply for operation.

Future versions of our HFET could feature some improvements. If the device is fabricated in a way to allow better heatsinking of the substrate, the axial temperature of our electron might be lower while the FET is operating. This could involve mounting the substrate on sapphire, *i.e.* replacing the circuit board (made out of G-10) "chip carrier" with a sapphire chip. In addition, the source resistance (from the imperfect contact to the 2DEG) and the gate resistance (from the small size of the electrode) could be reduced somewhat, reducing the thermal noise they generate. This noise is the dominant contribution when operating above the $1/f$ corner in saturation.

3.5 FET Comparison

At powers of several microwatts, the performance of the Harvard HFET is superior to that of the Mitsubishi MGF-1100. This section contains comparisons between the two devices for the relevant parameters for these experiments — low powers and radio frequencies (near 60 MHz).

3.5.1 DC Properties

The standard DC characterization of an FET includes the family of $I_D - V_{DS}$ curves and the transfer characteristic, or $I_D - V_{G_1S}$ curve, whose slope gives the transconductance. Figure 3.16 shows the drain characteristics for identical regions of current and voltage for the two transistors (this just consolidates the same graphs from the two previous sections). The HFET is in saturation at low V_{DS}, about 0.2 V, while the MESFET is strictly in the linear region. The lower gate bias for the HFET is a manifestation of the higher charge sensitivity of the device. The DC transconductance for each transistor is plotted versus power in Fig. 3.17. We have measured the transconductance versus frequency for the FETs and have seen that the DC values agree with the values at 60 MHz.

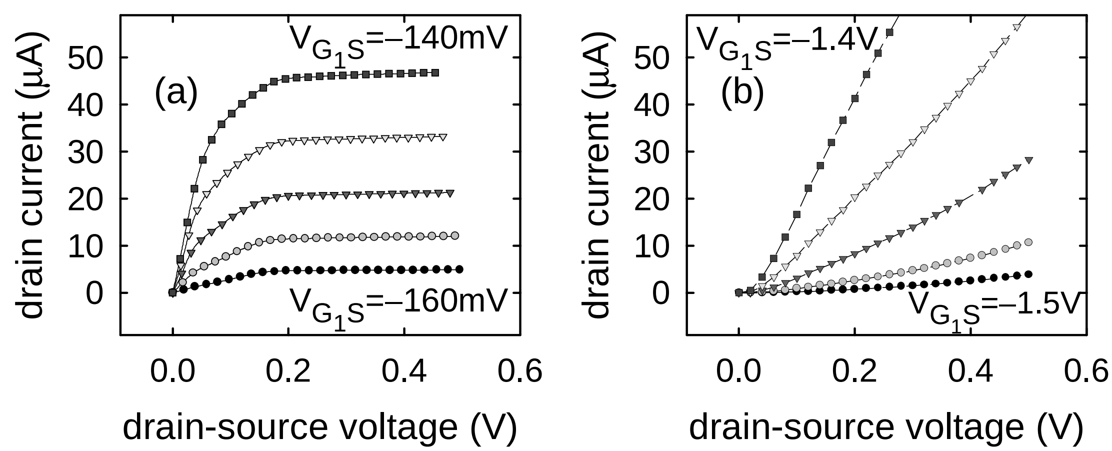

Figure 3.16: Drain characteristics at 4.2 K for the (a) HFET and the (b) MESFET.

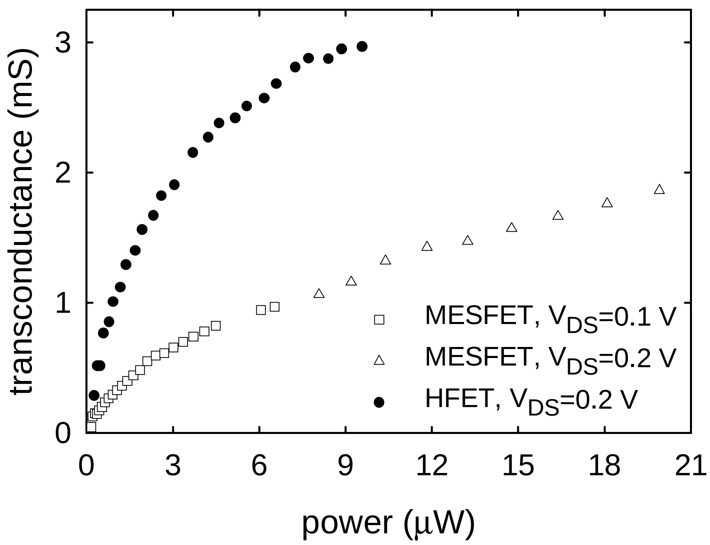

Figure 3.17: Comparison of the transconductances of the two FETs. The HFET curve is for $V_{DS} = 0.2$ V so that the device is in saturation. The MESFET curve is for two different values of V_{DS}, according to the optimization procedure described in Section 3.3.2.

3.5.2 AC Properties

Noise Resonance

The noise resonance of our tuned amplifier is a useful indicator of the achievable signal-to-noise for an electron signal. Figure 3.18 shows the noise power spectrum obtained with each FET in one of our amplifiers at 4 K. The transistors were biased with $V_{DS} = 0.5$ V and $I_D = 30$ μA. The signal-to-noise of the HFET resonance is about five times greater than the MESFET resonance. The Q values of the resonances are the same within the uncertainty of the comparison.

Signal from Cloud of 30 Electrons

A more stringent comparison than the noise-resonance test is to compare the signal-to-noise ratio of the driven amplitude of a small electron cloud obtained with each

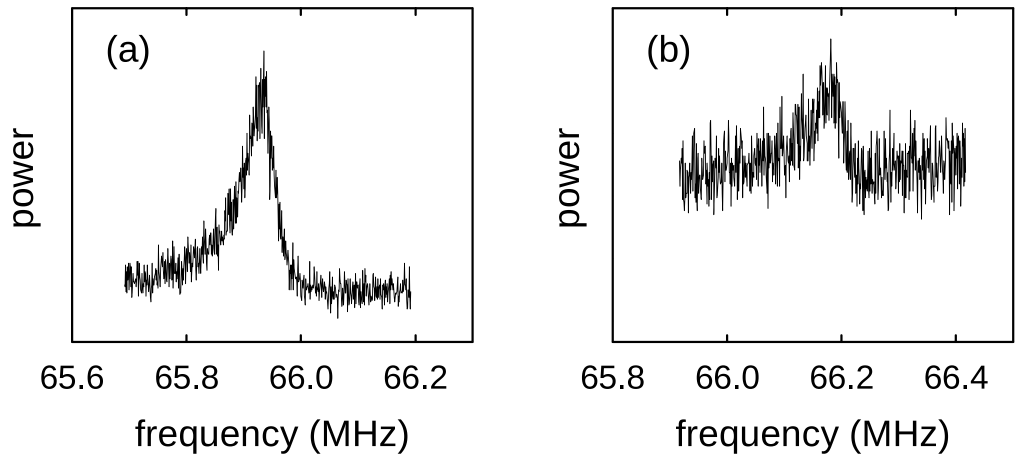

Figure 3.18: Comparison of a tuned-circuit noise resonance obtained with each transistor, (a) HFET and (b) MESFET.

FET. Figure 3.19(a) shows the signal obtained from a 30-electron cloud with each FET at 2 μW, and emphasizes the superiority of the HFET at that power. Figure 3.19(b) displays a semi-log plot of signal-to-noise ratio for the driven axial amplitude versus transistor power dissipation. The same electron cloud was used for each curve. The y-axis is obtained by dividing the height of the Lorentzian response by the standard deviation of the residuals on the baseline. The FETs were (necessarily) used with different tuned amplifiers, so the Q values of the tuned circuits were taken into account. (The above noise-resonance comparison demonstrates that the two FETs do not load the tuned circuit differently at 60 MHz.)

The points on the HFET curve were obtained by applying a drain-source bias of 0.2 V and stepping the drain current in 5 μA increments. In order to bias the MESFET, the optimization procedure outlined in Section 3.3.2 was implemented.

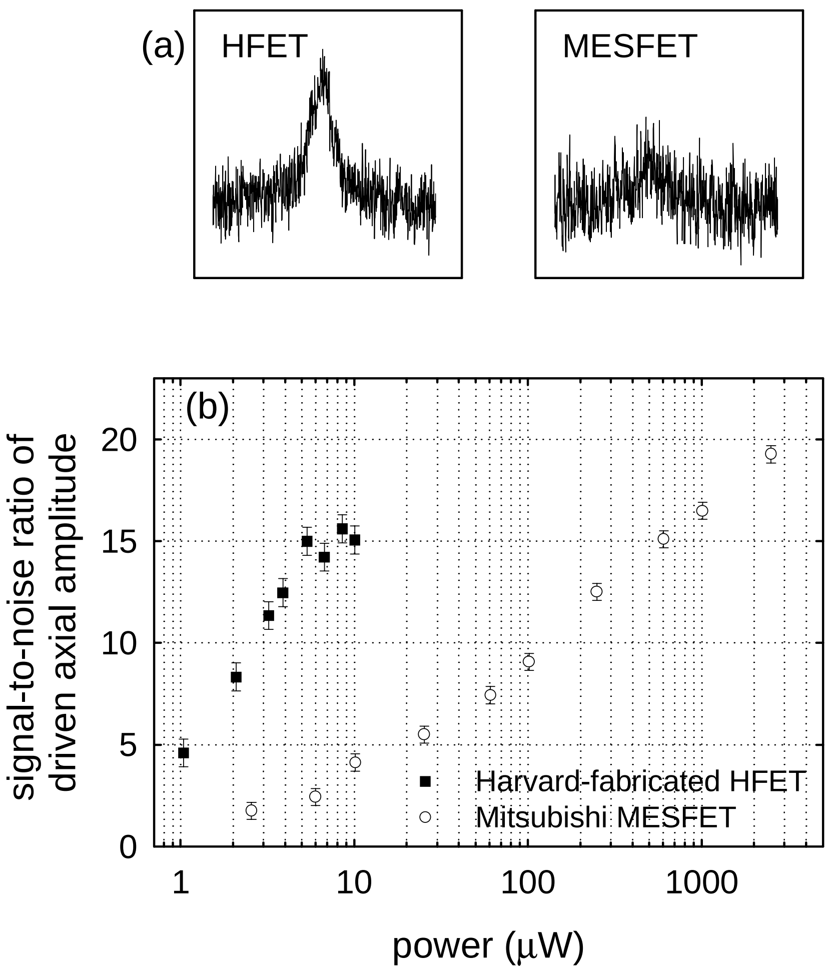

Figure 3.19: An FET comparison using the most relevant indicator, the driven response of a small cloud of electrons. (a) Resonances obtained with each FET dissipating 2 μW. (b) Semi-log plot of signal-to-noise ratio versus power.

3.6 Conclusions and Future Improvements

Throttling the MGF-1100 MESFET is a feasible solution for particular experiments in which either an elevated base temperature is acceptable or clouds of particles are being used. The sacrifice in temperature depends on the number of particles being detected. Figure 3.7 shows that monitoring a cloud of 30 electrons may require a power dissipation of 70 μW, which will heat the trap to several hundred millikelvin. In Chapter 2, we saw that for a cloud of about 300 electrons we could starve the MESFET to 15 μW (Fig. 2.2), which kept the trap temperature as low as 100 mK. For detection of a single electron below 100 mK, the HFET is necessary.

Once amplifier designs and FETs are no longer being developed and tested, electron experiments in this system can likely be carried out with just one amplifier. In this case, a bigger resonator can be used to improve the Q value. Additionally, implementing the transformer coupling and the HFET together should produce a substantially lower trap temperature than the 80 mK we demonstrated with the HFET in the directly coupled amplifier.

Chapter 4

Quantum Jumps Between Fock States

We have directly observed quantum jumps between energy levels of a harmonic oscillator. Microwave photons stimulate transitions between the Fock states of our electron cyclotron oscillator which are revealed in real time with high signal-to-noise ratio. Figure 4.1 illustrates a transition from the ground state to the first excited state and back, along with the signal observed. An extremely low temperature and a cylindrical Penning trap cavity allow the observation of these transitions. Quantum jumps induced by blackbody radiation from the trap walls enable us to measure the temperature of the electron's cyclotron motion and of the radiation field. These excitations of the cyclotron oscillator become less frequent as the trap temperature is lowered and ultimately cease by the time a base temperature of less than 100 mK is reached. At this temperature, a pure harmonic-oscillator ground state is realized and available for experiments, including quantum-jump spectroscopy for precision measurements (Chapter 5).

A charged particle in a magnetic field is a simple harmonic oscillator. Neglecting

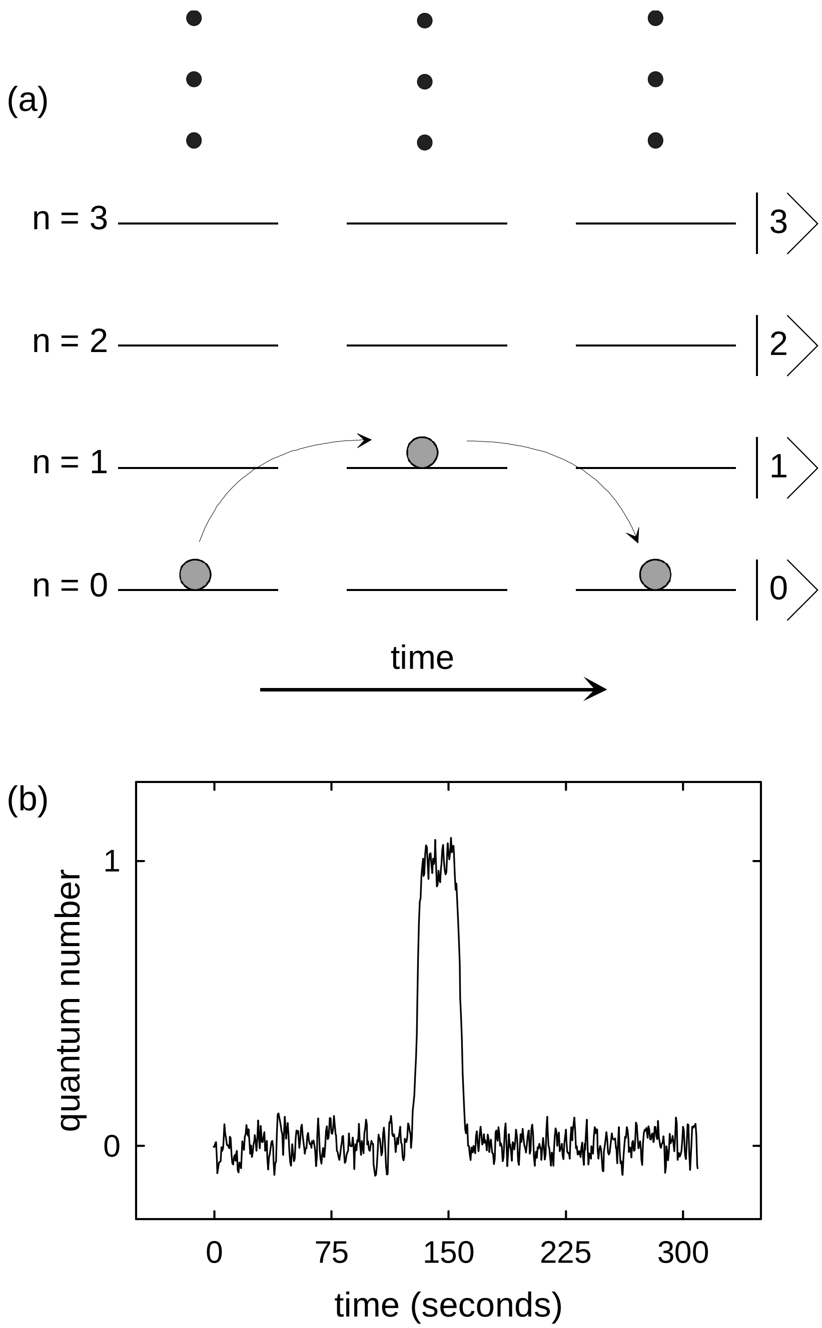

Figure 4.1: (a) Equally spaced energy eigenstates form an infinite ladder of Landau levels. The sequence of transitions from $|0\rangle \rightarrow |1\rangle \rightarrow |0\rangle$ is illustrated. (b) Observed signal for the event shown in (a) when the oscillator is cooled to 80 mK and excited with an external drive.

the anharmonicity introduced by special relativity [88], the Hamiltonian for the cyclotron motion is

$$H_c = (a^\dagger a + \frac{1}{2})\hbar\omega_c. \tag{4.1}$$

The energy eigenstates for this system are equally spaced states separated by 147 GHz in frequency for our 5.2 T field. For an electron in a magnetic field, these states are often called Landau levels, but in general such eigenstates of a harmonic oscillator are known as number states or Fock states.

Most realizations of a quantum-mechanical harmonic oscillator are in the form of coherent states, such as the radiation field of a laser, or thermal states, such as the radiation field in an undriven, low-Q cavity. The generation of non-classical harmonic-oscillator states, including Fock states, is important to emerging fields which require engineering the quantum state of a system (*e.g.* quantum communication [2]). Our system is one of the first to prepare Fock states of $n > 1$ [12], and is the first to observe them directly and non-destructively. Figure 4.2 shows the signal from our electron being excited to the $n = 1$ and $n = 4$ levels by thermal radiation, and to the $n = 1$ and $n = 2$ levels by an external microwave drive. An event in which the electron makes successive jumps from the ground state, to $n = 2$ and back, is displayed in Fig. 4.3.

Direct monitoring of the decay of an atom reveals “quantum jumps”. Quantum jumps were observed in ion-trap experiments which monitored abrupt transitions of a single atom between its ground state and a weakly coupled state, and were intended to be a way of amplifying the spectroscopic signal from that forbidden transition [89, 90, 91]. A dipole transition between the ground state and a third atomic level was optically cycled on the order of 10^8 times per second, resulting in a large continuous fluorescence signal. This fluorescence disappeared when the

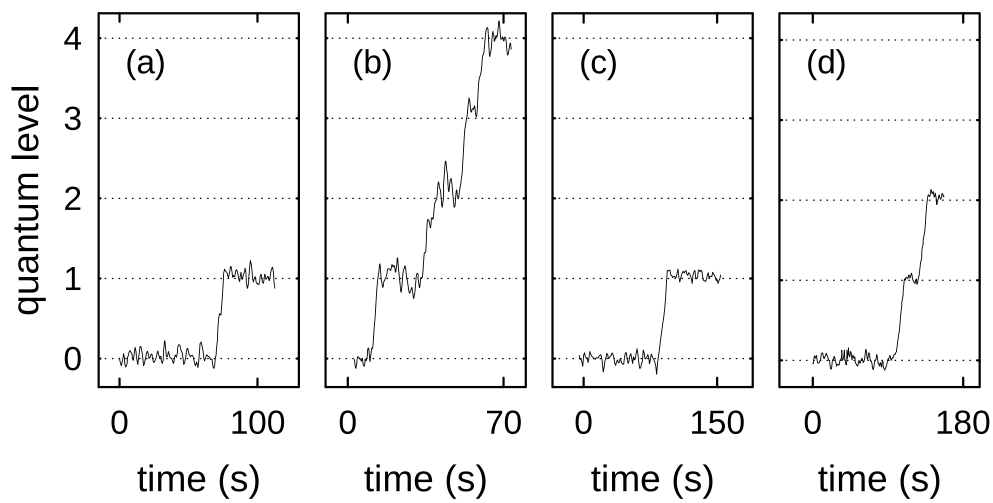

Figure 4.2: Observation of quantum jumps to low-n Fock states due to absorption of (a)–(b) thermal photons and (c)–(d) photons from an external drive.

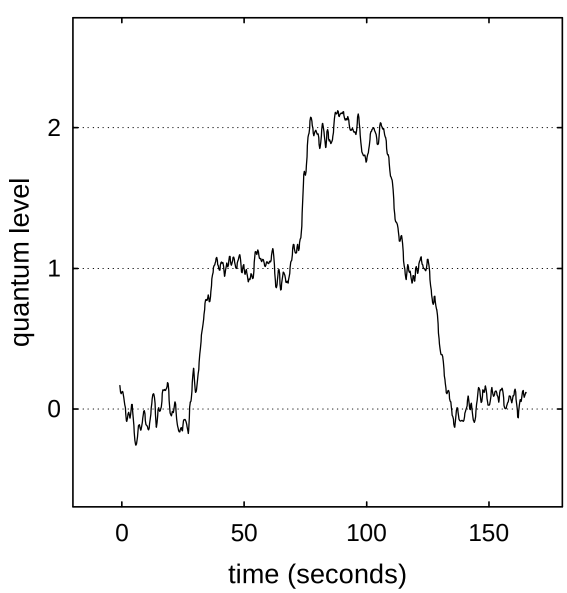

Figure 4.3: Signal observed when the cyclotron oscillator makes transitions from $|0\rangle \rightarrow |1\rangle \rightarrow |2\rangle \rightarrow |1\rangle \rightarrow |0\rangle$.

atom made a transition to the metastable state, taking it out of resonance with the laser light. The disruption in the bright fluorescence induced by a single-photon excitation to the metastable state provided the signal for the quantum jumps and the gain mechanism for the intended spectroscopy (Fig. 4.4).

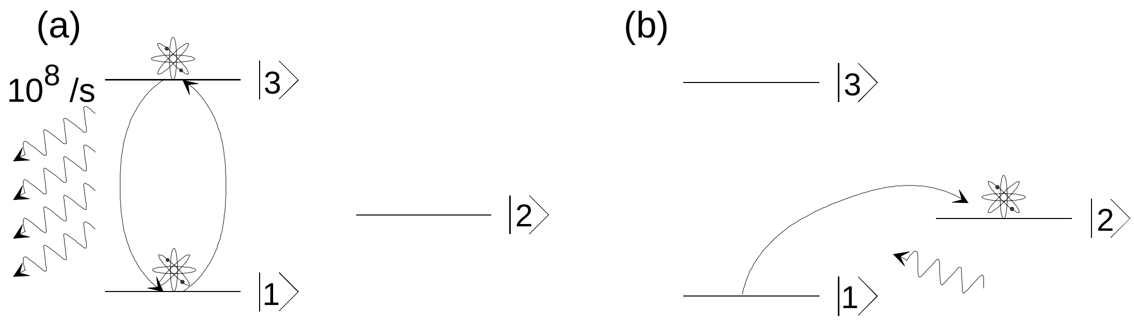

Figure 4.4: Process involved in quantum jumps of a trapped ion. (a) A strong transition ($|1\rangle \leftrightarrow |3\rangle$) is made to fluoresce about 10^8 photons per second. (b) When the ion makes a quantum jump from the ground state to the weakly coupled state $|2\rangle$, the bright fluorescence from the strong transition is interrupted, providing an easily observed signal for the single-photon excitation. See references [89, 90, 91].

4.1 Magnetic-Bottle Coupling

We employ a magnetic-field gradient to couple the electron's cyclotron and spin levels to its axial motion, which is detected using RF techniques (Chapter 3). This magnetic-field perturbation, which is similar to but much larger than the one used to detect spin flips [31], is produced by nickel rings incorporated into the trap assembly. The strong field of the superconducting solenoid saturates the magnetization of the nickel at $M(\mathrm{Ni}) = 0.485$ J/(T·m^3). Figures 4.5 and 4.6 show the dimensions of the nickel rings and their location in the trap.

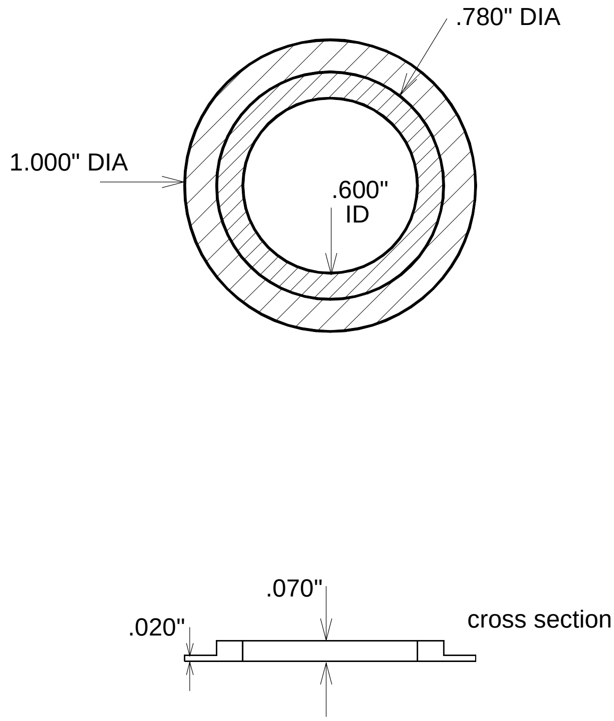

Figure 4.5: Mechanical drawing for one of the nickel electrodes used to produce the bottle field.

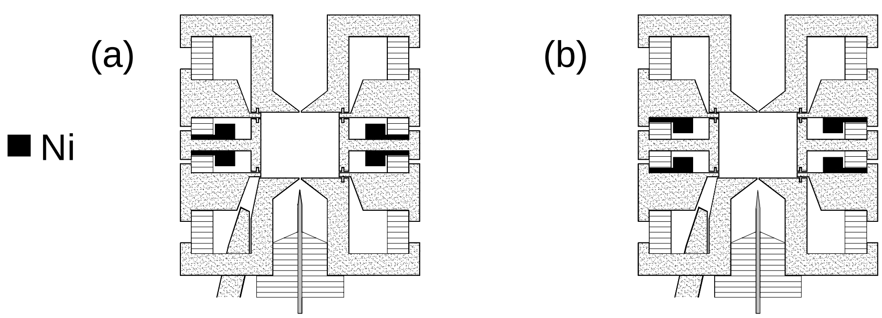

Figure 4.6: Trap-assembly drawing (cross section) showing (a) placement of nickel rings in the current setup and (b) configuration that could be used to give a smaller B_2 for the same nickel electrodes.

4.1.1 Bottle Field

The multipole expansion of the field perturbation due to the nickel material is given by [48]

$$\boldsymbol{\Delta B}(\boldsymbol{r}) = \sum_{\substack{l=0 \\ \text{even}}}^{\infty} B_l r^l \left[P_l(\cos\theta)\hat{z} - (l+1)^{-1} P_l^1(\cos\theta)\hat{\rho}\right] \tag{4.2}$$

with expansion coefficients

$$B_l = (l+1)(l+2)2\pi \int \rho' d\rho' dz' M(\rho', z')(r')^{-l-3} P_{l+2}(cos\theta'). \tag{4.3}$$

The sum is over just even l because the nickel electrodes are symmetric under $z \to -z$, and the $P_l^1(\cos\theta)$ are associated Legendre polynomials. The $l = 0$ term, $B_0\hat{\boldsymbol{z}}$, adds a 0.7% contribution to the uniform trapping field. The next term couples the orthogonal motions of the electron and is often referred to as the "magnetic bottle" [48]. The nickel rings in our trap were designed to contribute a hefty B_2 of 1470 T/m^2, about ten times larger than the magnetic bottle used earlier to detect spin flips [31]. With the same nickel rings, B_2 can be decreased by placing them in the compensation electrodes (Fig. 4.6(b)) rather than in the ring (Fig. 4.6(a)).[1]

The values of B_0 and B_2 have been measured and compared with the calculated values (Table 4.1). B_0 is measured from the cyclotron frequency $\omega_c = eB/m$ of an electron cloud at the trap center with and without the nickel electrodes in the trap. Our B_0 was determined using two frequencies measured about $1\frac{1}{3}$ years apart, during which time the trap was rebuilt in order to include the nickel rings. The difference in the two cyclotron frequencies is attributed to B_0.

Measuring B_2 requires measuring ω_c as a function of z, the axial position. Dis-

[1] This is not quite a practical option for the trap presently in use. It utilizes compensation electrodes that are split into two pieces, which would be shorted together by the nickel. This would be a viable option for a trap with solid compensation electrodes.

placing a cloud of electrons axially is accomplished by applying an antisymmetric DC potential to the trap. As the cloud is displaced, shifts in both ω_c (due to the bottle field) and ω_z (due to changes in the shape of the electrostatic well) occur. The axial frequency shift is used to calibrate the size of the displacement versus the applied voltage, V_A. The details of the displacement procedure and calibration are discussed in Appendix D. Figure 4.7 shows the measured cyclotron frequency versus axial position, with a quadratic fit giving $B_2 = 1540\ \mathrm{T/m^2}$. The calculated and measured values for B_2 are summarized in Table 4.1.

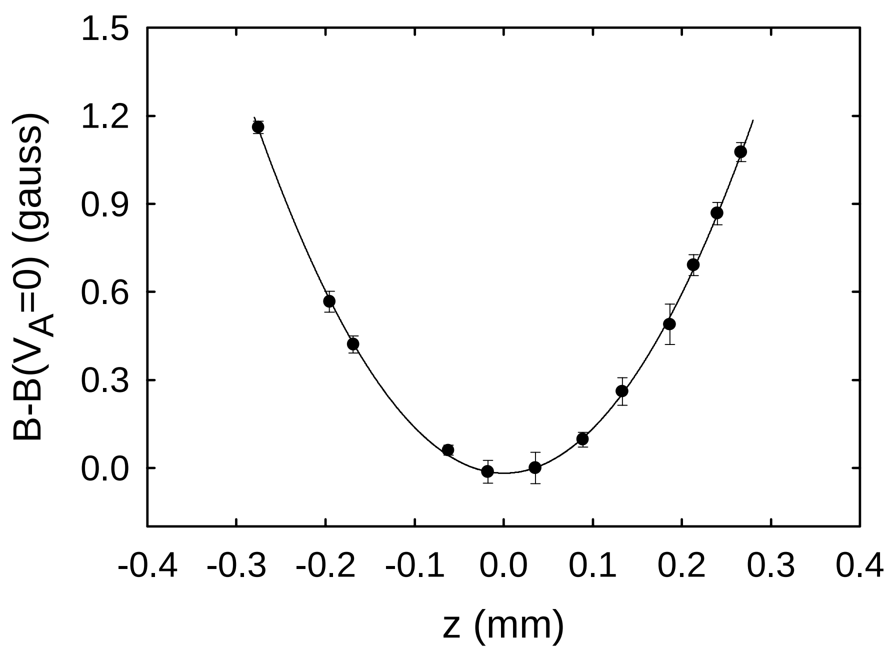

Figure 4.7: Change in magnetic field versus axial displacement. The absence of two points on the left-hand side of the curve is apparently due to nodes in the standing wave pattern.

	$\boldsymbol{B_0}$	$\boldsymbol{B_2}$
calculated	$-346(10)$ G	$1468(39)$ G/cm^2
measured	$-349(0)$ G	$1539(12)$ G/cm^2

Table 4.1: Calculated and measured values of the leading expansion coefficients for the magnetic-field perturbation.

4.1.2 Axial-Frequency Shift — Theory

A trapped electron has a magnetic moment in the $\hat{z}$ direction, $\boldsymbol{\mu}= \mu\hat{z}$, with contributions from its spin s and orbital angular momentum L,

$$\mu_s = g\frac{e}{2m}s \tag{4.4}$$

and

$$\mu_L = \frac{e}{2m}L. \tag{4.5}$$

The potential energy of a magnetic dipole moment in an external magnetic field is $-\boldsymbol{\mu} \cdot \boldsymbol{B}$. The electron's energy in the magnetic-bottle field can be written as

$$E = -\boldsymbol{\mu} \cdot \boldsymbol{\Delta B} = -\mu B_z = -\mu \left[B_0 + B_2 \left(z^2 - \frac{\rho^2}{2}\right)\right], \tag{4.6}$$

to second order in the field expansion. Since we cool the electron essentially to the z-axis, we take $\rho = 0$. The first term above does not have any z-dependence and thus is not involved in the coupling of the orthogonal motions of the electron. The second term, $-\mu B_2 z^2$, describes the bottle coupling because it exhibits dependence on μ (which depends on the energy of the spin and cyclotron systems) and on z, the axial position. This interaction comes into the equation of motion for the axial harmonic oscillator,

$$\ddot{z} + \gamma_z \dot{z} + \left(\omega_{z0}^2 - 2B_2 \frac{\mu}{m}\right) z = 0, \tag{4.7}$$

where

$$\omega_{z0}^2 = \frac{eV_0}{md^2}\left(1 + C_2\right). \tag{4.8}$$

The spring constant k_z acquires a dependence on μ, giving a modified axial frequency of

$$\begin{aligned} \omega_z^2 &= \omega_{z0}^2 - \frac{2B_2\mu}{m} \\ &= \omega_{z0}^2 + \frac{2B_2}{m}\left(2n_c + 1 + gn_s\right)\mu_B, \end{aligned} \tag{4.9}$$

using the quantum mechanical expressions for the magnetic moments,

$$\mu_L = -(2n_c + 1)\mu_B \quad \text{and} \quad \mu_s = -gn_s\mu_B \quad (n_s = \pm 1/2). \tag{4.10}$$

We have neglected the small contribution to μ_L from the magnetron motion.

Since the modification to the axial frequency is small compared to ω_{z0}, we can expand the above expression,

$$\omega_z = \omega_{z0}\left[1 + \frac{1}{m\omega_{z0}^2} B_2\left(2n_c + 1 + gn_s\right)\mu_B\right]. \tag{4.11}$$

From this we can see that the spin and cyclotron states of the system change the axial frequency by

$$\Delta\omega_z = \frac{B_2\mu_B}{m\omega_{z0}}\left(2n_c + 1 + gn_s\right). \tag{4.12}$$

For a change in energy of either $\Delta n_c = 1$ or $\Delta n_s = 1$, the axial frequency shifts by $2\pi(12.2)$ Hz.

4.1.3 Axial-Frequency Shift — Experiment

A signal proportional to shifts in the axial frequency can be obtained by locking the electron's oscillation to a frequency reference in the laboratory. The electron's motion is driven with the harmonic signal from a high-precision frequency synthesizer. The response of the electron is amplified by a cooled preamp and by room-temperature amplifiers and is then sent to a lock-in amplifier whose reference is the same synthesizer that drives the electron. (The detection scheme is explained in more detail in Section 2.2.) A lock-in amplifier mixes the input it receives with two orthogonal signals, enabling it to provide an output that is proportional to the amplitude of the input with a fixed but arbitrary phase relative to its reference. A driven, damped harmonic oscillator exhibits a Lorentzian resonance for its response in phase with the drive and a dispersive resonance for its quadrature response (recall Fig. 2.6).

The dispersion curve has a linear region that crosses zero on resonance and provides a useful signal for locking the electron's axial frequency. This curve shifts higher or lower in frequency with changes in ν_z, providing the locking circuit an error signal proportional to the frequency shift. The correction voltage generated by the lock loop is added to the trapping potential to maintain a constant axial frequency. This voltage, being proportional to the shift in axial frequency, also acts as the signal for transitions in the magnetic systems, as shown in Fig. 4.8. Once the electron frequency is locked, the correction voltage versus frequency shift can be calibrated by changing the local oscillator by a known amount and measuring the correction voltage applied. In this way, the smallest single-electron quantum jumps observed are determined to correspond to a frequency shift of 12.3(4) Hz, which agrees well with the 12.2 Hz from Eq. (4.12).

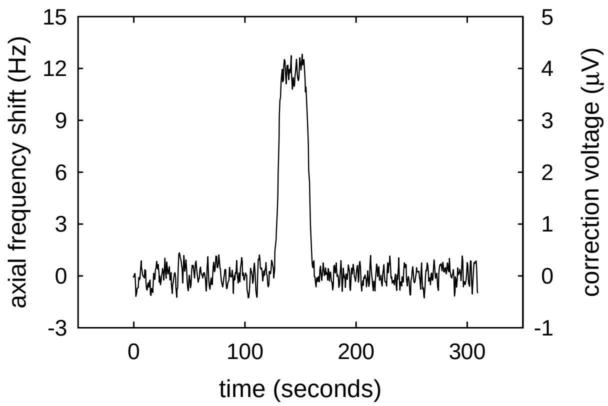

Figure 4.8: Quantum-jump signal observed at 80 mK when the electron's quadrature response is locked to a frequency reference.

The speed at which the locking circuit responds to a shift in axial frequency is maximized in order to detect the shortest-lived cyclotron excitations. One obstacle to achieving the fastest response is the size of the frequency shift. The change of 12.3 Hz is considerably larger than the available linear region of the dispersion curve (± 2.5 Hz). This results in a weak error signal (the amount by which the wing of the dispersion curve is positive, Fig. 4.9) until enough integration has occurred that the peak of the dispersion curve is reached. A smaller frequency shift (a 3 Hz shift is still easily resolvable) would cause the error signal applied to the lock loop to be large and on the linear part of the resonance.

4.1.4 Thermal Issues

Our experiment implements a magnetic bottle which is larger than those used in other electron traps. In addition to the advantageous coupling the bottle provides, it would also have a negative effect on our single-electron experiments if we were not able to work at such a low temperature. The presence of the bottle field means

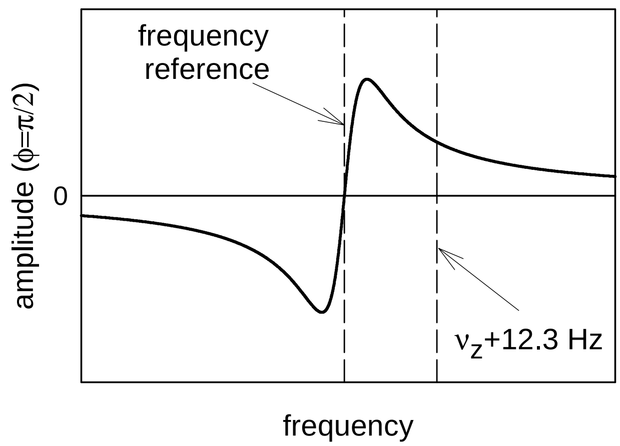

Figure 4.9: The size of the axial frequency shift does not optimize the response time of the lock loop.

that the total magnetic field — and thus ω_c and ω_s — depends on the electron's position in the trap. Thermal noise stochastically driving the axial oscillator causes random amplitude fluctuations which are seen by the electron as fluctuations in the magnetic field. For this reason, impressive efforts have been put forth in the past decade [88, 52, 92, 93] to reduce the size of this bottle field or eliminate it altogether.[2] Our dilution-refrigerator environment, with an operating temperature about 100 times lower than liquid-helium experiments, has enabled us to use a larger bottle to achieve exceptional sensitivity to cyclotron and spin transitions while still reducing the thermal broadening compared to the last g-factor measurement. These thermal issues are the focus of Section 5.1.

[2]In the latter case, the intrinsic coupling due to special relativity [88, 52] provides the axial-frequency shift needed to observe cyclotron transitions and spin flips.

4.1.5 Counting Electrons

Counting electrons has been done in the past using a variety of techniques (see, for example, reference [50]). Quantum jumps of the cyclotron oscillator provide a novel, straightforward method of counting up to three electrons.

Our RF detector measures the current induced by the axial oscillation of an electron cloud's center of mass. With 2 or 3 electrons in the trap, a single quantum-level transition of one of the electrons generates a 12.3 Hz shift which is averaged with the unshifted frequencies when the signal is measured. The quantum-jump signature for clouds of 2 and 3 electrons are shown in Fig. 4.10. (Quantum jumps with multiple ions were observed in reference [90].)

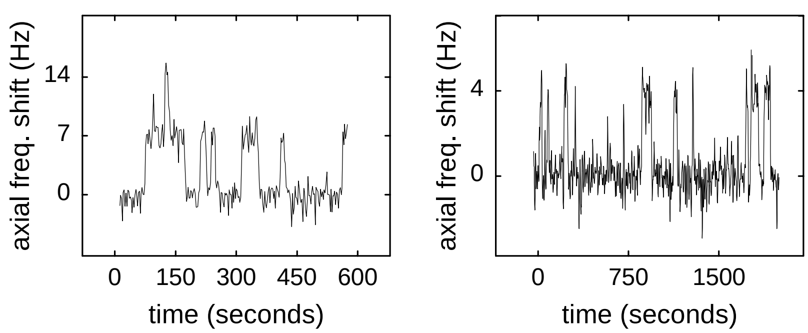

Figure 4.10: Quantum-jump signal obtained from clouds of 2 and 3 electrons. The size of the smallest quantum jump for 2 electrons is somewhat larger than expected according to the above discussion.

4.1.6 Future Considerations

The large size of our bottle was chosen to allow us to make progress quickly without issues arising from inadequate signal-to-noise for single-quantum transitions. Frequency shifts as small as 1 Hz can be resolved, and shifts of 3 Hz can be observed easily. Replacing this "extra large" magnetic bottle with one that still provides ample coupling (*e.g.* a 3 Hz shift per transition) would provide more of a buffer against the thermal systematic effects and decrease the response time of the lock-loop as discussed in the previous section.

4.2 Inhibited Spontaneous Emission

In order to measure the current from a single electron well enough to resolve the electron's cyclotron level, it is necessary to average for times on order of a second. The free-space lifetime of an electron cyclotron oscillator is

$$\tau_c = \gamma_c^{-1} = \left[\frac{1}{4\pi\epsilon_0}\left(\frac{4e^2\omega_c^2}{3mc^3}\right)\right]^{-1} = 94 \text{ ms} \tag{4.13}$$

for a 5.2 T field. With this lifetime, excited Fock states of the oscillator are difficult to observe. Past experiments have seen asymmetric noise spikes on a frequency-lock signal due to thermal excitations to $n > 0$. Since n is never negative, spikes were only measured in one direction [94, 69]. Observing quantum jumps between energy levels of the cyclotron oscillator requires lengthening the system's lifetime by inhibiting spontaneous emission.

4.2.1 History

E. Purcell first proposed that radio-frequency transition rates of an atom could be enhanced by coupling to a resonant circuit [95]. Alternatively, a cavity can be used to *suppress* the radiation rate of a system. As recently as 1983, D. Kleppner pointed out that inhibited spontaneous emission had yet to be observed experimentally [96]. Several years later, the first observation in a microwave cavity [47] was reported in which the modified vacuum inside a Penning trap was utilized to inhibit synchrotron radiation of an electron cyclotron oscillator. This reduction in the radiation rate resulted in an increase of the system's lifetime by a factor of five; later, a factor of ten increase was reported in a similar system [51]. A Penning-trap cavity has since been used to demonstrate an enhanced spontaneous emission rate [52], similar to the original experiments that pioneered the field of cavity QED [97].

4.2.2 Cavity Modes of a Cylindrical Penning Trap

The original Penning traps, including those used in the examples just discussed, featured electrodes with hyperbolic surfaces in order to achieve a large harmonic volume in the trap. The largest uncertainty in the measurement of the electron's g factor is the estimate of the frequency shift caused by the cavity-modified radiation field [31]. A hyperbolic trap's cavity modes, and therefore the trap's effect on an electron's oscillation frequency, are difficult to characterize. In order to gain a handle on the electron-cavity interaction, a trap with electrodes that form a cylindrical cavity with a well understood mode spectrum was designed [49] and built [40].

The cavity modes for our cylindrical trap can be calculated analytically by treating it as an ideal cylindrical cavity. The modes have resonant frequencies given by [98]

$$2\pi\nu_{mnp} = c\sqrt{\left(\frac{\chi_{mn}}{\rho_0}\right)^2 + \left(\frac{p\pi}{2z_0}\right)^2}. \tag{4.14}$$

χ_{mn} is the nth zero of the Bessel function $J_m(x)$ for TM_{mnp} modes, which have an index $p = 0, 1, 2, \ldots$ For TE_{mnp} modes, χ_{mn} is the nth zero of $J'_m(x)$, and the index p can take on the values $1, 2, 3, \ldots$ [50]. The mode structure can be experimentally observed using the signal from a cloud of electrons driven parametrically. The parametric response is very sensitive to the damping of the cyclotron motion of the cloud and thus to the cloud's detuning from the trap's resonant modes; details are discussed in reference [40].

While the mode structure for the particular trap used in this experiment has not been acquired, the mode spectrum from reference [50] is for an identical trap. The center frequencies of the TE_{0np} modes of that trap were used to determine its cavity dimensions, giving $z_0 = 0.3838(6)$ cm and $\rho_0 = 0.4559(6)$ cm. The mechanical drawing for our trap specified $z_0 = 0.3842(3)$ and $\rho_0 = 0.4564(3)$ — we therefore have confidence in claiming a similar mode spectrum for this experiment.

A 10 GHz section of the spectrum of cavity modes is shown in Fig. 4.11. We have detuned the cyclotron motion from the modes of the trap. The weak coupling

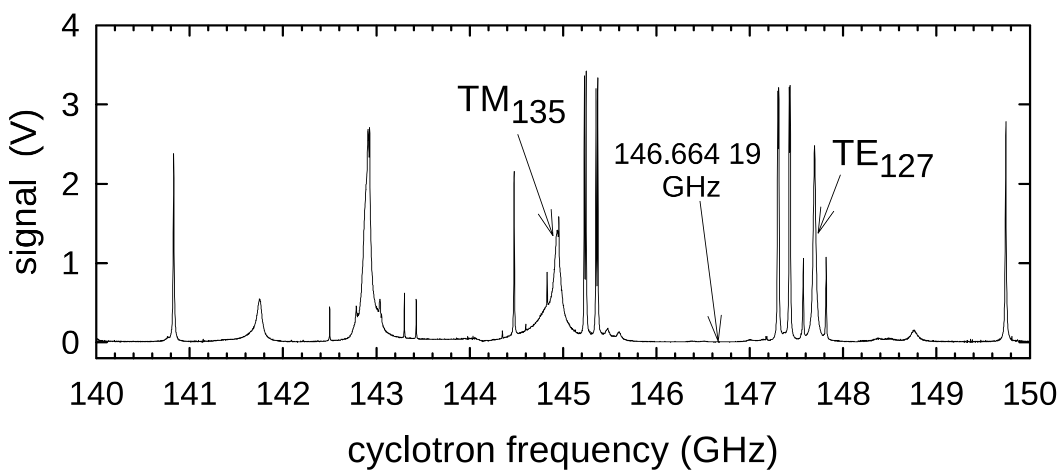

Figure 4.11: A 10 GHz section of the cavity-mode spectrum of a cylindrical Penning trap. The amplitude of the radiation field at our cyclotron frequency is denoted. This figure is courtesy of J. N. Tan [40].

to the radiation field at 146.7 GHz results in inhibited spontaneous emission of our cyclotron oscillator by more than two orders of magnitude. The resultant lifetime, measured to be 13 sec at 1.6 K (Section 4.3.2), enables us to average sufficiently to observe excited Fock states of the oscillator. This dramatic increase in the lifetime is possible because of the well-separated, high-Q modes that exist in a cylindrical trap.

The nearest modes that couple to an electron at the trap center are the TM_{135} and TE_{127} modes,[3] which have Q values and center frequencies listed in Table 4.2. These values, along with the known field geometries, can be used to calculate the frequency shift (see Section 5.3) and damping rate of a centered electron. For an electron

	$\mathbf{TM}_{135}$	$\mathbf{TE}_{127}$
ν (GHz)	144.8	147.7
Q	1900	16,500

Table 4.2: Center frequencies and Q values of the modes nearest to ν_c [50].

coupled to mode M, the frequency shift and damping rate can be written [99]

$$\Delta\omega - i\frac{\gamma}{2} = \frac{\omega\lambda_M^2}{\omega^2 + i\omega\Gamma_M - \omega_M^2} \tag{4.15}$$

where λ_M is the coupling strength, which has been calculated for all of the modes of a cylindrical trap cavity in reference [99]. The real and imaginary parts of the right-hand side of this expression determine the frequency shift and damping rate introduced by the mode. Figure 4.12 shows the calculated lifetime for cyclotron frequencies between the TM_{135} and TE_{127} modes. The magnitude of these lifetimes is consistent with the value we measure.

[3]The cavity modes are often observed as frequency doublets or with sidebands due to the driven motion of the electron cloud through the standing-wave radiation field. The two doublets in between these modes in Fig. 4.11 have nodes at $z = 0$ and thus do not couple to an electron at the center of the trap.

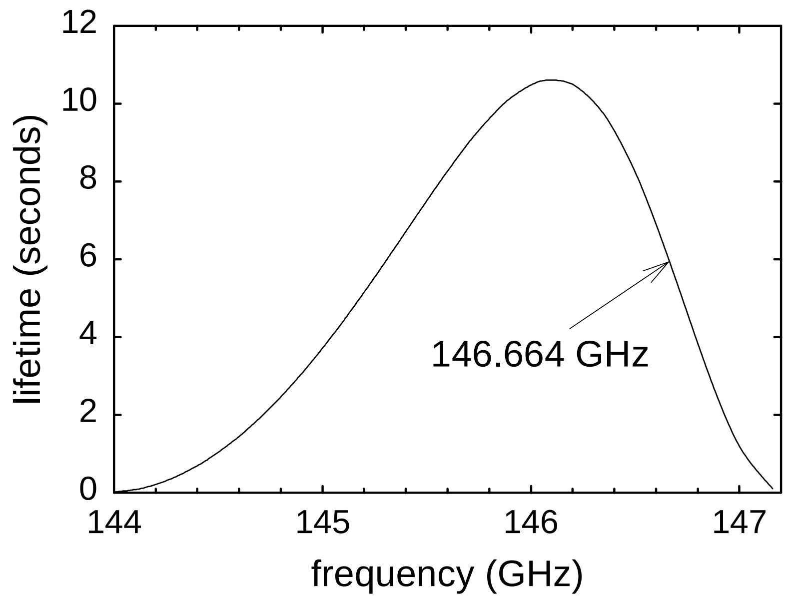

Figure 4.12: Calculated lifetime when the cyclotron oscillator is tuned between the TM_{135} and TE_{127} modes.

4.3 Quantum-Jump Thermometer

At a frequency of 147 GHz, non-negligible power is radiated from the walls of the trap electrodes even at 4 K, where the average number of thermal photons is 0.23 for this frequency (Fig. 4.13). These blackbody photons drive the electron cyclotron oscillator among its lowest Fock states, a process which we monitor in real time and use to determine the average temperature of the electron oscillator and radiation field.

4.3.1 Interaction with Thermal Radiation

A. Einstein was the first to anticipate that the stimulated absorption rate of a system in thermal equilibrium with a reservoir at temperature T is proportional to

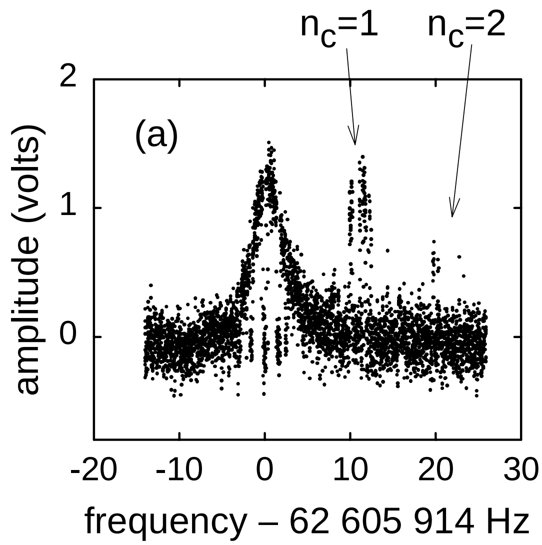

Figure 4.13: (a) Quantum jumps of the cyclotron oscillator observed with the in-phase electron response at 4 K. Partial resonances can be seen at axial frequencies corresponding to the first and second excited cyclotron states due to thermal photon excitations. (b) Closer inspection of the $n_c = 0$ resonance reveals long intervals of time (48, 68, and 76 seconds for the three biggest intervals in the picture) for which the electron is excited out of the cyclotron ground state.

the spectral density of radiation[4] u_ν [100],

$$\Gamma_{stim\ abs} = Bu_\nu, \tag{4.16}$$

where B, the Einstein coefficient for absorption, is a proportionality constant independent of T and ν. The function u_ν is the same thermal radiation spectrum that Planck explained using quantization of electromagnetic energy, and is equal to the energy of radiation at a certain frequency and temperature times the density of states at that frequency,

$$u_\nu = \langle l \rangle h\nu D(\nu). \tag{4.17}$$

[4]This is the energy per unit volume per unit frequency range.

Here, $h\nu$ is the photon energy and $D(\nu)$ the density of states at frequency ν, and $\langle l \rangle$ is the average number of photons in the mode of the electromagnetic field. The average photon number is determined by the Boltzmann distribution for a harmonic oscillator of frequency $\nu = \omega/2\pi$ and temperature T,

$$\langle l \rangle = \frac{1}{e^{\hbar\omega/kT} - 1}. \tag{4.18}$$

If we denote the spontaneous emission rate by γ,[5] one can show that [100]

$$\gamma = D(\nu) h\nu B. \tag{4.19}$$

Combining Eqs. (4.16)–(4.19) gives

$$\Gamma_{stim\ abs} = \frac{\gamma}{h\nu D(\nu)} u_\nu = \frac{\gamma}{h\nu D(\nu)} D(\nu) h\nu \langle l \rangle = \langle l \rangle \gamma. \tag{4.20}$$

This expression applies to both the stimulated absorption and the stimulated emission rates of the system because of detailed balancing,

$$\boxed{\Gamma_{stim\ abs} = \Gamma_{stim\ emiss} = \langle l \rangle \gamma.} \tag{4.21}$$

All of the temperature dependence in the above expression is contained in $\langle l \rangle$. The proportionality between Γ_{stim} and γ results from the fact that both thermal radiation and radiation from spontaneous emission are isotropic and unpolarized.

[5] Of course, it would be natural to use A for the spontaneous emission rate, since Einstein's original derivation was in terms of his A and B coefficients. We choose to denote this with the variable γ.

4.3.2 Temperature Measurement

We have monitored quantum jumps stimulated by thermal photons at five different trap temperatures. A one-hour sample of the data obtained is shown in Fig. 4.14. The temperatures displayed on each plot were determined from a RuO_2 temperature

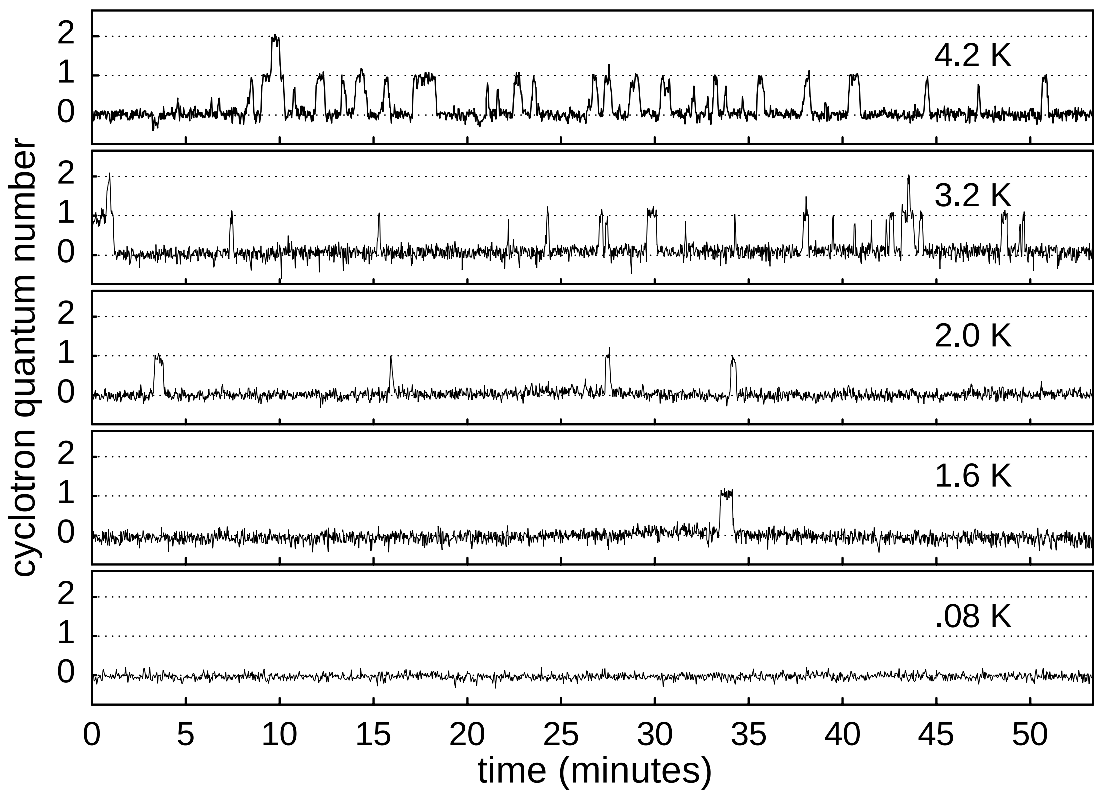

Figure 4.14: A sample of thermal-photon induced transitions at five different trap temperatures.

sensor mounted to the ring electrode of the trap. This figure is a nice demonstration of the suppression of thermal excitations as the temperature is lowered and of the cooling of a quantum oscillator to its ground state. The $T = 80$ mK environment is the one we will exploit to carry out future experiments.

The Boltzmann distribution describes the probability for a system to be in a quantum state $|n\rangle$,

$$P(n) = \frac{e^{-E_n/kT}}{\sum\limits_n e^{-E_n/kT}}. \tag{4.22}$$

Measuring the distribution of states for a system enables its temperature to be determined. Specifically, for a quantum mechanical harmonic oscillator of angular frequency ω at temperature T, the Boltzmann distribution (4.22) becomes,

$$P(n) = e^{-n\hbar\omega/kT}\left(1 - e^{-\hbar\omega/kT}\right). \tag{4.23}$$

The temperature of the cyclotron oscillator can be determined by fitting $P(n)$ versus n to this expression. The probability distributions for the four temperatures between 1.6 K and 4.2 K are shown in Fig. 4.15. Figure 4.16 plots the average temperature of the oscillator and the average occupation number $\langle n\rangle$,

$$\langle n\rangle = \sum_n nP(n) = \frac{1}{e^{\hbar\omega/kT} - 1}, \tag{4.24}$$

versus trap temperature.

Figure 4.16 does not include a temperature for the 80 mK plot shown in Fig. 4.14. At this temperature, the oscillator is expected to stay in the ground state for 10^{32} years without being thermally excited. We can only put an upper limit on the temperature for this case. At temperature T, the probability that at time t a thermal photon has been absorbed is

$$P(t) = 1 - e^{-\langle l\rangle\gamma t}, \tag{4.25}$$

where $\Gamma_{stim\ abs} = \langle l\rangle\gamma = 0.077\langle l\rangle$. If after time t no excitation is observed, we can,

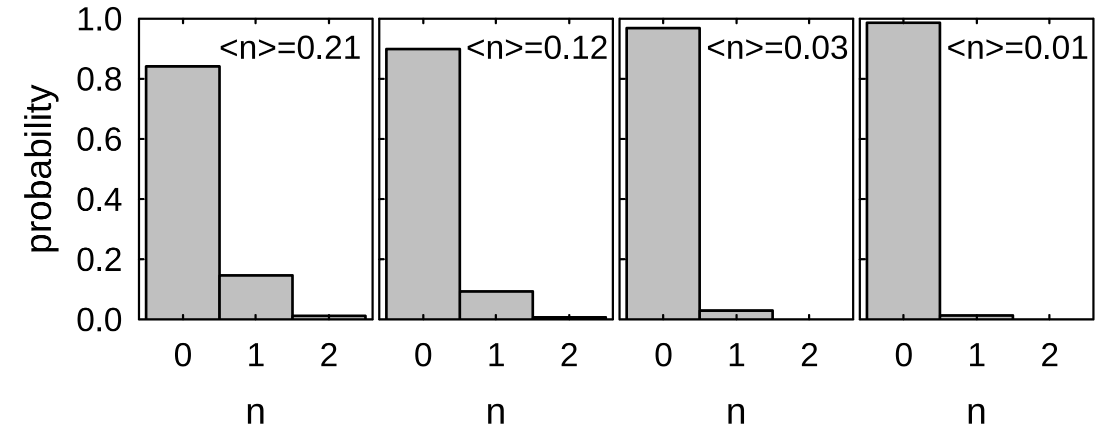

Figure 4.15: Measured distribution of energy levels at 4.2 K, 3.2 K, 2.0 K and 1.6 K.

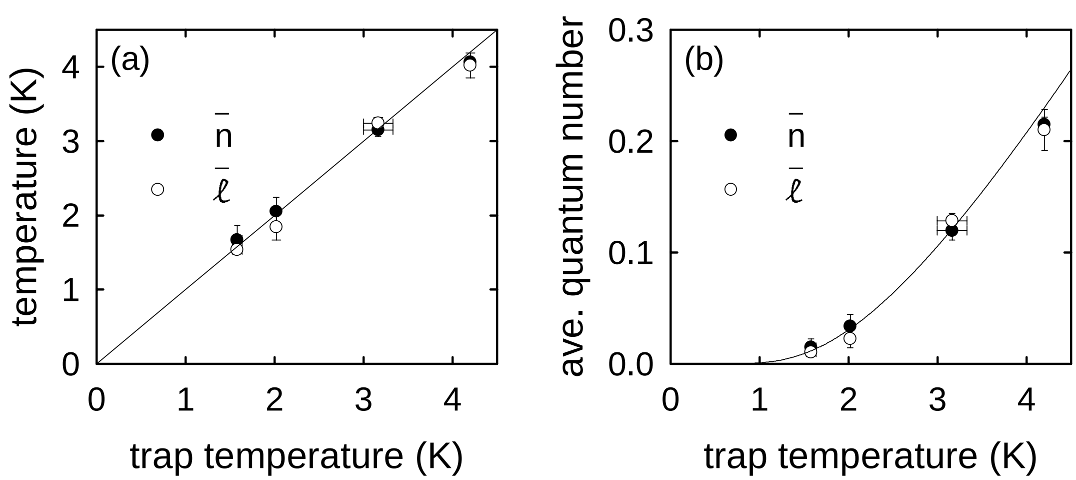

Figure 4.16: Measurement of (a) temperature and (b) average occupation/photon number for the electron cyclotron oscillator and radiation field. The trap temperature is measured with a RuO_2 sensor.

with confidence level C, place an upper limit on the temperature of the system by solving the above equation for t and identifying $P(t)$ with C,

$$kT \leq \frac{\hbar\omega}{\ln\left(1 - \frac{\gamma t}{\ln(1-C)}\right)}. \tag{4.26}$$

Five hours of continuous observation yielded no excitations, prompting us to claim with a 68% confidence level that $T < 1$ K.

We can also use the thermally induced quantum jumps to measure the average temperature of the resonant mode of the radiation field. Rates for the electron to make transitions from $|0\rangle$ to $|1\rangle$ and from $|1\rangle$ to $|0\rangle$ can be measured from the data, as shown in Fig. 4.17. The process of going from $|0\rangle$ to $|1\rangle$ can only occur due to the absorption of a photon (*i.e.* stimulated absorption). The reverse process can be the result of stimulated emission or spontaneous emission. Using Eq. (4.21) above we have

$$\Gamma_{0\to1} = \Gamma_{stim\ abs} = \langle l\rangle\gamma, \tag{4.27}$$

$$\Gamma_{1\to0} = \Gamma_{stim\ emiss} + \gamma = (\langle l\rangle + 1)\gamma. \tag{4.28}$$

These two equations determine the two unknowns γ and $\langle l\rangle$. The 1.6 K data in Fig. 4.17 give a spontaneous emission rate of 13 seconds. The plot of $\langle l\rangle$ versus temperature is included in Fig. 4.16 along with the results for $\langle n\rangle$. The agreement displayed between $\langle n\rangle$ and $\langle l\rangle$ is expected since the electron comes into thermal equilibrium via the blackbody photons in the cavity.

4.3.3 Analysis

For the data analysis, an event threshold was set at one-half of the quantum-jump signal size. The duration of an "event" was measured from the point the signal

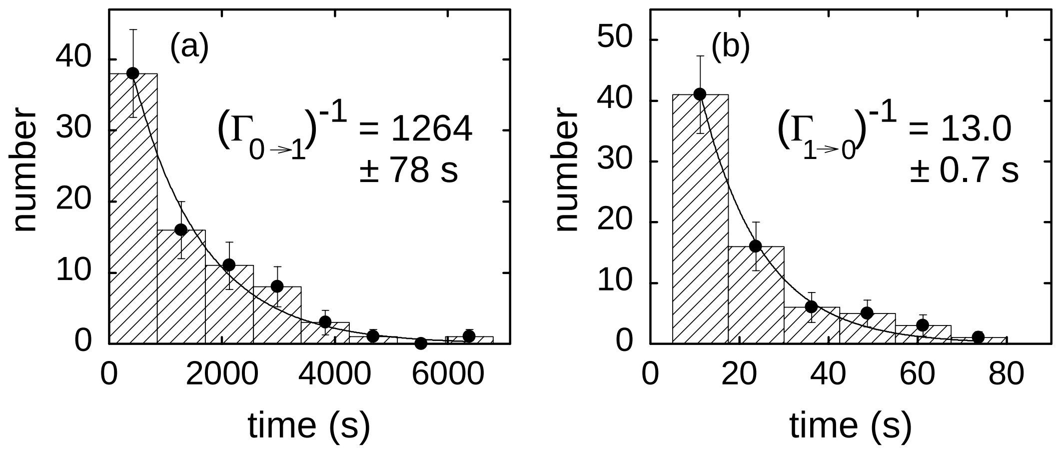

Figure 4.17: Histogram of dwell times in the (a) $n = 0$ and (b) $n = 1$ states at 1.6 K. The exponential fit gives the average (stimulated) absorption and emission rates. The absence of events at short times is discussed in the text.

crossed the threshold on the initial transition to the same point on the subsequent transition. Most times between transitions were determined by the computer, but some excitations (especially those of short duration) had to be adjusted by hand. Because of the response time of our lock loop, only events lasting five seconds or longer, those detected reliably, were included in fits to an exponential function.

The recorded dwell times in $n = 0$ and $n = 1$ needed to be scaled because of software delays. The dwell times were measured using Labview's counter which was compared to the computer clock approximately every 20 minutes. Typically, the counter time had to be corrected by 20%. Uncertainties in this correction are included in uncertainties in the measured lifetime.

The measured $P(n)$ were fit to the Boltzmann distribution in Eq. (4.23) to determine the electron cyclotron temperature T. From this temperature $\langle n \rangle$ was determined from Eq. (4.24). The uncertainty in T propagates to $\langle n\rangle$ as

$$\frac{\delta\langle n\rangle}{\langle n\rangle}=\frac{\hbar\omega_c/kT^2}{1-e^{-\hbar\omega_c/kT}}\delta T. \tag{4.29}$$

The average photon number is derived from the transition rates between Fock states as previously discussed. (The bin size used in the histograms of the dwell times was adjusted as a check.) The uncertainty in $\langle l\rangle$ becomes

$$\frac{\delta\langle l\rangle}{\langle l\rangle}=\frac{\Gamma_{1\to 0}}{\Gamma_{1\to 0}-\Gamma_{0\to 1}}\sqrt{\left(\frac{\delta\Gamma_{0\to 1}}{\Gamma_{0\to 1}}\right)^2+\left(\frac{\delta\Gamma_{1\to 0}}{\Gamma_{1\to 0}}\right)^2}. \tag{4.30}$$

Finally, the error on $T\left(\langle l\rangle\right)$ is

$$\frac{\delta T}{T}=\left(\frac{1}{\ln\left(\frac{(1+\langle l\rangle)}{\langle l\rangle}\right)}\right)\left(\frac{1}{\langle l\rangle\left(1+\langle l\rangle\right)}\right)\delta\langle l\rangle. \tag{4.31}$$

4.4 Photon Antibunching

Three phenomena demonstrating nonclassical behavior of light are sub-Poissonian amplitude fluctuations, squeezed light, and photon antibunching [101]. Light is antibunched if emitted photons *anti*correlate at short times. Unlike bunching, it is an intrinsically quantum mechanical effect.

Antibunching is revealed through the correlation function $g_{(2)}(\tau)$, which gives the probability that, once a photon has been emitted, a second photon will be emitted a time τ later. A positive slope at $\tau = 0$ indicates antibunching. The photons emitted when a system undergoes quantum jumps between two states are antibunched [90]. After the emission of one photon, a second photon cannot be radiated until a time delay has accumulated, which includes the time in the ground state before re-excitation and the time in the excited state before decay.

We can deduce $g_{(2)}(\tau)$ for our system by assigning to every transition from $|1\rangle$ to $|0\rangle$ the emission of a single microwave photon. Figure 4.18 shows the correlation function for one of our data sets. We analyzed a sequence of quantum jumps stimulated by an external microwave drive, detuned slightly above resonance to 146.6646 GHz, at a trap temperature of 80 mK. To the electron moving through the bottle field, the frequency of this drive appears to be fluctuating (*i.e.* it is an incoherent drive, see Section 5.1).

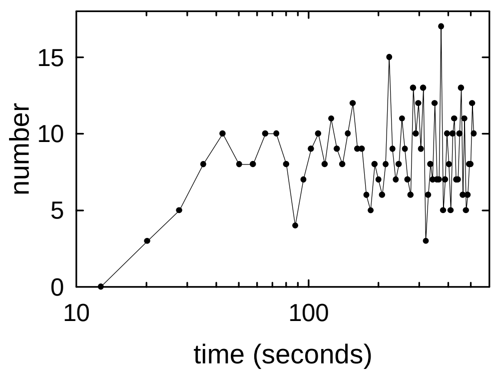

Figure 4.18: Photon antibunching with the system primed by an external drive. The existence of antibunching is marked by a decrease in $g_{(2)}(\tau)$ as $\tau \to 0$.

We can also include in $g_{(2)}(\tau)$ photons emitted during the $|2\rangle$ to $|1\rangle$ transition. In this case, there can be transitions from $|1\rangle$ to $|0\rangle$ almost immediately after $|2\rangle$ to $|1\rangle$ without the need for the system to be re-excited. For the data analyzed, the dip in the correlation function at $\tau = 0$ becomes barely perceptible. The quantum mechanical signature of antibunching is obscured by introducing just one more energy level to the analysis.

4.5 Topics in Quantum Measurement

4.5.1 QND Measurement

The magnetic-bottle coupling allows the cyclotron level of our electron to be measured from the frequency of the RF current induced in the trap electrodes by the orthogonal axial motion. This detection does not "disturb" an eigenstate of the cyclotron motion — if we observe the electron to be in state $|n\rangle$, a subsequent measurement will reveal the same state, unless an absorption or emission event takes place. These events are due to the environment rather than the detection process.

This falls into the category of a "quantum nondemolition" (QND) measurement [102]. Formally, a QND measurement corresponds to an observable that commutes with the Hamiltonian. In our case,

$$V_{obs} \propto z^2 a_c^\dagger a_c, \tag{4.32}$$

for which $[V_{obs}, H_c] = 0$. QND measurements are important for gravity-wave detection [103] and may serve to lend insight into the nature of quantum measurement.

4.5.2 Measurement Time

Our "act of measurement" takes some time, t_m, to be completed [94, 104, 105]. This measurement time is difficult to determine, but it has been estimated for the case of measuring the spin state of an electron in a Penning trap [104, 105]. In these articles, measurement times are derived by considering how much averaging needs to occur to obtain a determination of the spin state in the presence of noise in the system. We will simply quote these estimates and evaluate them for our experimental parameters. The use of these results as approximations in our system is very reasonable since the detection process in each apparatus is fundamentally identical and the signal determining the spin state is the same size as the signal determining the cyclotron state. (Additionally, the author in reference [94] derives a similar expression that is applicable to measurements of the cyclotron level.)

The limit placed on the measurement time by thermal noise from the detection circuit (which the electron sees as a resistance R, recall Fig. 3.1) is found to be [105],

$$t_m \approx \frac{2\gamma_z k_B T_R}{\delta^2 W_{zs}}. \tag{4.33}$$

Here, γ_z is the axial (resistive) damping rate, k_B is the Boltzmann constant, T_R is the temperature of the detection resistor, $\delta = \Delta\omega_z$ is the shift in ω_z for a single quantum-level transition in the cyclotron oscillator, and W_{zs} is the energy in the axial oscillator. Noise from additional amplifiers, etc., can make the achieved measurement time longer than this value.

The measurement time required in the presence of only quantum fluctuations in the axial oscillator at $T_z = T_R = 0$ is the *intrinsic* measurement time [105],

$$t_m^* \approx \frac{\gamma_z}{\delta^2 \overline{k}}, \tag{4.34}$$

where $\overline{k}$ is the average quantum level of the driven axial oscillation. This is regarded by H. Dehmelt as the time for reduction of the wave function. This measurement time must be at least as long as the inverse linewidth, which indicates the time over which the cyclotron energy is not well-defined.

One assumption made in the derivation of these expressions does not apply to our experiment. Equation (11) of reference [104] is only valid for $\delta < \gamma_z/2$; in our system, $\delta > \gamma_z$. This can be accounted for by scaling the calculated times by a factor of 10^2 for our present parameters. Evaluating the above expressions for our system and applying this correction gives

$$t_m \approx 4 \text{ s} \quad \text{and} \quad t_m^* \approx 5 \times 10^{-4} \text{ s}, \tag{4.35}$$

using a temperature of 20 K and a driven amplitude of 30 μm for t_m and $\overline{k} = 1000$ for t_m^*. The measurement time t_m^* is much longer than the inverse linewidth, which can be as short as 1 μs when actively detecting.

4.5.3 Quantum Zeno Effect

The quantum Zeno effect is the inhibition of transitions caused by frequent measurement of a system [106]. Consider a system that is repeatedly measured while trying to evolve from one eigenstate of an observable to another. If the measurement is completed during the period of quadratic time evolution of the system (see the next section), observation can keep the system from making transitions. This was demonstrated beautifully by Itano, *et al.*, with several thousand trapped ions by inhibiting a driven transition with frequent "measurement pulses" [106].

4.5.4 Zeno Time

Consider a two-state system in which an initial state $|i\rangle$ is unstable and decays into a final state $|f\rangle$. If we make a measurement on the system at time t, the probability of observing that it will still be in $|i\rangle$, *i.e.* that it does *not* decay, is

$$P(t) = |\langle i|e^{-iHt/\hbar}|i\rangle|^2. \tag{4.36}$$

Expanding this for short times, and keeping only terms to order t^2,

$$P(t) = \left| \langle i| \left(1 - \frac{iHt}{\hbar} - \frac{H^2 t^2}{2\hbar^2} - \dots \right) |i\rangle \right|^2 \tag{4.37}$$

$$= \left(1 + \frac{it}{\hbar}\langle i|H|i\rangle - \frac{t^2}{2\hbar^2}\langle i|H^2|i\rangle\right)\left(1 - \frac{it}{\hbar}\langle i|H|i\rangle - \frac{t^2}{2\hbar^2}\langle i|H^2|i\rangle\right)$$

$$= 1 - \frac{t^2}{\hbar^2}\langle i|H^2|i\rangle + \frac{t^2}{\hbar^2}\langle i|H|i\rangle^2.$$

If we define

$$\Delta E \equiv \sqrt{\langle i|H^2|i\rangle - \langle i|H|i\rangle^2} \quad \text{and} \quad \tau_z \equiv \frac{\hbar}{\Delta E}, \tag{4.38}$$

then

$$P(t) = 1 - \frac{t^2}{\tau_z^2} + \dots, \tag{4.39}$$

where τ_z is the *Zeno time* for the system.

If we write the Hamiltonian of the system as the sum of three terms, the Hamiltonian of the particle, the Hamiltonian of the radiation field, and the interaction Hamiltonian ($H = H_{e^-} + H_\gamma + H_I$), the only term that gives a non-vanishing contribution to τ_z is $H_I = \frac{e}{m}\boldsymbol{A}\cdot\boldsymbol{p}$. In our case,

$$\frac{1}{\tau_z^2} = \langle 1, 0|H_I^2|1, 0\rangle, \tag{4.40}$$

where $|1, 0\rangle$ is the state with the cyclotron oscillator excited to $n = 1$ and no photons in the mode (*i.e.* we are considering $|1, 0\rangle$ to be our initial state $|i\rangle$ discussed above). We can sum over a complete set of intermediate states and consider just one additional electron state ($n = 0$) to get

$$\frac{1}{\tau_z^2} = \sum_\beta \int_0^\infty d\omega\, |\langle 1, 0|H_I|0, 1_{\omega\beta}\rangle|^2 \equiv \sum_\beta \int_0^\infty d\omega\, |\phi_\beta(\omega)|^2\,, \tag{4.41}$$

where the field is expanded in the energy-angular momentum basis following the convention in reference [107]. To calculate τ_z, we need to evaluate the matrix element $\phi_\beta(\omega) = \frac{e}{m}\langle 1,0|\boldsymbol{A}\cdot\boldsymbol{p}|0,1\rangle$.

We outline this calculation for the case of an electron in a magnetic field in *free space*. The cyclotron oscillator wave function for level n is the nth-order Hermite polynomial $\mathcal{H}_n$ times a plane wave [108]. The overlap between the $n=0$ and $n=1$ wavefunctions falls off exponentially as

$$\exp\left(-x^2\frac{m\omega_c}{\hbar}\right), \tag{4.42}$$

which allows us to introduce a natural frequency cutoff,

$$\nu_{\text{cutoff}} = c\Lambda = c\sqrt{\frac{m\omega_c}{\hbar}} = 2.7\times 10^{16}\ \text{Hz}. \tag{4.43}$$

Λ is a common parameter used in carrying out estimates of the Zeno time in the electric dipole approximation [107, 109].

Evaluation of the matrix element ultimately gives

$$\phi_\beta(\omega) = \frac{e}{m}\langle 0,1|\boldsymbol{A}\cdot\boldsymbol{p}|1,0\rangle = \eta\sqrt{\omega}\exp\left(-\frac{\hbar\omega^2}{4(mc^2\omega_c)}\right) \tag{4.44}$$

where

$$\eta = \sqrt{\frac{\gamma}{2\pi\omega_c}\exp\left(\frac{\hbar\omega_c}{2mc^2}\right)} \tag{4.45}$$

and γ is the spontaneous emission rate. Important steps in the calculation include deriving the photon momentum to be along the $\hat{x}$ direction (for our choice of coordinates — see Eq. (4.42)) and using the relation $|\phi_\beta(\omega_0)|^2 \approx \gamma/(2\pi)$, where ω_0 is the resonant frequency. This relation is discussed in reference [107] and allows the many pre-factors involved in the calculation to be written in terms of γ. The Zeno time becomes

$$\tau_z = \left(\eta c\sqrt{\frac{m\omega_c}{\hbar}}\right)^{-1} = \frac{1}{\eta c\Lambda} = 9 \times 10^{-11} \text{ secs.} \tag{4.46}$$

The time during which decay can be inhibited by measurement corresponds to $t \ll \tau_z$, where the decay probability has a quadratic time dependence (recall expression (4.39) above). Thus, the measurement time required to inhibit decay (in free space) is very short. Several authors claim that this time τ_m should be given roughly by [110, 111, 109]

$$\tau_m \sim \tau_z \frac{\tau_z}{\tau_L}, \tag{4.47}$$

where τ_L is the lifetime of the system. This expression for τ_m comes from equating Eq. (4.39) to the expansion of the long-time behavior, $e^{-\gamma t} = 1 - \gamma t + \frac{1}{2}\gamma^2 t^2 \ldots$, at short times. Where these curves cross is approximately τ_m, which is 6×10^{-20} sec for the free-space approximation of our system.

We expect these times to be somewhat longer inside a cavity. In this case, a photon emitted into a mode with quality factor Q will remain in the cavity for a finite time, $\tau_Q = Q/\omega$. Since the electron and photon are in an entangled state until the photon is absorbed by the cavity walls, decay is non-exponential (is even reversible) on that timescale. For the highest Q modes in our trap, this is about 50 ns and is roughly τ_m in the cavity [112]. Thus, the time interval during which a measurement would need to be completed to alter the decay rate of the cyclotron oscillator is too short to observe an effect.

4.6 Future Experiments

The $n = 0$ and $n = 1$ Fock states of a mode of the radiation field and of the motion of trapped atoms have been generated and observed [13, 14]. The only Fock states produced with $n > 1$ rely on an indirect and destructive measurement of the eigenstates [12]. We have directly observed Fock states of our cyclotron oscillator, as high as $n = 4$, and should be able to generate low-n Fock states on demand.

Because of special relativity, the electron cyclotron oscillator is slightly anharmonic [88]. The transition frequency between levels n and $n + 1$ is

$$\omega_{n,n+1} = \omega_c - n\delta, \tag{4.48}$$

where $\delta/\omega_c \approx 10^{-9}$ (see Fig. 4.19). This should allow us to generate particular Fock states by applying a succession of pi pulses at different frequencies. Our oscillator at base temperature will be in the ground state; application of a pi pulse at ω_c would put us into the $n = 1$ state. Following this with an $\omega_c - \delta$ pi pulse would put the system into $n = 2$, and so on. Because the decay rate from state $|n\rangle$ is $n\gamma$, higher-n Fock states will be more difficult to observe.

Success of this technique will rely on a cyclotron linewidth that is more narrow than 1 ppb, the separation between transition frequencies. We expect a 1 ppb width at 50 mK (Section 5.1.2). Additionally, we need to be able to complete a pi pulse quickly compared to the decoherence time of the oscillator.

We may be able to observe an effect of the zero-point energy of the cyclotron oscillator. The magnetic bottle couples the z-component of the electron's magnetic moment into its axial frequency as revealed in Eq. (4.12). Eliminating the bottle coupling when the cyclotron motion is in its ground state, $n_c = 0$, will change the

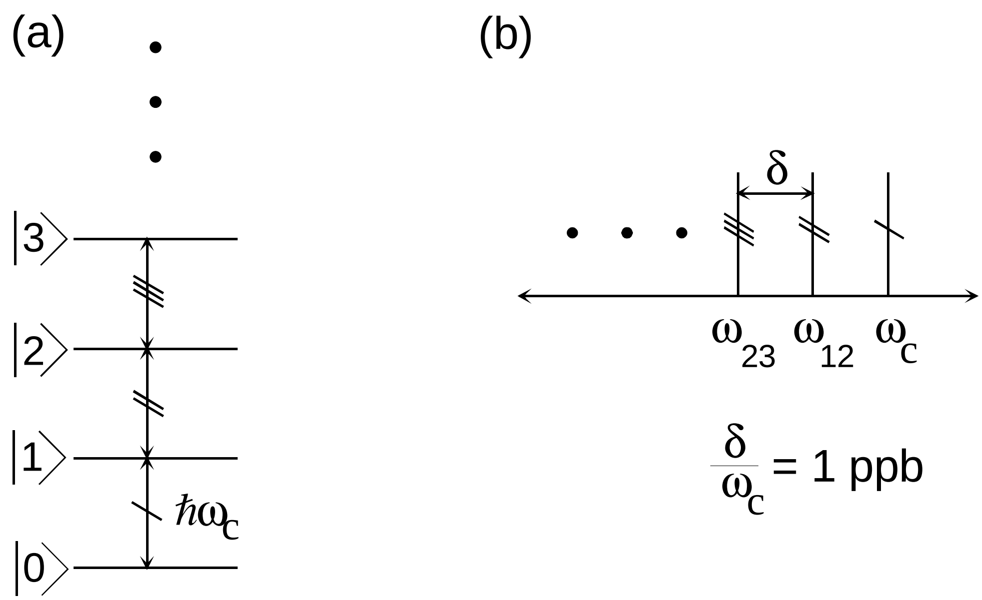

Figure 4.19: Successive transition frequencies for the cyclotron oscillator decrease by 1 ppb.

axial frequency by

$$\frac{B_2 \mu_b}{m\omega_{z0}}(1 + g n_s). \tag{4.49}$$

Depending on the spin state, either ν_z will shift by 12.3 Hz or will remain constant when the coupling is removed, revealing the zero-point energy in the oscillator.

Cancelling such a large magnetic gradient (recall, $B_2 \approx 1540$ T/m^2) is difficult. Since the 12.3 Hz shift produces such a well-resolved signal, canceling even 10–20% of B_2 should produce an observable signature of the zero-point motion of the cyclotron oscillator.

Chapter 5

Toward $g - 2$

The electron g factor has been measured to 4 parts in 10^{12} using a single electron in a 4 K Penning trap by Van Dyck, *et al.* [31]. The uncertainty in the estimated shift of the electron's cyclotron frequency from its free-space value due to the presence of the trap cavity was the dominant contribution to the final error assigned. Our cylindrical trap geometry should allow us to greatly reduce this cavity shift and estimate the residual shift more accurately.

The electron's stochastic thermal motion through the inhomogeneous bottle field causes the cyclotron oscillator to sample a randomly varying magnetic field, broadening the resonance. The temperature of our system is so low that we will reduce this thermal broadening compared to the 1987 g-factor measurement and at the same time achieve greater sensitivity to excitations by using a stronger bottle field. Our increased sensitivity allows us to perform a cyclotron-frequency measurement by exciting only the $n = 0$ to $n = 1$ transition, avoiding shifts introduced by special relativity. The reduced cyclotron temperature suppresses thermal excitations out of the ground state which otherwise would obscure this signal.

An electron in a magnetic field moves in a cyclotron orbit with angular frequency

$$\omega_c = \frac{eB}{m}. \tag{5.1}$$

Its intrinsic magnetic-dipole moment causes its spin to precess about the direction of the field with an almost identical frequency,

$$\omega_s = \frac{g}{2}\left(\frac{eB}{m}\right) = \frac{g}{2}\omega_c. \tag{5.2}$$

Measuring ω_s and ω_c for an electron in a Penning trap provides an experimental value for its g factor.

The energy-level diagram for an electron in a magnetic field is shown in Fig. 5.1. Measuring the anomaly

$$a = \frac{g-2}{2} = \frac{\omega_s - \omega_c}{\omega_c} \equiv \frac{\omega_a}{\omega_c} \tag{5.3}$$

and subsequently determining $g = 2(a+1)$ results in higher precision than measuring $g = \omega_s/\omega_c$ directly. The uncertainty becomes

$$\frac{\Delta g}{g} = \frac{\Delta a}{a+1} \approx \frac{\Delta a}{1} \approx 10^{-3}\frac{\Delta a}{a}, \tag{5.4}$$

using $a \approx 10^{-3}$. The anomaly interval is illustrated in Fig. 5.1.

The 1987 measurement achieved a precision of 4 ppb for the electron anomaly. With the improvements we have made to reduce the systematics discussed, we anticipate that at least a factor of ten reduction in uncertainty should be possible. This will require measurements of ω_a and ω_c to approximately 0.1 ppb.

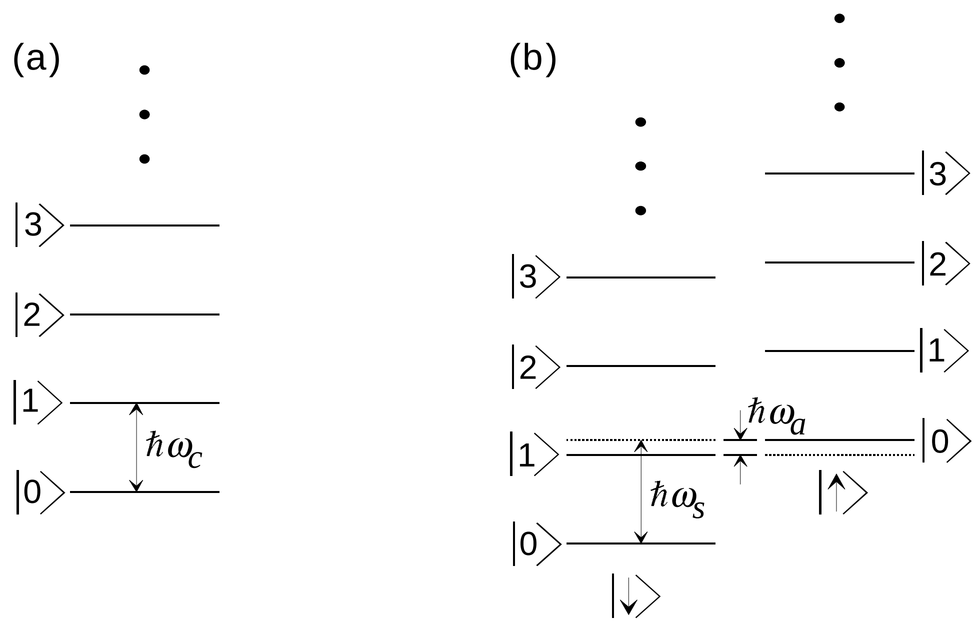

Figure 5.1: (a) Landau levels for an electron cyclotron oscillator. (b) Energy levels illustrating the Zeeman splitting. The energy difference between $|\uparrow\rangle|n\rangle$ and $|\downarrow\rangle|n{+}1\rangle$ is $\hbar\omega_a$. The entire spectrum for an electron in a Penning trap would include the axial and magnetron states [48].

5.1 Reduced Axial Temperature

The added magnetic-field gradient couples the electron's axial motion to it spin state and cyclotron oscillator. Because of this coupling, shifts in the axial frequency arise from excitations in the high-frequency systems and serve as the detection signal for these excitations. This beneficial aspect of the bottle coupling that allows detection of 150 GHz transitions,

$$\Delta E_{c,s} \to \Delta \nu_z, \tag{5.5}$$

is the subject of Section 4.1.2. Similarly, changes in the axial energy alter the frequencies of the cyclotron and spin systems,

$$\Delta E_z \rightarrow \Delta \nu_{c,s}. \tag{5.6}$$

This is the unavoidable “back action” that the detector imposes on the system it measures. Thermal fluctuations in the axial oscillator’s energy are accompanied by fluctuations in ν_c and ν_s, broadening or shifting the resonances in proportion to the axial temperature. This section treats the detrimental effect of the magnetic bottle, and how it can be avoided with the low-temperature environment in our system.

5.1.1 General Magnetic Lineshape

The electron’s axial motion is in thermal equilibrium with a tuned circuit at temperature T_z (Section 2.6). Its average energy fluctuates, with the spread of oscillation amplitudes given by the Boltzmann distribution,

$$P(z) = \frac{1}{Z} \exp\left(-\frac{1}{2}\frac{m\omega_z z^2}{k_B T_z}\right), \tag{5.7}$$

where $Z = \sqrt{2\pi kT/m\omega_z^2}$ is the partition function for the system. Amplitude variations are seen by the electron as fluctuations in the magnetic field because of the $B_2 z^2 \hat{\boldsymbol{z}}$ term of the bottle field (recall Eq. (4.2)). Specifically, the cyclotron, spin, and anomaly frequencies acquire the form,

$$\begin{aligned} \omega &= \lambda \frac{e}{m}\left(B + B_2 z^2\right) \\ &= \omega_0\left(1 + \varepsilon z^2\right), \end{aligned} \tag{5.8}$$

where B is the main trapping field, $\varepsilon = B_2/B$ and ω_0 is the frequency at $z = 0$. We use a constant λ which is 1, $g/2$ and a for the three frequencies, respectively. The stochastic variations in ω are characterized by a *linewidth parameter* [113, 114, 48],

$$\Delta\omega = \omega_0 \varepsilon \left\langle z^2 \right\rangle, \tag{5.9}$$

where $\langle z^2 \rangle$ is an ensemble average. This can be put into a more useful form by relating $\langle z^2 \rangle$ to an effective temperature using the equipartition of energy,

$$\frac{1}{2} k_B T_z = \frac{1}{2} m \omega_z^2 \left\langle z^2 \right\rangle, \tag{5.10}$$

giving

$$\Delta\omega = \omega_0 \varepsilon \left(\frac{k_B T_z}{m \omega_z^2} \right) = 2.7 \times 10^{-8} \omega_0 T_z \tag{5.11}$$

for our parameters (see Table 5.1).

parameter	**measured value**	**derivation**
ω_z	$2\pi(63.95)$ MHz	measured
ω_c	$2\pi(146.664\ 2)$ GHz	measured
ω_a	$2\pi(170.079\ 4)$ MHz	$\frac{g}{2}\omega_c$
γ_z	$2\pi(5)$ Hz	measured
B_2	1540 T/m^2	measured[a]
B	5.24 T	$m\omega_c/e$

[a]See Table 4.1 for both the calculated and measured values of B_2.

Table 5.1: Experimental parameters relevant to the discussion of magnetic lineshapes.

The fluctuating resonant frequency (ω_c, ω_s, or ω_a) introduces perturbations to the standard Lorentzian lineshape that we expect. The *line profile*,[1] the Fourier transform of the correlation function $\chi(t, t')$ for frequency fluctuations, describes

[1]Using the term from the literature [113, 114, 48].

the resonance shape. Its form depends on the relative size of $\Delta\omega$ and γ_z, *i.e.*, the average time between the field fluctuations (determined by $1/\gamma_z$) versus the time required for the frequency ω to be established (determined by $1/\Delta\omega$). The line profile is easiest to understand in the two limits (i) $\Delta\omega \gg \gamma_z$, the "exponential limit", and (ii) $\Delta\omega \ll \gamma_z$, the "Lorentzian limit".

In the exponential limit, the frequency ω registers quickly compared to the fluctuations in B so that the motion samples each of the values of the stochastically varying field. The line profile acquires the form [114]

$$\chi(\omega) = \frac{\Theta(\omega - \omega_0)}{\Delta\omega} \exp\left(-\frac{\omega - \omega_0}{\Delta\omega}\right), \tag{5.12}$$

where Θ is the "step function". The exponential reflects the Boltzmann distribution of axial energies (Eq. (5.7)) and has a $1/e$ width of $\Delta\omega$. The abrupt low-frequency edge of the profile corresponds to the cyclotron frequency due to just the uniform field.

In the Lorentzian limit, the motion is unable to follow the field fluctuations and sees an average field of $B + B_2 \langle z^2 \rangle$. Therefore, the resultant profile is a Lorentzian with a center frequency shifted by $\Delta\omega$ [114],

$$\chi(\omega) = \frac{\Delta\omega^2/\pi\gamma_z}{(\omega - \omega_0 - \Delta\omega)^2 + (\Delta\omega^2/\gamma_z)^2}. \tag{5.13}$$

The shape of the line profile in the general case is a combination of these two shapes and is given by [114]

$$\chi(\omega) = \frac{4}{\pi}\mathrm{Re}\frac{\gamma'\gamma}{(\gamma' + \gamma_z)^2} \sum_{n=0}^{\infty} \frac{(\gamma' - \gamma_z)^{2n} (\gamma' + \gamma_z)^{-2n}}{\left(n + \frac{1}{2}\right)\gamma' - \frac{1}{2}\gamma_z - i(\omega - \omega_0)} \tag{5.14}$$

where $\gamma' = (\gamma_z^2 + 4i\gamma_z\Delta\omega)^{1/2}$ and "Re" is for the real part.

A low axial temperature is crucial in order to achieve narrow, unshifted resonances. We mentioned in Section 2.6 that the reservoir coupled to the axial motion is at a temperature much higher than the base temperature when the FET is active. It is therefore necessary to stimulate cyclotron and anomaly transitions with the FET off so that a low T_z is realized. The transistor will then be activated after the excitation drive has been applied to read out whether a transition has occurred. The "frequency-shift detection" scheme (Section 2.2.1) requires driving the axial motion to obtain a dispersive response that can be used to lock ω_z. This axial drive in effect amplifies T_z because the quadratic component in the bottle field introduces a cross term,

$$B_2 z^2 = B_2 \left(z_d + z_{th}\right)^2 = \ldots + 2B_2 z_d z_{th}, \tag{5.15}$$

where we have divided the amplitude into a driven and a thermal part. In order to use our low-temperature environment to reduce the broadening from the bottle field, both the FET and the axial drive need to be turned off while a cyclotron or anomaly excitation drive is applied.

5.1.2 Cyclotron Resonance

Since $\Delta\omega_c \gg \gamma_z$, the cyclotron resonance for our system will be close to the exponential limit, Eq. (5.12), for all of our operating temperatures (Fig. 5.2(a)). This is emphasized in Fig. 5.3, which displays calculated line profiles $\chi_c(\nu)$ for 4.2 K and 50 mK. Dotted lines map out the exponential limit of the line profile for each temperature, and the solid lines are the exact solution using Eq. (5.14).

For each temperature, the entire response is shown along with a close-up of the low-frequency edge. The dramatic advantage of our reduced temperature is

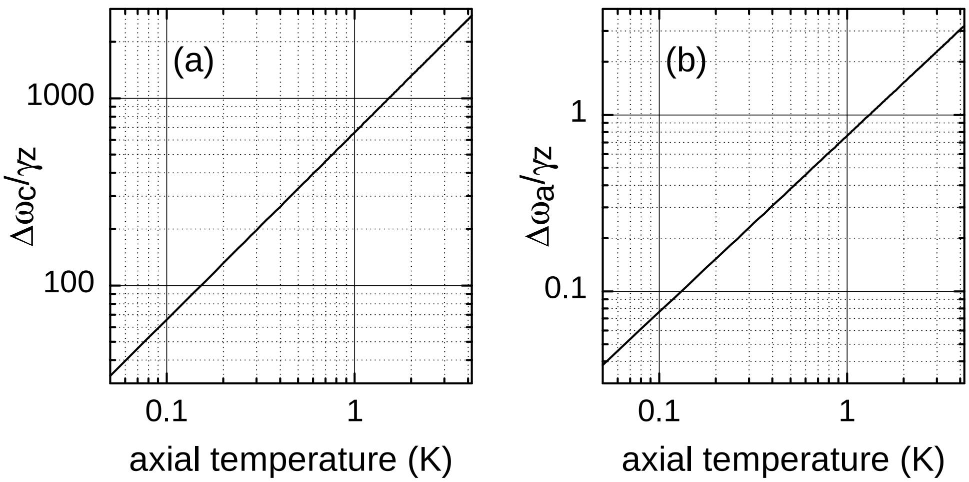

Figure 5.2: Ratio of linewidth parameter to axial damping width as a function of T_z for the (a) cyclotron and (b) anomaly resonances.

emphasized by the arrows in the figure. The entire frequency axis of the 50 mK graph scales to the interval marked in Fig. 5.3(a). The arrows in Fig. 5.3(b) indicate the entire vertical axis of the 4.2 K resonance — because the low-temperature resonance is less "washed out", the peak is much higher.

The most recent g-factor measurement [31], carried out with $T_z \sim 4$ K and $B_2 = 155$ G/cm^2, deduced ν_c to 1 ppb using the sharp low-frequency edge of the 10–20 ppb-wide cyclotron resonance. At 50 mK, we expect a cyclotron width of 1 ppb (≈ 150 Hz) and the lineshape shown in Fig. 5.3(b). Splitting this line by only 10% will give the desired 0.1 ppb precision for ν_c.

We intend to map out a cyclotron resonance by counting quantum jumps from $n = 0$ to $n = 1$ as we sweep a microwave drive through resonance. Watching jumps of the oscillator is useful for two reasons. First, a transition of one quantum level is so well-resolved that it is only necessary to make excitations to the first excited

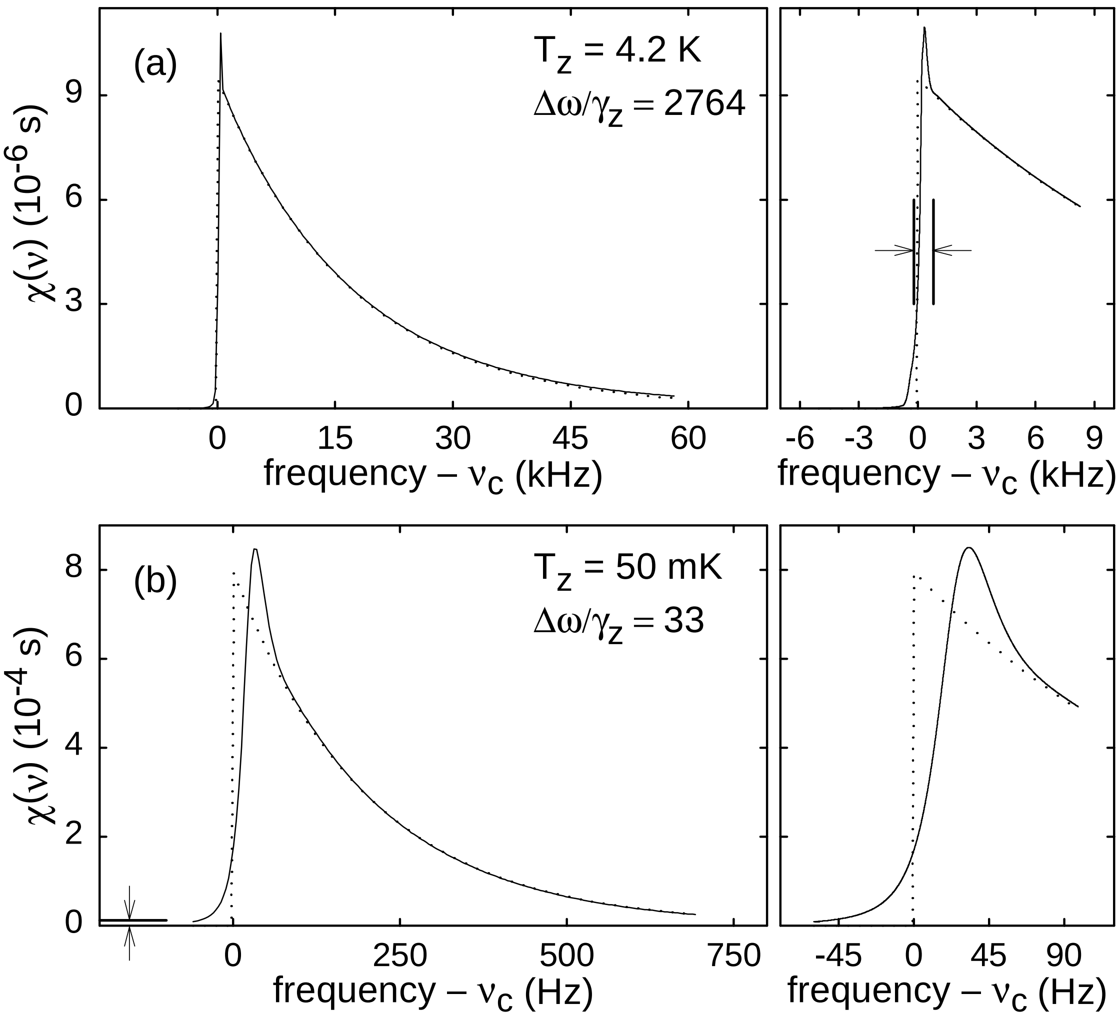

Figure 5.3: Calculated cyclotron line profiles $\chi_c(\nu)$. Solid curves are the calculated lineshapes, and dotted lines show the exponential limit for (a) 4.2 K and (b) 50 mK. The entire response for the two temperatures is shown along with a "close-up" of the low-frequency edge, which becomes less abrupt as we diverge from limit (i). For perspective, the arrows in (a) indicate the entire 1 kHz horizontal span of the 50 mK plot, and the arrows in (b) mark the entire 1.2×10^{-5} sec vertical span of the 4.2 K plot.

state. This is crucial for achieving a 1 ppb linewidth since relativistic anharmonicity broadens the resonance by at least 1 ppb as soon as the system is excited past the $n = 1$ level (recall the anharmonicity discussion in Section 4.6). Second, in order to realize $T_z = T_{base}$, we can take advantage of the long lifetime of the cyclotron excitations. It will enable us to turn the FET on to determine whether an excitation has occurred after applying a drive with the transistor off.

To illustrate, we have obtained several cyclotron resonances for different "detector" conditions during the excitation: (i) axial drive and FET on, (ii) axial drive off and FET on, (iii) axial drive and FET off. As discussed above, the drive in the first scenario gives an increased broadening, in our case a resonance width of several hundred kHz (corresponding to several hundred kelvin in temperature). By turning off the axial drive during excitation, we obtain a resonance with a width corresponding to $T_z = 17 \pm 2$ K, which is consistent with values measured in past 4 K experiments [69]. The resonance exhibits qualitative features of the exponential limit; an example is shown in Fig. 5.4. This particular curve uses as an amplitude the number of jumps out of 100 excitation attempts.

When the FET and axial drive are both cycled off for the excitation (case (iii)), the axial temperature should reach the trap temperature. The resonance should have the same low-frequency edge but display a width 100 times more narrow and a correspondingly higher amplitude. Although some time was spent searching the frequencies around the abrupt edge in Fig. 5.4, no resonance was observed. The arrows in the figure show the range of frequencies searched (in roughly 500 Hz increments) with the FET off during excitation.

The transistor is biased through 1 sec filters, making the total time to cycle it off and on several seconds. This needs to be done each time a drive pulse is applied, and acquiring a resonance may require several hundred pulses. To obtain a resonance

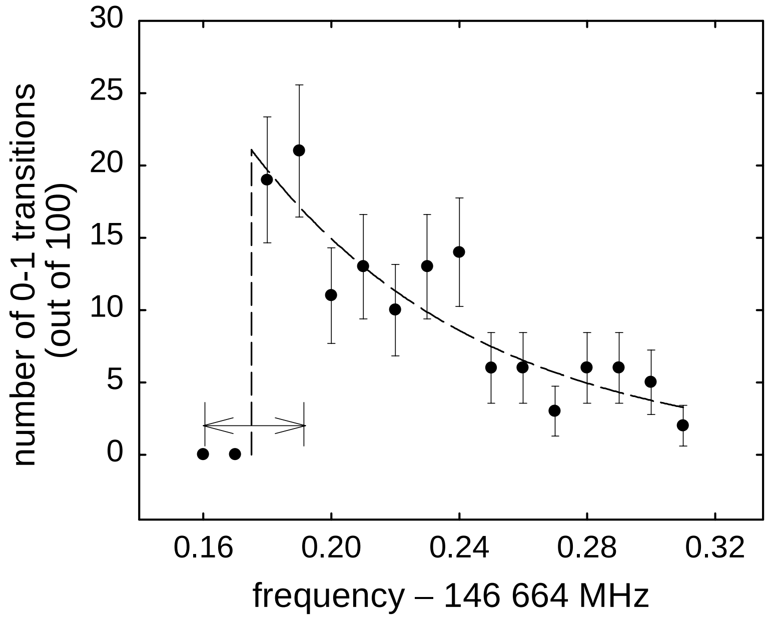

Figure 5.4: Single-electron cyclotron resonance. The exponential fit gives $T_z = 17 \pm 2$ K. The arrows mark the range of frequencies covered while searching for the resonance when both the FET and axial drive are turned off during excitation.

in an expedient fashion, we will ultimately need to optimize the excitation process by applying the drive for a duration that amounts to a pi pulse on resonance. This requires supplying enough drive power to give a Rabi frequency that is considerably larger than the decoherence rate of the oscillator. In the language of Rabi oscillations, the fluctuations in the resonant frequency introduced by the thermal axial motion must be slow compared to the rotation rate of the "state vector" from $n = 0$ to $n = 1$. This is relevant for all experiments manipulating Fock states of the cyclotron oscillator in a controllable fashion (recall Section 4.6).

5.1.3 Anomaly Resonance

The anomaly resonance will feature a different shape than the cyclotron resonance because $\Delta\omega_a \approx 10^{-3}\Delta\omega_c$ (recall Eq. (5.9) and Fig. 5.2(b)). Figure 5.5 shows the calculated line profile for the anomaly interval at 4.2 K and 50 mK. Also included on the plots are the Lorentzian (dashed lines) and exponential (dotted lines) limits at these temperatures. The line profile is indistinguishable from the Lorentzian limit at 50 mK, while it clearly lies between the two limits at 4.2 K.

Because the two-state spin system is involved in an anomaly transition, the resonance can be saturated for high drive powers or long drive-pulse lengths. The general expression for an anomaly resonance — the probability of a transition versus frequency — is not proportional to the line profile $\chi_a(\nu)$ for all drive strengths, but rather is given by [48]

$$P = \frac{1}{2}\left(1 - \exp\left(-\pi\Omega_a^2\, t\, \chi_a(\nu)\right)\right), \tag{5.16}$$

where Ω_a is the Rabi frequency and t is the length of time for which the drive is applied.

Figure 5.6 shows expected anomaly resonances for 4.2 K and 50 mK. On each plot are five curves for different values of V^2t (V is the drive voltage applied to the endcap electrode), with saturation clearly visible at the largest values. The advantage that the lower temperature affords is dramatic: the unsaturated resonance width is about 100 times more narrow at 50 mK, and the resonance peak is much higher for the same drive parameters. Notice that the peak for $V^2t = 1$ at 50 mK is about as high as the peak for $V^2t = 10^3$ at 4 K. This is fortunate since the milliwatts of anomaly-drive power used in the past to induce transitions at 4 K would be unbearable in a dilution-refrigerator environment. The $V^2t = 1$ curve in

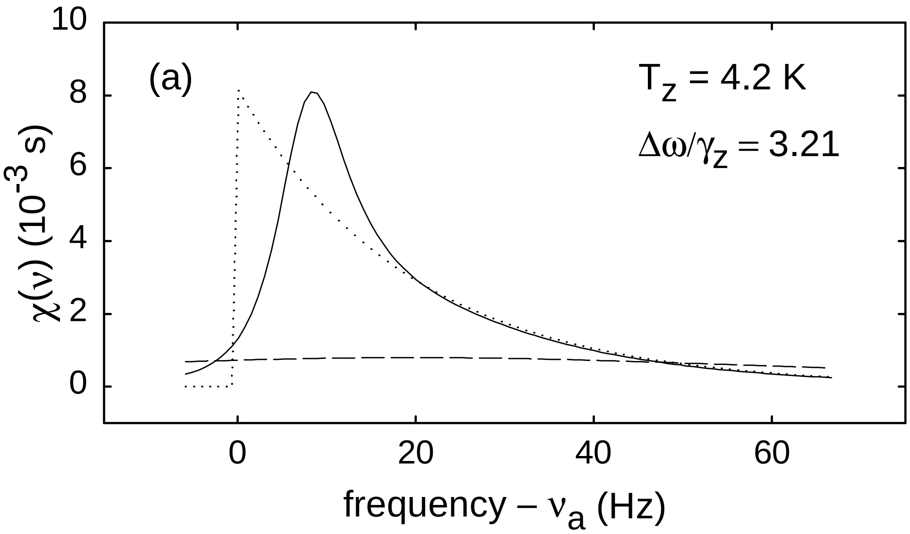

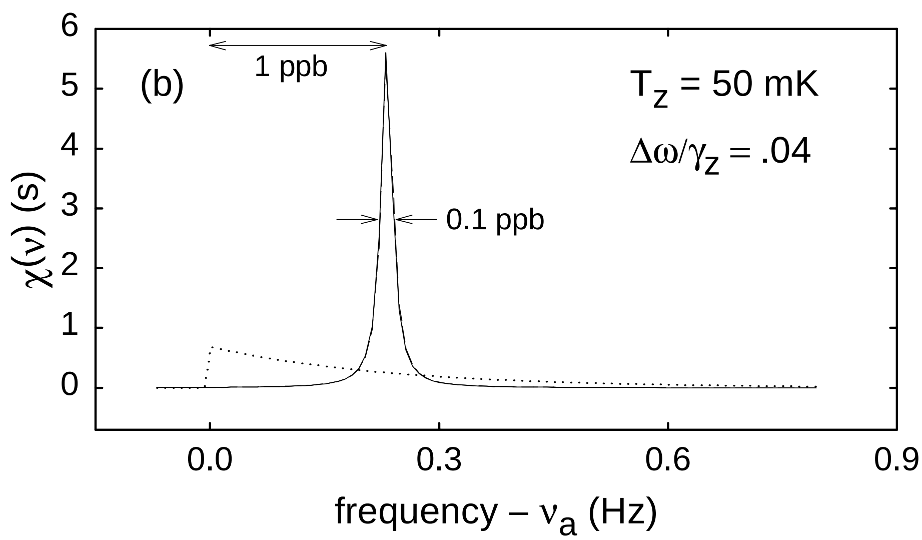

Figure 5.5: Calculated anomaly line profiles for (a) 4.2 K and (b) 50 mK, from expression (5.14). The dotted lines show the exponential limit and dashed lines the Lorentzian limit, which is indistinguishable from the actual line profile at 50 mK.

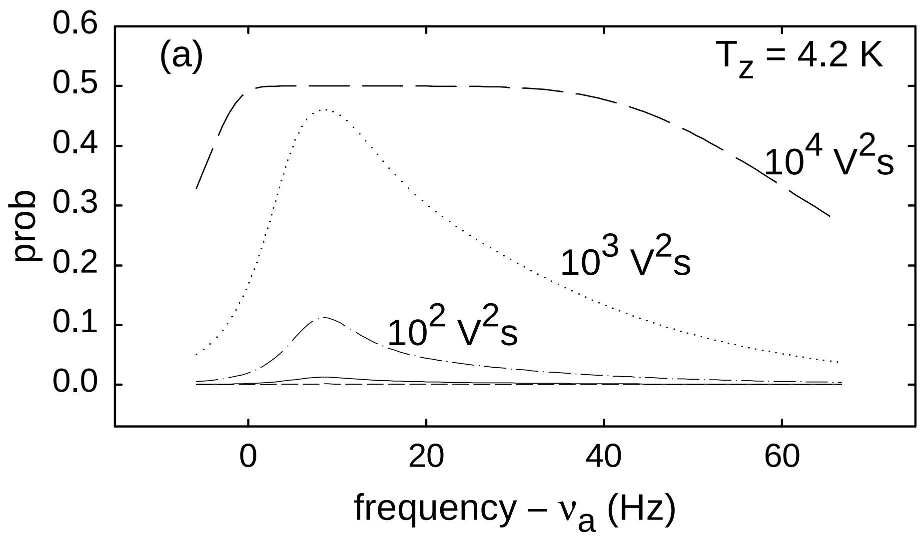

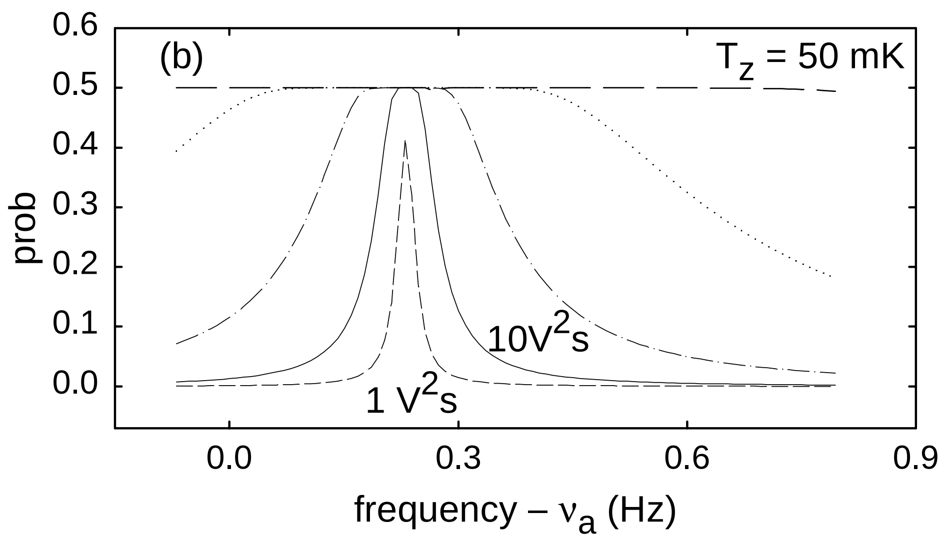

Figure 5.6: Calculated anomaly resonances for (a) 4.2 K and (b) 50 mK, from expression (5.16). Five curves are plotted, corresponding to $V^2t = 1$ (small dash), 10, 10^2, 10^3, and 10^4 (big dash), from bottom curve to top. The "high-energy" curves are clearly saturated.

Fig. 5.6(b) demonstrates that we should be able to achieve an anomaly resonance with a width of less than 0.1 ppb and a center shifted by about 1 ppb. Modest line splitting should yield a measurement of ν_a to our desired precision.

Driving the anomaly transition has been done with two different schemes in the past. One uses trap electrodes configured as coils with counter-circulating currents to create a radial magnetic field at ν_a (ν_s in the electron's rest frame) to induce a spin-flip [51]. We plan to implement the original method of driving the transition using the motional field generated by the electron's driven axial oscillation through the nonuniform bottle field [115]. Recall from Eq. (4.2) that the added magnetic-field gradient has a radial component, $B_2 z\rho$ (which vanished when calculating $\boldsymbol{\mu}\cdot\boldsymbol{B}$). This is seen by the electron as a field rotating at ν_c. When the axial motion is driven at $\nu_d \approx \nu_a$, this field is amplitude modulated and can stimulate a spin flip.

Our freedom to use a large bottle makes this technique convenient and more effective than previously possible because the Rabi frequency for the transition is proportional to B_2 [51],

$$\Omega_a = B_2 z_a \rho_c \frac{\mu_B}{\hbar}. \tag{5.17}$$

Here ρ_c is the radius of the cyclotron orbit and z_a is the 170 MHz oscillation amplitude that results from a drive voltage V,

$$z_a = \left(\frac{\omega_z^4}{\left(\omega_a^2 - \omega_z^2\right)^2 + \omega_a^2 \gamma_z^2} \right)^{\frac{1}{2}} \frac{d^2}{z_0} \frac{c_1}{2\left(1 + C_2\right)} \frac{V}{V_0}. \tag{5.18}$$

Our large bottle enables us to use a smaller z_a than otherwise possible. A large anomaly drive has been a systematic problem[2] for one of the other g-factor experiments [116], and is being addressed by increasing ρ_c during an anomaly excitation.

[2]For the same reason as discussed with the axial drive in Section 5.1; in effect, the drive raises the axial temperature. But the anomaly drive cannot be turned off during an anomaly excitation.

Because a spin flip is a magnetic dipole transition and because we drive the axial motion far from resonance ($\nu_a \approx 3\nu_z$), we need substantial RF power to induce an anomaly transition. Figure 5.6 shows that at 4.2 K, a 10 sec pulse must be as strong as 10 V at 170 MHz to achieve a transition probability approaching 0.5. Even the lower anomaly power needed at 50 mK is on the threshold of heating the trap environment. While most of our radio-frequency drives are applied with a constantan twisted pair with about 20 dB of attenuation at 50 MHz, we use a stainless-steel microcoax for application of the anomaly drive to transmit sufficient power to the trap.

5.2 Reduced Cyclotron Temperature

Acquiring a cyclotron resonance using just excitations from $n = 0$ to $n = 1$ avoids broadening due to relativistic anharmonicity. At 4 K, there is on average one thermal excitation to $n = 1$ every minute. This adds noise to the cyclotron resonance, which is eliminated at base temperature (around 80 mK) where the oscillator occupies the ground state 99.998% of the time (recall Section 2.2.2 and Fig. 4.14).

Blackbody radiation at 4 K complicates a different technique used to measure the cyclotron frequency. If no magnetic bottle is implemented, a cyclotron excitation can be "pulled" [88] to high enough n levels that the excitation can be observed with just the weak relativistic coupling between the cyclotron and axial motions. The center of the cyclotron lineshape in this case can be shifted by thermal excitations of the oscillator [116].

5.3 Eliminating Cavity Shifts

The cyclotron frequency of an electron in a Penning trap can be shifted from its free-space value due to the presence of the trap electrodes. The cavity walls formed by the electrodes impose boundary conditions on the radiation field inside the trap — the modified radiative properties of a confined electron accompany a shift in its oscillation frequency. The frequency shift is greater when near a cavity mode that when far detuned. This interaction between the electron and the enhanced radiation field of the trap is a specific example of the absorption (modified damping) and dispersion (frequency shift) that arise in a system of coupled oscillators.

The estimation of this cavity shift is the leading contribution to the uncertainty in the 1987 g-factor measurement, which was carried out in a hyperbolic Penning trap [31]. That trap design has a mode structure which is difficult to characterize. New g-factor measurements are presently being performed in hyperbolic traps by two teams from the original University of Washington collaboration. One strategy being used to eliminate the cavity shift is to manufacture the electrodes out of lossy material, making the Q values very low and thus approximating free space [117]. The other method being pursued is to measure ν_c versus number of particles N, since the cavity shift should scale with N [118].

Our strategy for dealing with this systematic is to use a cylindrical trap geometry which has a mode spectrum that is well understood and experimentally verifiable. The trap is machined and assembled so that there is little leakage at frequencies near 150 GHz. Choke flanges are incorporated to reflect radiation at the gaps between electrodes. The cavity modes have high quality factors of 10^4 [40] and are well separated in frequency, providing broad portions of spectrum at which coupling to the trap is minimal (recall Fig. 4.11). Previously, the measured resonant frequencies of the TE_{0np} modes were used to determine the dimensions of the cylindrical trap cavity, giving excellent agreement with the specified dimensions [40]. This is an indication that the radiation field inside the trap is well known, which is necessary for finding the magnetic field at which $\nu_c(\text{trap}) = \nu_c(\text{freespace})$ and determining the residual cavity shift.

As an example of how the cavity shift can be taken into account, Fig. 5.7 shows calculations of the modified damping rate and frequency shift experienced by an

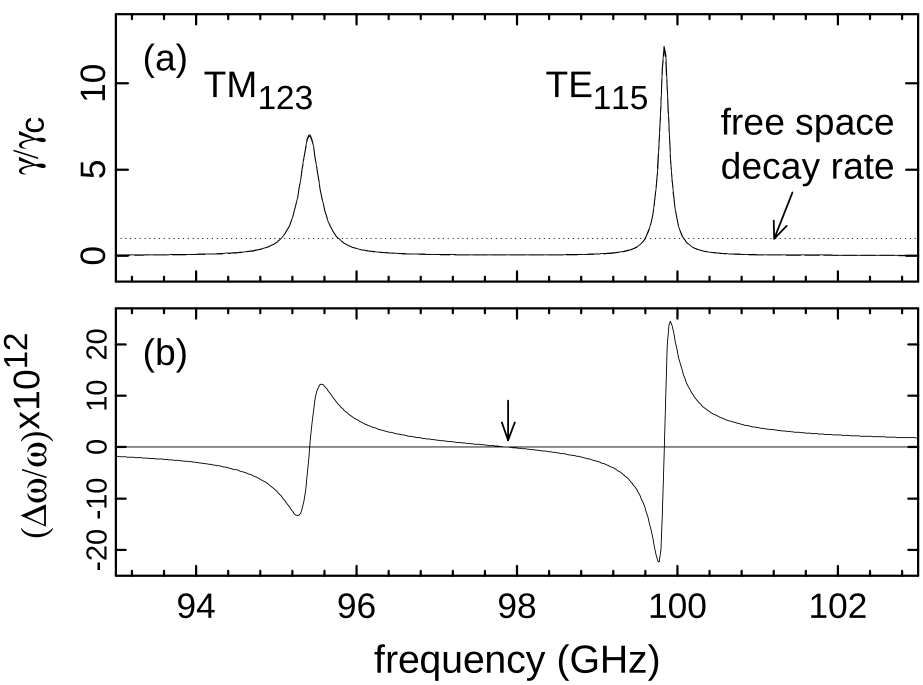

Figure 5.7: (a) Modified cyclotron damping rate versus frequency when coupled to two cavity modes observed in the cylindrical trap in reference [40]. (b) Accompanying frequency shift in the electron's cyclotron motion. This figure is adapted from reference [119], courtesy of J. N. Tan.

electron when coupled to the TM_{123} and TE_{115} modes of the trap, which were observed and identified in reference [119]. A particular mode will cause a shift in ν_c

with a dispersive shape, as illustrated in Fig. 5.7(b). Between neighboring modes, the frequency shift from each will be of opposite sign, making the net shift zero at some frequency, located in Fig. 5.7(b) with an arrow.

Our cyclotron oscillator, with its spontaneous emission dramatically suppressed, is weakly coupled to the trap and should have a correspondingly small shift in its frequency. While detuning the cyclotron motion from the electromagnetic modes of the trap diminishes the cavity shift, the weakly coupled oscillator becomes difficult to excite with an external microwave drive. This difficulty is partly offset by the increased lifetime, which essentially amplifies an excitation by making it long-lived. To first order, the cavity has no effect on the microwave power needed to make an excitation since the drive attenuation and the decreased radiation rate of the electron are both proportional to the amplitude of the radiation field at that frequency. However, this is relevant only for timescales long compared to the lifetime of the oscillator — coupling drive power to the electron on short timescales is more difficult when it is weakly coupled to the radiation field.

5.4 Future

The well-characterized modes of a cylindrical trap have been proposed as a way to sideband cool the axial motion of an electron by detuning $z(t)$ from its thermal reservoir and coupling it to the cyclotron motion with the appropriate drive field [40]. This is analogous to the process used to shrink the magnetron orbit, although the field needed to couple the axial and cyclotron motions is difficult to generate at the necessary power to achieve a reasonable cooling rate [48]. Tuning the system so that the sideband drive has a frequency that corresponds to a trap resonance of appropriate field geometry may allow enough power to be coupled to the electron for sideband cooling of the axial motion to become feasible. The theoretical cooling limit for this process is [48]

$$T_z = \frac{\omega_z}{\omega_c} T_c \tag{5.19}$$

(compare to Eq. 2.11), which would lower the axial temperature by 10^3. This could potentially be used to further reduce $\Delta\omega_c$ and $\Delta\omega_a$.

If future measurements push the g-factor precision much higher, the width of the cyclotron resonance may approach its natural linewidth (either by continuing with the magnetic bottle but achieving lower axial temperatures as discussed above or by eliminating the bottle and resorting to adiabatic-fast-passage techniques [88]). In this scenario, our demonstrated ability to narrow the natural linewidth by > 100 will be another feature of the cylindrical-cavity system that can be exploited.

Chapter 6

Conclusions

A cold electron cyclotron oscillator in a high-Q cylindrical trap cavity has been shown to be a useful system for generation of harmonic-oscillator Fock states. Detuning the oscillator from the resonant cavity modes of the trap increases its lifetime to 13 seconds, 140 times longer than in free space. Quantum jumps stimulated by thermal photons reveal the temperature of the electron's cyclotron motion and of the mode of the radiation field, demonstrating thermal equilibrium for timescales much longer than τ_c. When driven by an external microwave source, the rate of quantum jumps from $n = 0$ to $n = 1$ provides a method of measuring the cyclotron frequency to high precision, eliminating shifts due to special relativity.

This work required the development of a low-temperature Penning trap, which has been used to cool electrons below 4 K for the first time, reaching temperatures almost one-hundred times lower than previous experiments. Below 100 mK, the cyclotron oscillator is completely cooled to its ground state. A low-power FET fabricated from a specially grown semiconductor heterostructure provides single-electron signals with excellent signal-to-noise while the trap remains at 80 mK. The low-temperature environment enables us to improve our sensitivity to cyclotron excitations tenfold and still reduce the harmful line broadening of the magnetic bottle compared to the past g-factor measurement [31].

This system has been designed for precision measurements with a single electron. A new g-factor measurement will improve the precision with which we can determine the fine structure constant and will ultimately improve tests of quantum electrodynamics. Our cylindrical trap cavity and low temperature will reduce the systematic uncertainties encountered in an earlier measurement. Nonetheless, challenges remain. In order to take advantage of the low-temperature environment, the magnetic field at the trap center needs to be very stable. There are concerns that the field fluctuations felt by an electron may be more severe in our dilution refrigerator apparatus than in a liquid-helium system. Additional cryogen reservoirs, higher boil-off, and a vibrant pump may make establishing a stable field at the trap center a significant challenge.

Generation of Fock states of arbitrary n is the first step toward an efficient measurement of ν_c for precision measurements. While we can afford the large magnetic bottle field that we have implemented, it may prove wise to reduce its size by as much as a factor of five (which would still give well-resolved Fock states), in order to increase the coherence time of the oscillator for coherent excitations. Intriguing possibilities for the future include examining the limit of our "measurement time" and possibly observing evidence of the zero-point energy of the cyclotron oscillator.

Appendix A

Electrostatics

A.1 Definitions and Conversions

Equations describing the electrostatics of a Penning trap are written in the literature [48, 49] in terms of the variables V_0 and V_c shown in Fig. A.1(a). Experimentally, the endcap electrodes are grounded and voltages V_R and V_{comp} are applied to the ring and compensation electrodes, as shown in Fig. A.1(b).

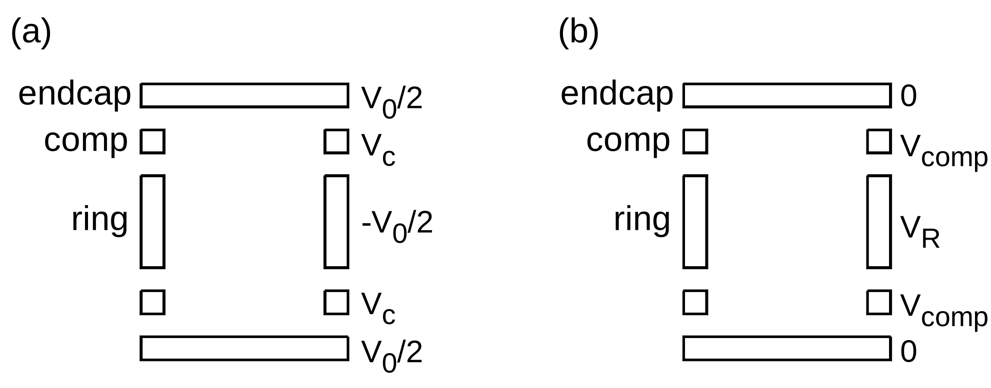

Figure A.1: Convention for voltages applied to Penning trap electrodes used (a) in the literature and (b) experimentally.

These two sets of variables can be related by adding a potential of $-V_0/2$ to all of the electrodes in Fig. A.1(a) and comparing the result to A.1(b). This gives

$$V_0 = -V_R, \tag{A.1}$$

$$V_c = V_{comp} - V_R/2. \tag{A.2}$$

A.2 Symmetric Potentials

Referring to Fig. A.1(a) above, the potential near the center of the trap due to V_0 can be expanded in powers of (r/d),

$$V = \frac{1}{2} V_0 \sum_{\substack{k=0 \\ \text{even}}}^{\infty} \left(\delta_{k2} + C_k^{(0)}\right) \left(\frac{r}{d}\right)^k P_k(\cos\theta). \tag{A.3}$$

Only even terms are included in the expansion because of invariance under $z \to -z$, and azimuthal symmetry removes all ϕ dependence. The expansion coefficients can be obtained by standard boundary-value methods [49],

$$C_k^{(0)} = -\delta_{k2} + \frac{(-1)^{\frac{k}{2}}}{k!} \frac{\pi^{k-1}}{2^{k-3}} \left(\frac{d}{z_0}\right)^k \sum_{\text{n}=0}^{\infty} \frac{(-1)^{n+1}(2n+1)^{k-1} \cos^2\left[\frac{1}{2}\left(n+\frac{1}{2}\right)\pi\Delta z_c/z_0\right]}{J_0\left[i\left(n+\frac{1}{2}\right)\pi\rho_0/z_0\right]}. \tag{A.4}$$

The potential at the center of the trap due to V_c can be expanded as

$$V = \frac{1}{2} V_c \sum_{\substack{k=0 \\ \text{even}}}^{\infty} D_k \left(\frac{r}{d}\right)^k P_k(\cos\theta), \tag{A.5}$$

with expansion coefficients [49]

$$D_k = \frac{(-1)^{\frac{k}{2}}}{k!} \frac{\pi^{k-1}}{2^{k-3}} \left(\frac{d}{z_0}\right)^k \sum_{\text{n}=0}^{\infty} \frac{(-1)^n (2n+1)^{k-1} 2\sin^2\left[\frac{1}{2}\left(n+\frac{1}{2}\right)\pi\Delta z_c/z_0\right]}{J_0\left[i\left(n+\frac{1}{2}\right)\pi\rho_0/z_0\right]}. \tag{A.6}$$

Combining Eqs. (A.3) and (A.5) gives the total potential,[1]

$$V = V_0 \left(\frac{z^2 - \rho^2/2}{2d^2} \right) + \frac{1}{2} V_0 \sum_{\substack{k=0 \\ \text{even}}}^{\infty} C_k \left(\frac{r}{d} \right)^k P_k(\cos\theta), \tag{A.7}$$

where

$$C_k = C_k^{(0)} + D_k \left(\frac{V_c}{V_0} \right), \tag{A.8}$$

and we have written out the delta-function term. It is useful to recast Eq. (A.8) in terms of V_R and V_{comp} using Eqs. (A.1) and (A.2),

$$C_k = C_k^{(0)} + D_k \left(\frac{1}{2} - \frac{V_{comp}}{V_R} \right). \tag{A.9}$$

For appropriate choice of trap dimensions, D_2 can be made to be almost zero, so that changes in the compensation voltage have very little effect on the axial oscillation frequency. In that case, the trap is said to be *orthogonalized*.

A.3 Antisymmetric Potentials

The potential near the trap center due opposite voltages applied to the endcaps as in Fig. A.2 can be expanded as

$$V = \frac{1}{2} V_A \sum_{\substack{k=1 \\ \text{odd}}}^{\infty} c_k \left(\frac{r}{z_0} \right)^k P_k(\cos\theta), \tag{A.10}$$

with expansion coefficients [49]

$$c_k = \delta_{k1} + \frac{2\pi^{k-1}(-1)^{(k-1)/2}}{k!} \sum_{n=1}^{\infty} \frac{(-1)^n n^{k-1}}{J_0(in\pi\rho_0/z_0)}. \tag{A.11}$$

[1] This equation uses both the cylindrical coordinate ρ and the spherical coordinate r.

For an antisymmetric potential applied to the compensation electrodes, Fig. A.3,

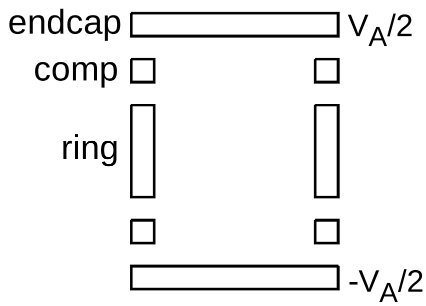

Figure A.2: Potential antisymmetric in z applied to the endcap electrodes.

the potential felt by a trapped particle is

$$V = \frac{1}{2} V_{A,c} \sum_{\substack{k=1 \\ \text{odd}}}^{\infty} d_k \left(\frac{r}{z_0} \right)^k P_k(\cos\theta), \tag{A.12}$$

with expansion coefficients

$$d_k = \frac{2\pi^{k-1}(-1)^{(k-1)/2}}{k!} \sum_{n=1}^{\infty} \frac{(-1)^n n^{k-1} \left(\cos\left(n\pi\Delta z_c/z_0\right) - 1\right)}{J_0\left(in\pi\rho_0/z_0\right)}. \tag{A.13}$$

The expansion coefficients c_k are needed for mapping out magnetic-field gradients (Section 4.1.1 and Appendix D), which requires application of voltages as shown in Fig. A.2 to axially displace the trapped particles. Determining the effects of a drive applied to or a detection circuit connected to an endcap electrode also requires knowledge of these coefficients [49, 120]. If detection or excitation incorporates a compensation electrode rather than an endcap (as in the case of our axial drives), the coefficients d_k are needed.

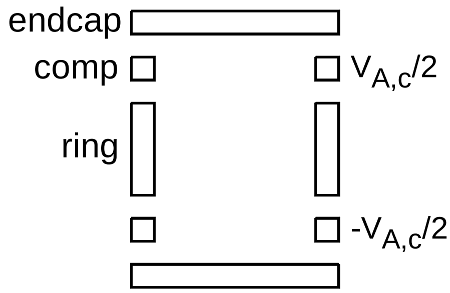

Figure A.3: Potential antisymmetric in z applied to the compensation electrodes.

A.4 Calculated Coefficients

The first two expansion coefficients for the four sets discussed, (A.4), (A.6), (A.11), and (A.13), have been calculated for our trap and compiled into Table A.1.

coefficient	**calc. value**
$C_2^{(0)}$	0.125
$C_4^{(0)}$	-0.018
D_2	4.4×10^{-5}
D_4	-0.055
c_1	0.785
c_3	0.318
d_1	0.031
d_3	-0.032

Table A.1: Electrostatic expansion coefficients.

Appendix B

Parametric Response with Weak Radiative Damping

Parametric excitations of electron oscillators have been useful for identifying the cavity modes of a cylindrical Penning trap [40, 50], demonstrating a 1-bit memory for "dark detection" [52], and studying stochastic switching in a two-well system [71]. The response to a parametric drive is well understood [50] when the electron cloud is strongly coupled to a cavity mode. The response in the case of weak radiative damping has been investigated less thoroughly.

With our magnetic field tuned so that electrons are decoupled from the trap's cavity modes, we have observed some unique behavior of a parametrically driven cloud of electrons. For a cloud size of 1,300 particles, the parametric resonance is observed to be symmetric; it is shown in Fig. B.1 along with the standard coherent axial response. For a 15-electron cloud, a stable excitation could not be sustained. An example of the response seen is shown in Fig. B.2,[1] but the lineshape varied from trace to trace. Figure B.3 shows the unstable behavior observed when the

[1] This moderately resembles the shapes seen when on the pedestal of a cavity mode [71].

15-electron cloud is parametrically driven on resonance and above threshold. The cloud's response at $\nu_d/2$ is mixed to 90 kHz and measured with an FFT signal analyzer. The figure shows sequential 50 Hz wide traces downloaded 0.8 sec apart, so that an interval of 24 sec is shown.

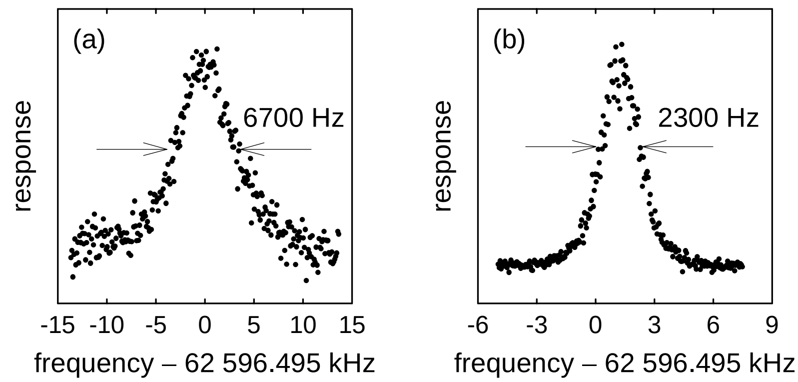

Figure B.1: (a) Standard driven axial response and (b) parametric response for a cloud of more than 1,000 electrons.

These parametric signals suggest a potentially useful method for studying phase transitions in a cold electron cloud. At very low temperatures, the thermal energy in a one-component plasma can be dominated by the Coulomb interaction between particles, resulting in a phase transition to a crystal-like structure. For an infinite plasma, this transition should occur when the Coulomb coupling constant,

$$\Gamma \equiv \frac{1}{4\pi\epsilon_0}\frac{e^2}{a_{WS}k_BT}, \tag{B.1}$$

is about 170 [121, 122, 123]. The Wigner-Seitz radius a_{WS} is the average distance between particles,

$$\frac{4\pi}{3}a_{WS}^3 = \frac{1}{n_0}, \tag{B.2}$$

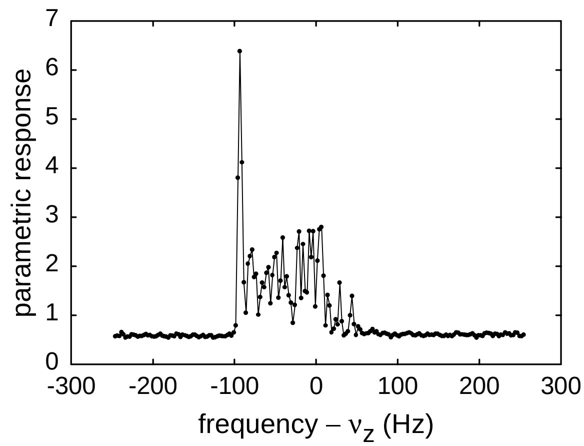

Figure B.2: Example of the parametric response of a 15-electron cloud with weak radiative damping.

with particle density

$$n_0 = \frac{3\epsilon_0}{ed^2} V_0 \tag{B.3}$$

for our system. Short-range order marked by a liquid-like state should arise at $\Gamma \approx 2$ [121]; thus, there is a large range of temperatures over which the cloud should behave differently than the "gaseous" state. Crystal structure has been seen in laser-cooled ion systems [41, 42, 43, 44].

Both coherent response to a parametric drive and short- and long-range order rely on cooled internal motions of the electron cloud. The parametric response of a cloud with a high degree of internal order should be similar to what would be seen if a "gaseous" cloud were coupled to a high-Q mode that could efficiently cool the internal motions. Studying parametric excitation of electrons with weak radiative damping could provide a very sensitive probe of the transition from disordered to ordered behavior by removing the "cooling effect" of the cavity modes. As the temperature is reduced, we might expect the unique behavior discussed here for

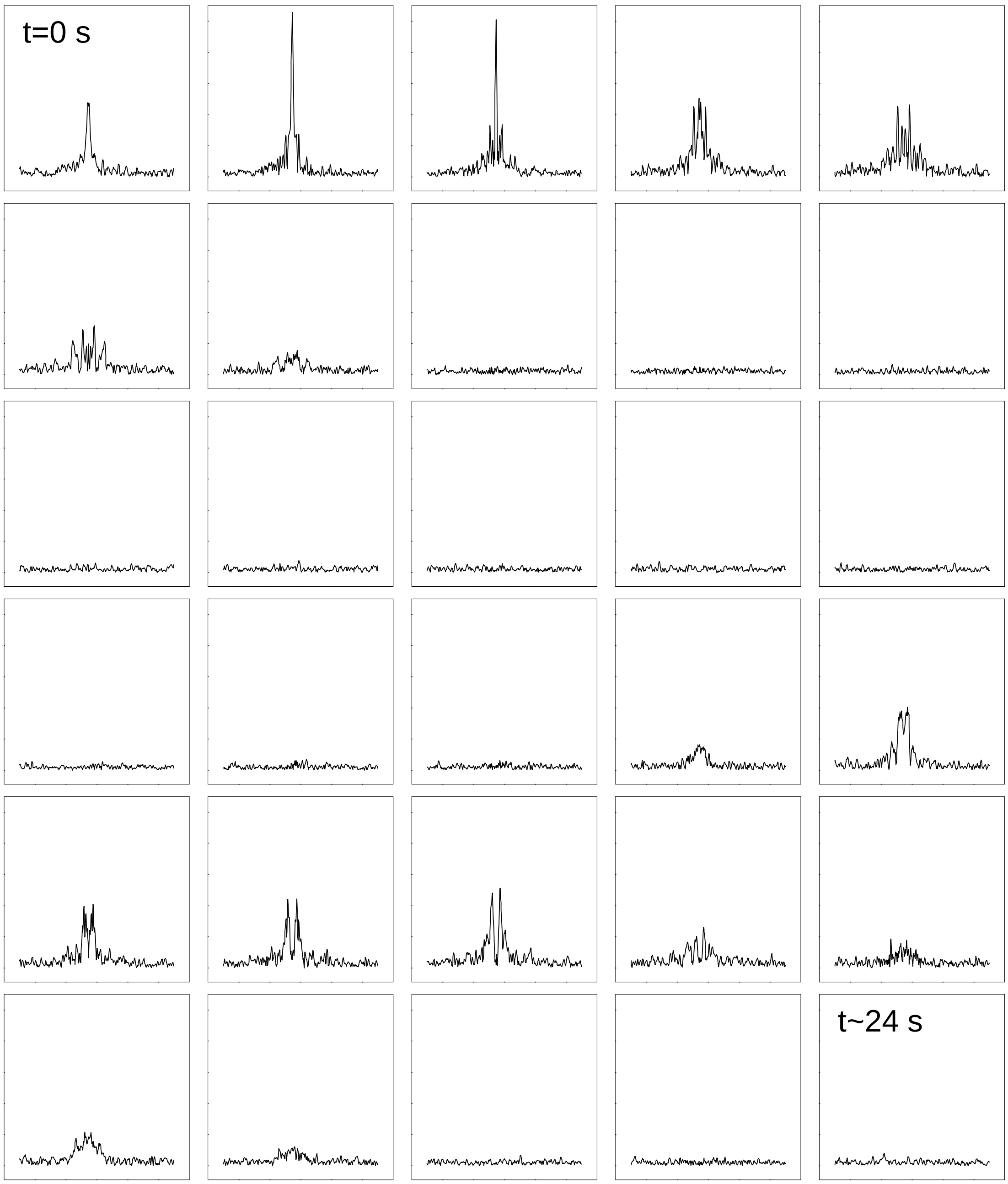

Figure B.3: Successive traces of the 15-electron cloud's response to a resonant parametric drive.

small Γ, approaching the behavior typically seen on a cavity mode and ultimately saturating when maximum order — crystallization — is achieved.

Figure B.4 shows the Coulomb coupling constant for an electron cloud in our experiment versus temperature. The onset of short-range order should occur just below 1 K; at 50 mK, an electron cloud is well into the "liquid" regime. In order to induce a transition to a crystal state, some additional cooling techniques would need to be applied to the cloud[2] to reach temperatures below 10 mK. Alternatively, a stronger trapping potential would increase the density and enable crystallization to occur at a higher temperature. A curve corresponding to $V_0 = 100$ V has been included in Fig. B.4. In that case, crystallization should occur between 10 and 20 mK, a temperature that may be achievable in our system with some improvements.

[2]For example, in Section 5.4 the possibility of reducing T_z several orders of magnitude by sideband cooling the axial motion is discussed.

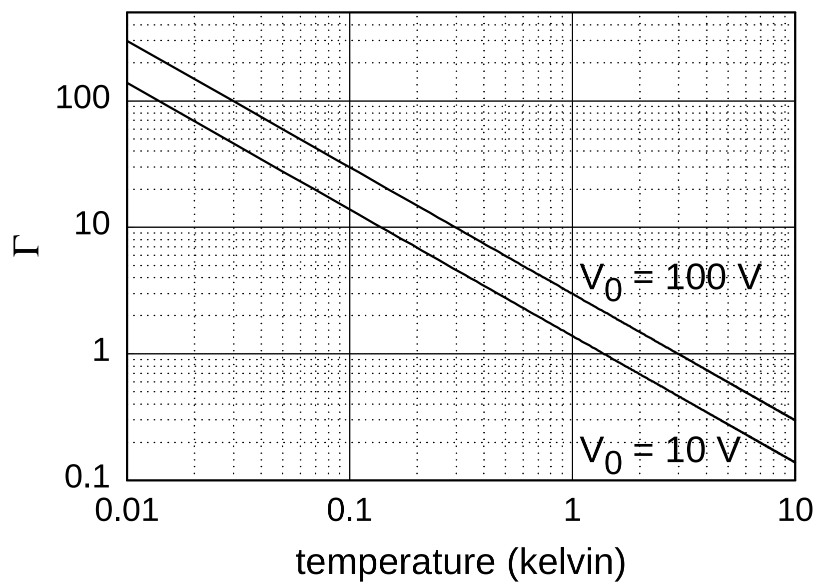

Figure B.4: Coulomb coupling constant Γ versus temperature for $V_0 = 10$ V and $V_0 = 100$ V.

Appendix C

Dilution-Refrigerator Details

C.1 Performance Issues

Three common problems that can hurt the performance of a dilution refrigerator are a leak, a touch between components at different temperatures, and a "plug" in the condenser line. We have had the opportunity to experience all three.

C.1.1 Vacuum Leaks

The dilution unit of a refrigerator is maintained in a vacuum region, the "inner vacuum chamber" or IVC, for thermal isolation of its various components. A leak into this vacuum space from the liquid-helium bath can be cryopumped by the refrigerator surfaces at $T < 4.2$ K until these surfaces saturate. A charcoal sorption pump (sorb), which is often used to remove the exchange gas efficiently, can dramatically increase the surface area available to cryopump ^{4}He and thus increase the time that the refrigerator can operate in the presence of a leak.

A chronic leak existed in the grease seal of our IVC for some time. It manifested itself when the refrigerator was submerged in liquid helium as a leak rate of $L \sim$

3×10^{-6} (mbar·l)/sec (Table C.1), but was unobservable at room temperature. This caused us to run on four-day cycles, after which the refrigerator surfaces would saturate with helium and the system would abruptly warm-up. Figure C.1 shows the helium level measured at the IVC pumping port near the end of one of these four-day periods. At some point (around 72 hours for this run), the helium entering the IVC through the leak can no longer be cryopumped and thus occupies the vacuum space as a vapor. This helium acts as an exchange gas, coupling heat between different stages of the refrigerator. Figure C.2 shows that the "hot" part of the two-piece amplifier, residing in the base-temperature region but heatsunk to the still (Fig. 3.4), cools as the exchange gas couples heat from it to the mixing chamber and experiment, which in turn warm.

Ultimately, this leak was fixed ($L \sim 4 \times 10^{-8}$ (mbar·l)/sec in liquid helium) by choosing an orientation of the refrigerator and IVC shield which increased the overlap between the two lapped surfaces.[1] This allowed us to run for several months with no signs of helium gas accumulating in the vacuum space.

leak rate	**run time**
3×10^{-6} mbar l/sec	4 days (no sorb)
	$>$ 12 days (sorb)
4×10^{-8} mbar l/sec	$>$ 9.5 weeks

Table C.1: IVC leak rates measured with the leak checker behind a turbo pump (80 l/sec nominal pumping speed), in parallel with the forepump. For the second two "run times" listed, the runs ended before any helium was seen to accumulate in the vacuum space. (Caution needs to be taken when establishing the leak rate. If a significant amount of helium has been pumped out of the IVC with the turbo-pump system, then the oil in the forepump can be saturated with helium and cause the measured leak rate to be artificially high. The oil can be purged in most cases by opening the gas ballast for several minutes.)

[1] Any new orientation of the IVC shield requires shimming the dilution unit of the refrigerator so there will be no contact between the two. This re-orientation, therefore, is not a trivial procedure.

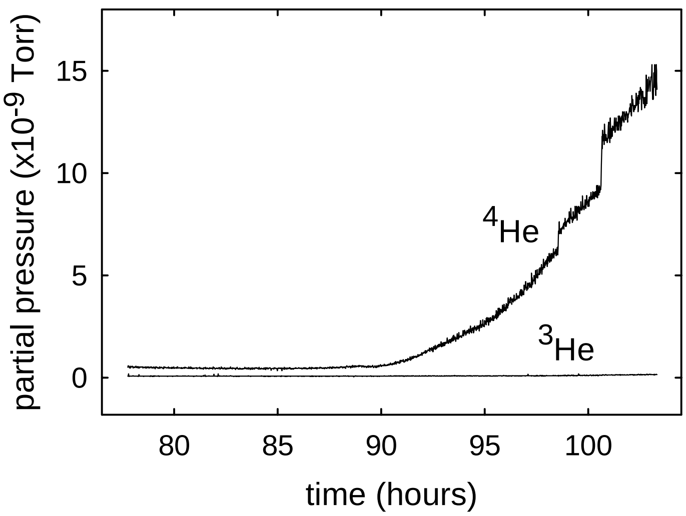

Figure C.1: Helium-4 level at the room-temperature IVC port as the system saturates after running for four days with a leak to the liquid-helium reservoir.

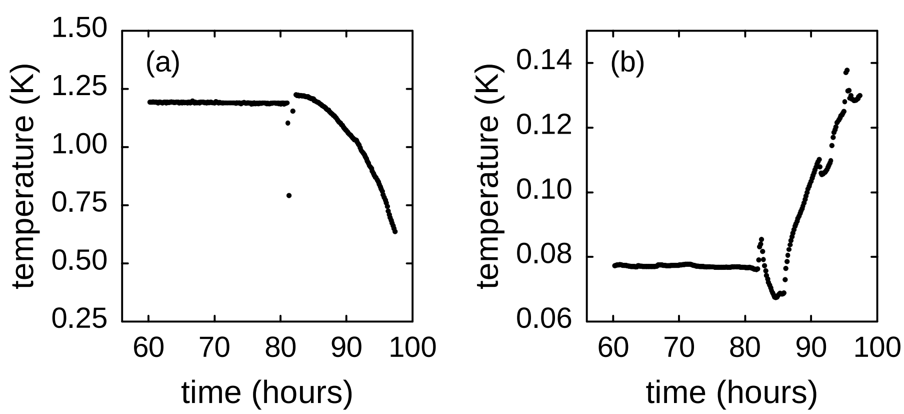

Figure C.2: When the surfaces in the refrigerator saturate due to a leak in the IVC, incoming helium cannot condense on the walls and thus acts like an exchange gas. This causes (a) the amplifier can to cool and (b) the trap to warm. (Figure C.1 is from a different run than this data.)

A leak between the IVC and dilution unit manifests itself differently than a leak between the IVC and liquid-helium reservoir. Figure C.3 shows the system's behavior in the presence of a dilution-unit leak. Several days into the run, two distinct peaks (or dips) appear in the system parameters, followed by an abrupt "crash". This behavior repeated itself during the following run, and may be evidence of what is called a "superleak". Tightening an indium seal at the still eliminated the problem.

C.1.2 Touch

We use an RF amplifier that couples the electron's signal from the trap electrode to the FET using two coaxial coils thermally anchored to separate stages of the refrigerator. This provides a physical break and enables heat generated by the FET to be directed to the still. To achieve a high coefficient of coupling (important both for signal size and amplifier stability), these coils must be close together. We originally had frequent touches between the two coils, resulting in cyclic fluctuations in the temperatures and pressures of the system. Figure C.4 shows the temperature of the amplifier can (the FET side of the amplifier) versus time, with the FET off. Our model for the cyclic behavior is that the still cools slightly because of contact with the mixing chamber, which hurts the cooling power and ultimately results in an overall temperature rise. This improves the cooling power, reducing the temperature, and the cycle repeats. The addition of a touch sensor for these coils enabled us to eliminate the problem; the two graphs in Fig. C.4 show the difference in behavior.

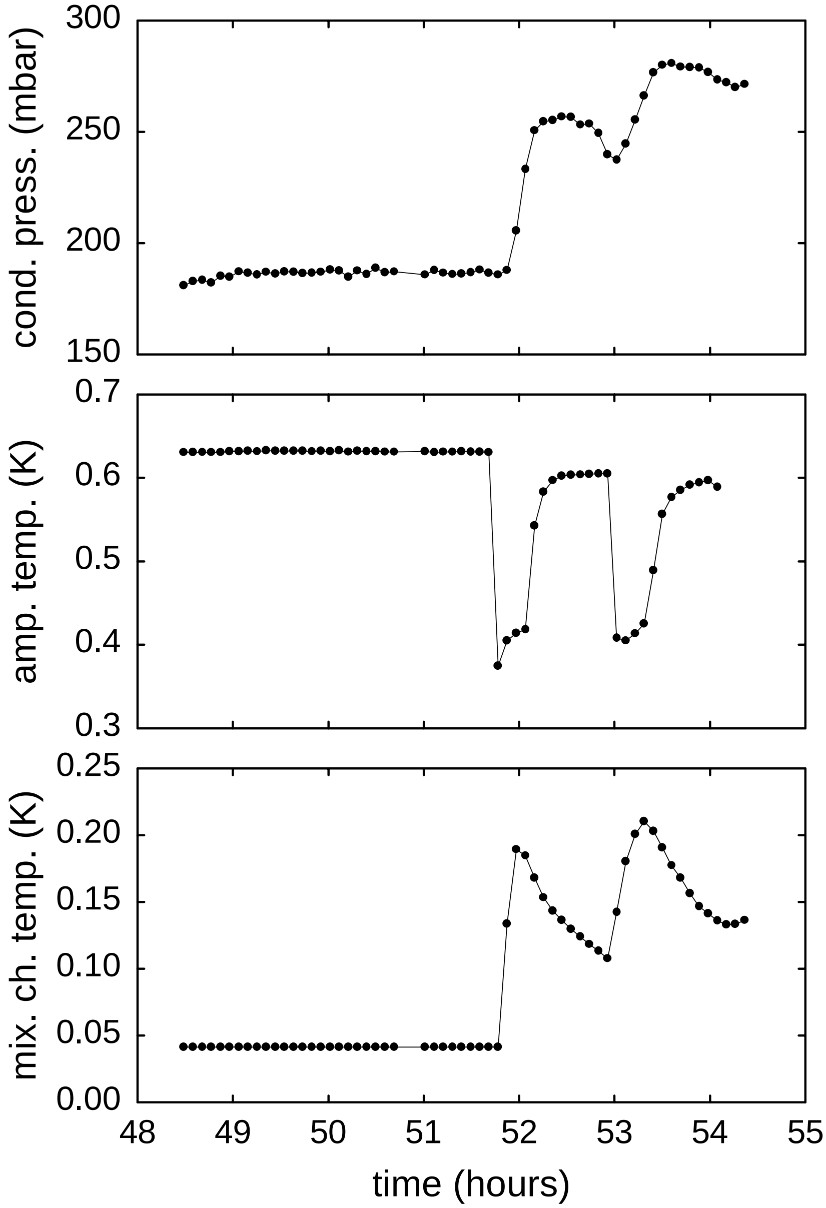

Figure C.3: Behavior of three refrigerator parameters when there is a leak in the dilution unit. The system crashed dramatically after the last data points shown here. Notice the individual peaks (or dips) versus the steady behavior when the leak is to the liquid helium reservoir, as in Fig. C.2.

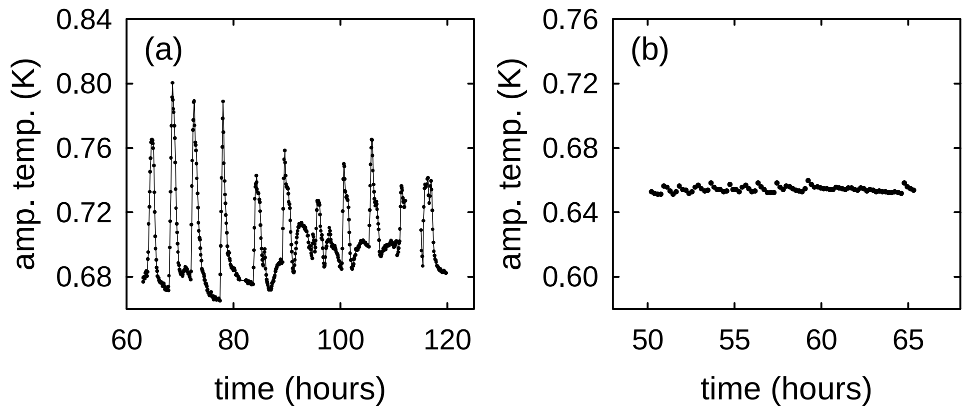

Figure C.4: Behavior of amplifier-can temperature (a) when there is a touch between the coils and (b) when the coils are not touching. The vertical spans are identical.

C.1.3 Plug

If the system's cold traps do not remove enough of the impurities introduced to the mash, or if there is a small leak in the system after these traps, contaminants can freeze at a point in the return line that impedes the ^{3}He circulation. This can continue for an extended period and hurt the system's performance, with the only reparation being to warm the refrigerator to room temperature and remove the impurities. We have had persistent problems with a condenser pressure that is higher than normal (typically several hundred millibar when *no* heat is applied to the still). Most likely, the plugs were caused by a major leak in the ^{3}He rotary pump, which introduced impurities faster than they could be removed by the cold traps.

C.2 Comparison to 4 Kelvin Systems

Experiments have been cooled to 4 K by both submersion in liquid helium and by thermal contact to a liquid-helium reservoir. The former "bucket dewar" experiments likely achieve better cooling, while the latter "cold-finger" systems feature more space for the trap and electronics, are less vulnerable to a leak in the trap can, and allow particle transport from below [124]. Figure C.5 shows the basic set-up of the two liquid-helium designs and the analogous components for the dilution-refrigerator system.

C.3 Operating Procedure

Since this is a unique apparatus — the first incorporation of a dilution refrigerator with a Penning trap — the operation procedures developed in the past several years are included here as an aid for subsequent users.

C.3.1 Cooling to 4 Kelvin

After final changes have been made to the experiment and all room-temperature electrical checks have been carried out…

1. Inspect for potential touches between inductive amplifier, base temperature components, and cold shield.

2. Put on cold shield and attach touch sensor.

3. Put on IVC shield, using A on shield opposite to A on refrigerator for alignment.

4. Check for leaks in the IVC.

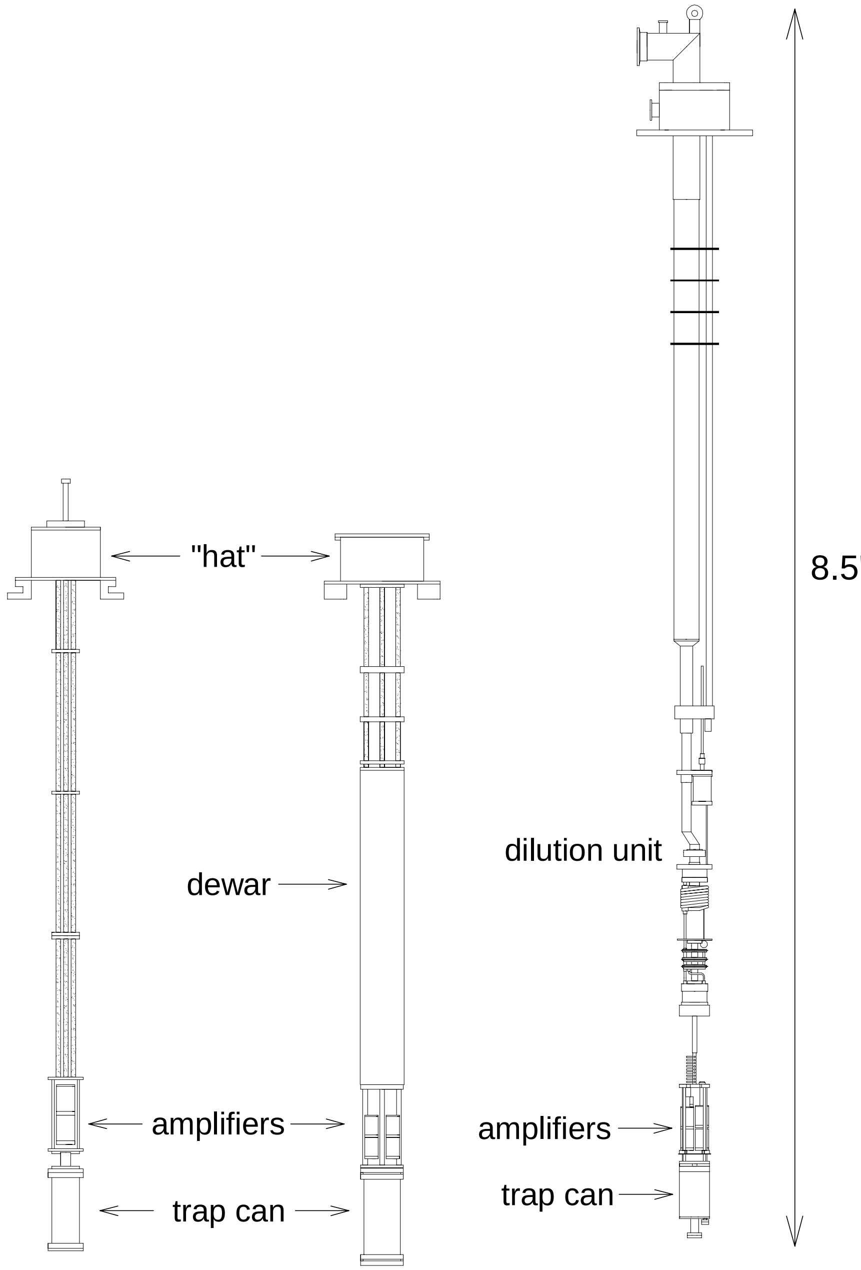

Figure C.5: Evolution of Penning-trap apparatus. (The systems are aligned according to the trap centers.)

5. Add about $\frac{2}{3}$ atm of nitrogen gas to serve as a "clamp" for the trap can while cooling. (Helium cannot be used at room temperature because it can diffuse through the glass-to-metal seal on the trap can.)

6. Remove liquid helium from the dewar, being mindful of the vacuum space.

7. Lower refrigerator into empty dewar (4.2 K $< T_{dewar} <$ 77 K). Going slowly (about a 30 minute descent) allows the glass-to-metal seals and other joints to cool gradually and is most gentle on the dewar. The refrigerator will cool to 77 K due to the gas in the dewar; the dewar remains cold because of the surrounding liquid nitrogen reservoirs.

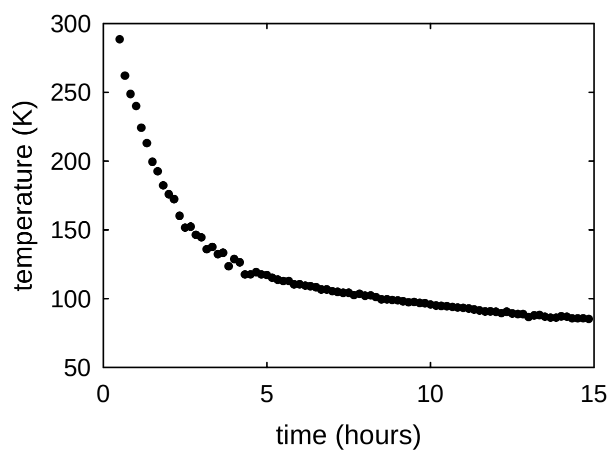

Figure C.6: Typical cooling curve for experiment when refrigerator resides in empty dewar near 77 K.

8. When the experiment has cooled to 77 K, pump the nitrogen from the IVC and replace with helium gas (about $\frac{1}{2}$ atm). Repeat all electrical checks.

9. Fill dewar with liquid helium. The experiment will cool quickly to 4 K.

10. In order to fire the field emission point to load electrons, most of the helium needs to be pumped from the IVC to avoid breakdown in the helium atmosphere. Enough gas must remain so that heat from the FET (if generating several milliwatts) is coupled to the liquid-helium bath. This typically takes about $1\frac{1}{2}$–3 hours of pumping with our 80 l/sec turbo pump.

11. Carry out experiments at 4 K.

C.3.2 Cooling Below 4 Kelvin

1. The remaining helium needs to be pumped out of the IVC. At this time, a leak-check of the vacuum space should be performed. The leak rate measured (refer to Table C.1) will indicate the quality of the seals and the expected duration of the refrigerator run.

2. The lines from the gas-handling system need to be attached to the refrigerator and the connections leak checked.

3. Mash should be cleaned for several hours, finishing close to the time when cooling is to begin.

4. Begin cooling by filling and pumping on the 1 K pot. The RGA, monitoring the IVC, should show a dramatic reduction in ^{4}He pressure at this point.

5. Condense the mash into the still. Guide the diffusion of the mash through the liquid nitrogen and helium traps and into the still, bypassing the condenser.

6. The entire condensation process takes several hours.

7. Establish continuous circulation by (gradually) pumping on the mash.

8. Remove the remaining mash from the dumps. During steps 5–8, always check that the 1 K pot remains cold and does not empty.

9. Apply several ($\sim$ 3–5) milliwatts of heat to the still to establish the optimal circulation rate. (This is sometimes abandoned if an abnormally high condenser pressure builds.)

10. From this point, base temperature may take 8–10 hours (see Fig. C.7).

11. Make sure that the needle valve is adjusted so that the 1 K pot remains as cold as possible, but does not empty.

C.3.3 Removal of Refrigerator from Dewar

1. Pump mash back into the dumps, performing "one-shot".

2. Stop pumping on 1 K pot and fill with liquid helium. Turn on heaters and pump on both sides of the dilution unit until all of the mash is removed.

3. Remove the liquid helium from the dewar, by transferring liquid out of the belly and using the 3 W sorb heater to empty the tail. Use temperature sensors to determine when the tail is empty. (The eddy currents induced in the refrigerator when it is lifted with liquid helium in the dewar make removal impractical; emptying the dewar first mitigates this effect.)

4. Manually remove refrigerator with the pulley, but have the chain hoist hooked up and continually take up the slack. When the apparatus is completely out of the dewar, suspend it from the chain hoist instead of the pulley. Blow helium gas through the dewar and use plastic bags around the refrigerator during this process to minimize the amount of air that gets into the dewar.

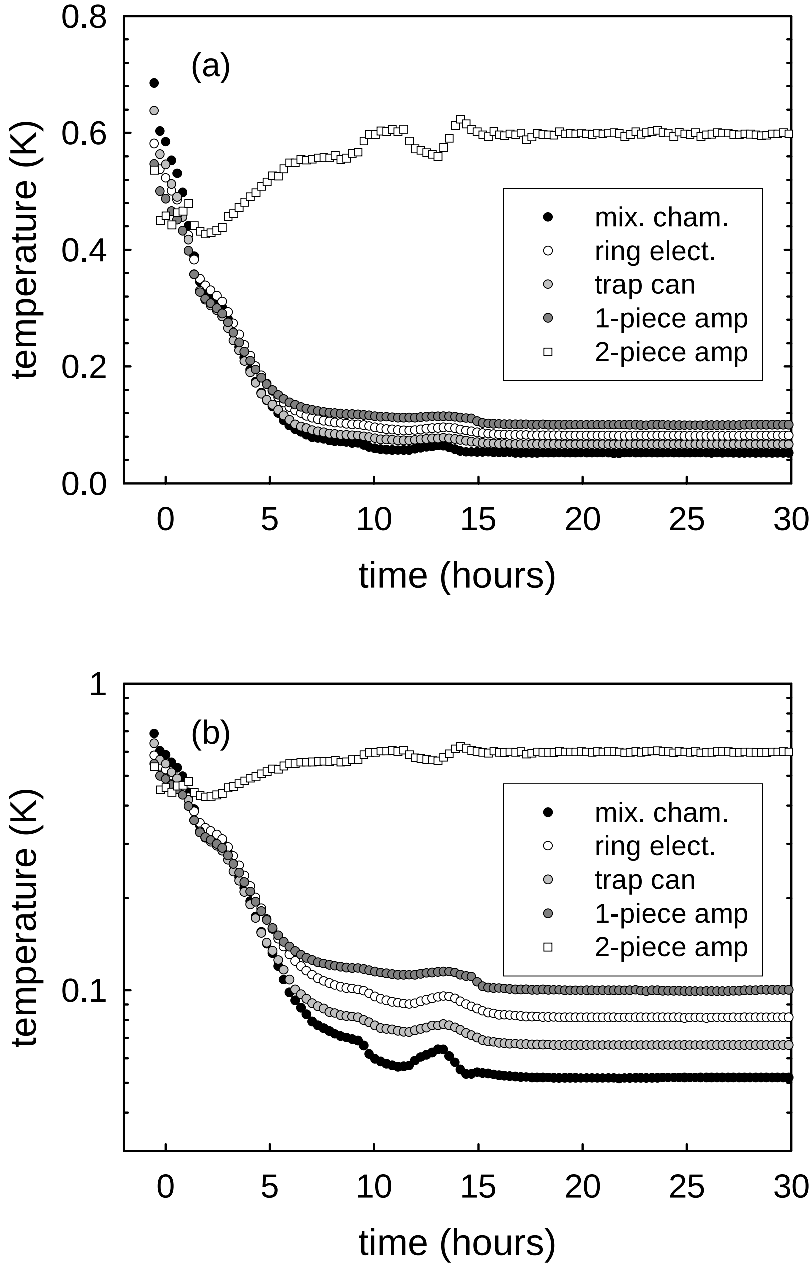

Figure C.7: Typical "cool down" of dilution refrigerator, (a) linear and (b) log scales.

5. Wait until the system warms to room temperature, about 2–3 hours, before removing the IVC shield. Vent the vacuum space with dry nitrogen gas. Use the "knocker" to remove the shield with the refrigerator stationed at an appropriate height.

Appendix D

Magnetic-Bottle Measurement in a Cylindrical Trap

D.1 Axial Displacement of Particles

Shifting the center of oscillation of an electron cloud is accomplished by applying a potential of V_A between the two endcaps as shown in Fig. A.2. Here we compile the expressions for the size of the axial displacement and the axial frequency shift versus V_A. These have been derived before [125], but are important to review because there have been several errors in the literature [125, 53].

The potential at the center of the trap due to the antisymmetric voltage applied to the endcaps can be expanded as (Eq. (A.10))

$$V = \frac{1}{2} V_A \sum_{\substack{k=1 \\ \text{odd}}}^{\infty} c_k \left(\frac{r}{z_0}\right)^k P_k(\cos\theta). \tag{D.1}$$

If we consider the particles to be on axis, the leading terms of this expansion are

$$V = \frac{V_A}{2}\left(c_1\left(\frac{z}{z_0}\right) + c_3\left(\frac{z}{z_0}\right)^3\right). \tag{D.2}$$

Adding the symmetric trapping potential (Eq. (A.7)) gives us the entire potential on axis near the center of the trap; to third order in z,

$$V(z) = \frac{V_0}{2}\left(1 + C_2^{(0)}\right)\left(\frac{z}{d}\right)^2 + \frac{V_c}{2}D_2\left(\frac{z}{d}\right)^2 + \frac{V_A}{2}\left(c_1\left(\frac{z}{z_0}\right) + c_3\left(\frac{z}{z_0}\right)^3\right). \tag{D.3}$$

The minimum of $V(z)$ will determine the shifted center of oscillation, z_e. To first order in this small displacement,

$$\left.\frac{\partial V}{\partial z}\right|_{z_e} = \frac{V_0}{d^2}z_e\left(1 + C_2^{(0)} + \frac{V_c}{V_0}D_2\right) + \frac{V_A}{2}\frac{c_1}{z_0} = 0. \tag{D.4}$$

This results in an equilibrium position of

$$\boxed{\frac{z_e}{z_0} \simeq -\frac{1}{2}\left(\frac{d}{z_0}\right)^2\left(\frac{V_A}{V_0}\right)c_1\frac{1}{1+C_2}} \tag{D.5}$$

where $C_2 = C_2^{(0)} + (V_c/V_0)\,D_2$.

To determine the shift in axial frequency versus displacement in the trap, we can expand the expression for $V(z)$ (Eq. (D.3)) in terms of $z = z_e + u$ [48],

$$\begin{aligned} V &= \frac{V_0}{2}(1+C_2)\left(\frac{z_e+u}{d}\right)^2 + \frac{V_A}{2}\left(c_1\left(\frac{z_e+u}{z_0}\right) + c_3\left(\frac{z_e+u}{z_0}\right)^3\right) \\ &= \frac{V_0}{2}\frac{(1+C_2)}{d^2}\left(1 + 3\frac{c_3}{(1+C_2)}\frac{z_e d^2}{z_0^3}\frac{V_A}{V_0}\right)u^2 + \text{const.} \end{aligned} \tag{D.6}$$

Terms linear in u have been discarded since we expect to still have harmonic motion at the new equilibrium position. Using $m\omega_z^2 u^2/2 = eV$ and expanding the square-root for small changes to ω_z gives

$$\boxed{\frac{\Delta\omega_z}{\omega_z} \simeq -\frac{3}{4}\left(\frac{d}{z_0}\right)^4 \frac{c_1 c_3}{(1+C_2)^2}\left(\frac{V_A}{V_0}\right)^2} \tag{D.7}$$

when we compare to $V\Big|_{V_A=0}$ and substitute for z_e. Figure D.1 shows the axial frequency shift introduced as a function of vertical displacement in the trap. The curvature of the plot is .0011 V^{-2}, giving a value for $c_1 c_3$ of 0.243, which agrees well with the product of the calculated values of $c_1 = 0.785$ and $c_3 = 0.318$ (see Appendix A).

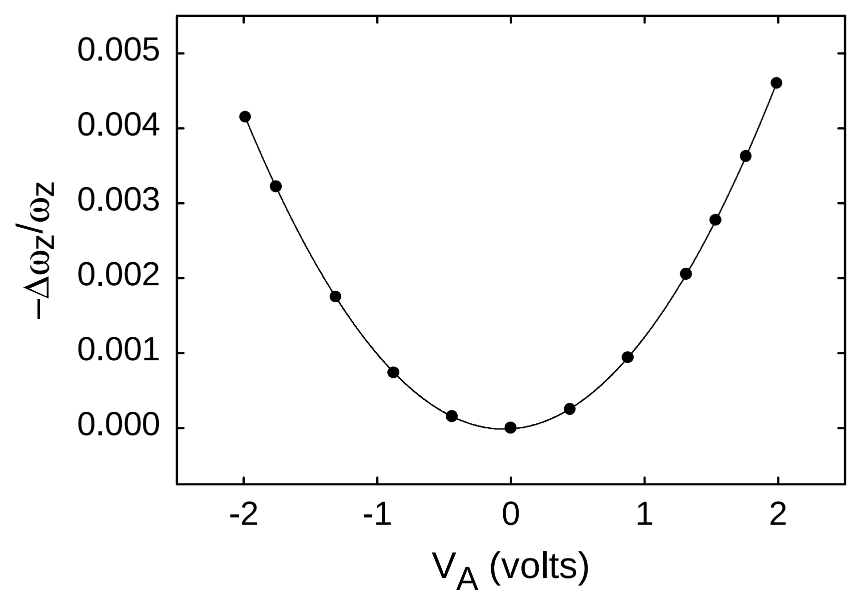

Figure D.1: Axial frequency shift versus V_A. From (D.7), the quadratic fit gives $c_1 c_3 = 0.243$. Electrons sit 7 microns away from the center of the trap when no V_A is applied.

D.2 Cyclotron Excitations

Exciting the cyclotron motion of a cloud of electrons is difficult when the system's resonant frequency is well detuned from the trap's cavity modes. While typically a large cloud provides a large cyclotron response because of the high degree of coupling between the motions of the particles, no cyclotron excitation has been observed for a cloud of *more* than ≈ 200 electrons at 146.7 GHz. This is apparently because it is so difficult to couple microwave radiation into the trap cavity at ν_c that the amount of power needed to excite a large cloud enough to be detected is more than our drive can generate. Thus, when off of a mode, it is necessary to carry out magnetic field measurements with a relatively small cloud.

Bibliography

[1] *Quantum Optics*, edited by D. F. Walls and G. J. Milburn (Springer-Verlag, New York, 1995).

[2] D. P. DiVincenzo, Science **270**, 255 (1995).

[3] S. J. van Enk, J. I. Cirac, and P. Zoller, Phys. Rev. Lett. **78**, 4293 (1997).

[4] S. Peil and G. Gabrielse, submitted to *Physical Review Letters*, March 1999.

[5] H. J. Charmichael and D. F. Walls, J. Phys. B **9**, 43 (1976).

[6] H. J. Kimbel, M. Dagenais, and L. Mandel, Phys. Rev. Lett. **39**, 691 (1977).

[7] H. J. Kimbel, M. Dagenais, and L. Mandel, Phys. Rev. A **18**, 201 (1978).

[8] F. M. Rateike, G. Leuchs, and H. Walther, in *Dissipative Systems in Quantum Optics*, edited by R. Bonifacio (Springer, New York, 1982).

[9] F. Diedrich and H. Walther, Phys. Rev. Lett. **58**, 203 (1987).

[10] R. E. Slusher, L. W. Hollberg, B. Yurke, J. C. Mertz, and J. F. Valley, Phys. Rev. Lett. **55**, 2409 (1985).

[11] L. A. Wu, H. J. Kimble, J. Hall, and H. Wu, Phys. Rev. Lett. **57**, 2520 (1986).

[12] D. M. Meekhof, C. Monroe, B. E. King, W. M. Itano, and D. J. Wineland, Phys. Rev. Lett. **76**, 1796 (1996).

[13] X. Maître, E. Hagley, G. Nogues, C. Wunderlich, P. Goy, M. Brune, J. M. Raimond, and S. Haroche, Phys. Rev. Lett. **79**, 769 (1997).

[14] M. Weidinger, B. T. H. Varcoe, R. Heerlein, and H. Walther, ICAP 16 Abstracts (1998).

[15] P. Domokos, M. Brune, J. M. Raimond, and S. Haroche, Eur. Phys. J. D **1**, 1 (1998).

[16] V. B. Braginsky and F. Ya. Khalili, Rev. Mod. Phys. **68**, 1 (1996).

[17] Hans Frauenfelder and Ernest M. Henley, *Subatomic Physics*, 2nd ed. (Prentice Hall, Englewood Cliffs, New Jersey, 1991).

[18] Frank Pobell, *Matter and Methods at Low Temperatures* (Springer-Verlag, New York, 1992).

[19] G. Frossati, in the monograph preprint *Experimental Techniques*.

[20] D. S. Betts, *Refrigeration and Thermometry Below One Kelvin* (Sussex University Press, Brighton, 1976).

[21] O. V. Lounasmaa, *Experimental Principles and Methods Below 1 K* (Academic Press, New York, 1974).

[22] Eric Cornell, J. Res. Natl. Inst. Stand. Technol. **101**, 419 (1996).

[23] K. B. Davis, M.-O. Mewes, M. R. Andrews, N. J. van Druten, D. S. Durfee, D .M. Kurn, and W. Ketterle, Phys. Rev. Lett. **75**, 3969 (1995).

[24] John M. Doyle, Bretislav Friedrich, Jinha Kim, and David Patterson, Phys. Rev. A **52**, 2515 (1995).

[25] Jinha Kim, Bretislav Friedrich, Daniel P. Katz, David Patterson, Jonathan D. Weinstein, and John M. Doyle, Phys. Rev. Lett. **78**, 3665 (1997).

[26] J. D. Weinstein, Robert deCarvalho, Jinha Kim, David Patterson, Bretislav Friedrich, and John M. Doyle, Phys. Rev. A **57**, 3173 (1998).

[27] Jonathan D. Weinstein, Robert deCarvalho, Thierry Guillet, Bretislav Friedrich, and John M. Doyle, Nature **395**, 148 (1998).

[28] W. Mampe, P. Ageron, C. Bates, J. M. Pendlebury, and A. Steyerl, Phys. Rev. Lett. **63**, 593 (1989).

[29] S. Peil, B. Odom, and G. Gabrielse, Bull. Am. Phys. Soc. **43**, 1272 (1998).

[30] S. Peil, R. G. Beck, R. M. Westervelt, and G. Gabrielse, to be submitted to *Reviews of Scientific Instruments*.

[31] Robert S. Van Dyck Jr., Paul B. Schwinberg, and Hans G. Dehmelt, Phys. Rev. Lett. **59**, 26 (1987).

[32] Toichiro Kinoshita, Rep. Prog. Phys. **59**, 1459 (1996).

[33] F. Minardi, G. Bianchini, P. Cancio Pastor, G. Giusfredi, F. S. Pavone, and M. Inguscio, Phys. Rev. Lett. **82**, 1112 (1999).

[34] D. S. Weiss, B. C. Young, and S. Chu, Phys. Rev. Lett. **70**, 2706 (1993).

[35] V. W. Hughes and T. Kinoshita, Rev. Mod. Phys. **71**, 133 (1999).

[36] Toichiro Kinoshita, private communication.

[37] W. Liu *et al.*, Phys. Rev. Lett. **82**, 711 (1999).

[38] E. R. Cohen and B .N. Taylor, Rev. Mod. Phys. **59**, 1121 (1987).

[39] G. Gabrielse, S. L. Rolston, L. Haarsma, and W. Kells, Phys. Lett. A **129**, 38 (1988).

[40] J. Tan and G. Gabrielse, Phys. Rev. Lett. **67**, 3090 (1991).

[41] F. Diedrich, E. Peik, J. Chen, W. Quint, and H. Walther, Phys. Rev. Lett. **59**, 2931 (1987).

[42] J. Hoffnagle, R. G. DeVoe, L. Reyna, and R. G. Brewer, Phys. Rev. Lett. **61**, 255 (1988).

[43] D. J. Wineland, J. Bergquist, W. Itano, J. Bollinger, and C. Manney, Phys. Rev. Lett. **59**, 2935 (1987).

[44] T. B. Mitchell, J. J. Bollinger, D. H. E. Dubin, X.-P. Huang, W. M. Itano, and R. H. Baughman, Science **282**, 1290 (1998).

[45] G. Graff, F. G. Major, R. W. H. Roeder, and G. Werth, Phys. Rev. Lett. **21**, 340 (1968).

[46] Dean L. Farnham, Jr. Robert S. Van Dyck, and Paul B. Schwinberg, Phys. Rev. Lett. **75**, 3598 (1995).

[47] Gerald Gabrielse and Hans Dehmelt, Phys. Rev. Lett. **55**, 67 (1985).

[48] L. S. Brown and G. Gabrielse, Rev. Mod. Phys. **58**, 233 (1986).

[49] Gerald Gabrielse and F. Colin MacKintosh, Int. J. of Mass Spec. and Ion Proc. **57**, 1 (1984).

[50] Joseph Ngai Tan, Ph.D. thesis, Harvard University, Cambridge, Massachusetts, 1992.

[51] Robert S. Van Dyck Jr., in *Quantum Electrodynamics*, edited by T. Kinoshita (World Scientific, New Jersey, 1990).

[52] C. H. Tseng, D. Enzer, G. Gabrielse, and F. L. Walls, Phys. Rev. A **59**, 2094 (1999).

[53] Ching-Hua Tseng, Ph.D. thesis, Harvard University, Cambridge, Massachusetts, 1995.

[54] Larson Electronic Glass, Redwood City, California 94064.

[55] D. E. McCarthy, Appl. Opt. **10**, 2539 (1971).

[56] The Eppley Laboratory, Inc., Newport, Rhode Island 02840.

[57] David Sumner Hall, Ph.D. thesis, Harvard University, Cambridge, Massachusetts, 1997.

[58] Type MKP 1840. Roederstein, Landshut, Germany.

[59] *Experimental Techniques in Condensed Matter Physics at Low Temperatures*, edited by Robert C. Richardson and Eric N. Smith (Addison-Wesley, Reading, Massachusetts, 1988).

[60] Emerson & Cuming, Inc., Woburn, Massachusetts 01888.

[61] *The ARRL Handbook for the Radio Amateur*, 67th ed., edited by Kirk A. Kleinschmidt (American Radio Relay League, Newington, Connecticut, 1990).

[62] Dale Electronics, Inc., Columbus, Nebraska 68601.

[63] RV-Elektroniikka Oy, SF-01510 VANTAA, Finland.

[64] Nalorac Cryogenics Corporation, Martinez, California 94553.

[65] G. Gabrielse, X. Fei, L. A. Orozco, R. L. Tjoelker, J. Haas, H. Kalinowsky, T. A. Trainor, and W. Kells, Phys. Rev. Lett. **65**, 1317 (1990).

[66] J. Wilks, *The Properties of Liquid and Solid Helium* (Clarendon Press, Oxford, 1987).

[67] Jinha Kim, Ph.D. thesis, Harvard University, Cambridge, Massachusetts, 1997.

[68] Clover Lapping Compounds (silicon carbide). Fel-Pro Chemical Products, L.P., Lincolnwood, Illinois 60645. We have exclusively used water-based compounds, but oil-based are available.

[69] Robert S. Van Dyck Jr., Paul B. Schwinberg, and Hans G. Dehmelt, Phys. Rev. D **34**, 722 (1986).

[70] Hans Dehmelt, Richard Mittleman, and Yuan Liu, Proc. Natl. Acad. Sci. USA **85**, 7041 (1988).

[71] Lisa Jill Lapidus, Ph.D. thesis, Harvard University, Cambridge, Massachusetts, 1998.

[72] Frank DiFilippo, Vasant Natarajan, Kevin R. Boyce, and David E. Pritchard, Phys. Rev. Lett. **73**, 1481 (1994).

[73] David Forrest Phillips, Ph.D. thesis, Harvard University, Cambridge, Massachusetts, 1996.

[74] D. J. Wineland and H. G. Dehmelt, J. Appl. Phys. **46**, 919 (1975).

[75] *Amplifier Handbook*, edited by Richard F. Shea (McGraw-Hill, New York, 1966).

[76] D. S. Hall and G. Gabrielse, Phys. Rev. Lett. **77**, 1962 (1996).

[77] Paul Horowitz and Winfield Hill, *The Art of Electronics* (Cambridge University Press, New York, 1994).

[78] D. J. Mar, R. M. Westervelt, and P. F. Hopkins, Appl. Phys. Lett. **64**, 631 (1994).

[79] *Molecular Beam Epitaxy*, edited by M. A. Herman and H. Sitter (Springer-Verlag, Berlin, 1989).

[80] *High-Speed Semiconductor Devices*, edited by S. M. Sze (John Wiley & Sons, Inc., New York, 1990).

[81] *The Quantum Hall Effect*, 2nd ed., edited by Richard E. Prange and Steven M. Girvin (Springer-Verlag, New York, 1990).

[82] K. von Klitzing, G. Dorda, and M. Pepper, Phys. Rev. Lett. **45**, 494 (1980).

[83] *Fine Line Lithography*, edited by R. Newman (North-Holland, Amsterdam, 1980).

[84] Rex Gordon Beck Jr., Ph.D. thesis, Harvard University, Cambridge, Massachusetts, 1998.

[85] Using Kulicke-Soffa model 4123 wirebonder.

[86] Carter's rubber cement, Avery Dennison, Framingham, MA 01701.

[87] R. M. Weisskoff, G. P. Lafyatis, K. R. Boyce, E. A. Cornell, R. W. Flanagan Jr., and D. E. Pritchard, J. Appl. Phys. **63**, 4599 (1988).

[88] Gerald Gabrielse, Hans Dehmelt, and William Kells, Phys. Rev. Lett. **54**, 537 (1985).

[89] Warren Nagourney, Jon Sandberg, and Hans Dehmelt, Phys. Rev. Lett. **56**, 2797 (1986).

[90] D. J. Wineland, J. Bergquist, W. Itano, J. Bollinger, and C. Manney, Phys. Rev. Lett. **57**, 1699 (1986).

[91] Th. Sauter, W. Neuhauser, R. Blatt, and P. E. Toschek, Phys. Rev. Lett. **57**, 1696 (1986).

[92] R. S. Van Dyck Jr., F. L. Moore, D. L. Farnham, and P. B. Schwinberg, Rev. Sci. Instrum. **57**, 593 (1986).

[93] P. B. Schwinberg and R. S. Van Dyck Jr., Bull. Am. Phys. Soc. **26**, 598 (1981).

[94] T. Steimle and G. Alber, Phys. Rev. A **53**, 1982 (1996).

[95] E. M. Purcell, Phys. Rev. **69**, 681 (1946).

[96] D. Kleppner, Phys. Rev. Lett. **47**, 233 (1981).

[97] *Cavity Quantum Electrodynamics*, edited by Paul R. Berman (Academic Press, Boston, Massachusetts, 1994).

[98] John David Jackson, *Classical Electrodynamics*, 2nd ed. (John Wiley and Sons, New York, 1975).

[99] Gerald Gabrielse, Joseph Tan, and Lowell S. Brown, in *Quantum Electrodynamics*, edited by T. Kinoshita (World Scientific, New Jersey, 1990).

[100] William H. Louisell, *Quantum Statistical Properties of Radiation*, 2nd ed. (John Wiley and Sons, New York, 1990).

[101] G. Rempe, F. Schmidt-Kaler, and H. Walther, Phys. Rev. Lett. **64**, 2783 (1990).

[102] *Quantum Measurement*, edited by Vladimir B. Braginsky and Farid Ya. Khalili (Cambridge University Press, Cambridge, 1995).

[103] Kip S. Thorne, Ronald W. P. Drever, and Carlton M. Caves, Phys. Rev. Lett. **40**, 667 (1978).

[104] Hans Dehmelt, Proc. Natl. Acad. Sci. USA **83**, 2291 (1986).

[105] Hans Dehmelt, Proc. Natl. Acad. Sci. USA **83**, 3074 (1986).

[106] Wayne M. Itano, D. J. Heinzen, J. J. Bollinger, and D. J. Wineland, Phys. Rev. A **41**, 2295 (1990).

[107] P. Facchi and S. Pascazio, Phys. Lett. A **241**, 139 (1998).

[108] Richard L. Liboff, *Introductory Quantum Mechanics* (Addison-Wesley, Reading, Massachusetts, 1992).

[109] Wayne Itano, private communication.

[110] L. S. Schulman, A. Ranfagni, and D. Mugnai, Phy. Scr. **49**, 536 (1994).

[111] L. S. Schulman, J. Phys. A **30**, 293 (1997).

[112] Brian D'Urso, private communication.

[113] Lowell S. Brown, Annals of Phys. **159**, 62 (1985).

[114] Lowell S. Brown, Phys. Rev. Lett. **52**, 2013 (1984).

[115] P. B. Schwinberg, R. S. Van Dyck Jr., and H. G. Dehmelt, Phys. Rev. Lett. **47**, 1679 (1981).

[116] R. K. Mittleman, I. I. Ioannou, and H. G. Dehmelt, ICAP 16 Abstracts (1998).

[117] R. S. Van Dyck Jr., P. B. Schwinberg, and H. G. Dehmelt, in *The Electron*, edited by D. Hestenes and A. Weingartshofer (Kluwer, Deventer, 1991).

[118] Richard Mittleman, Hans Dehmelt, and Sander Kim, Phys. Rev. Lett. **75**, 2839 (1995).

[119] G. Gabrielse and J. Tan, in *Cavity Quantum Electrodynamics*, edited by Paul R. Berman (Academic Press, Boston, Massachusetts, 1994).

[120] Gerald Gabrielse, Phys. Rev. A **29**, 462 (1984).

[121] S. Ichimaru, H. Iyetomi, and S. Tanaka, Phys. Rep. **149**, 91 (1987).

[122] G. S. Stringfellow and H. E. DeWitt, Phys. Rev. A **41**, 1105 (1990).

[123] D. H. E. Dubin, Phys. Rev. A **42**, 4972 (1990).

[124] G. Gabrielse, X. Fei, K. Helmerson, S. L. Rolston, R. L. Tjoelker, T. A. Trainor, H. Kalinowsky, J. Haas, and W. Kells, Phys. Rev. Lett. **57**, 2504 (1986).

[125] G. Gabrielse, L. Haarsma, and S. L. Rolston, Int. J. of Mass Spec. and Ion Proc. **88**, 319 (1989).